

**The first direct measurement of the
 $^{17}\text{O}(\alpha,\gamma)^{21}\text{Ne}$ reaction and its impact on heavy
element production**

Matthew P. Taggart, B.Sc. (Hons), M.Sc.

A thesis submitted for the degree of

Doctor of Philosophy

University of York

Department of Physics

September 2012

Abstract

The ratio of the $^{17}\text{O}(\alpha,\gamma)^{21}\text{Ne}$ reaction rate to that of the competing $^{17}\text{O}(\alpha,n)^{20}\text{Ne}$ reaction has long been thought to have significant consequences to the s-process. Specifically in massive rotating stars at low metallicity, the abundance of light isotopes toward the end of the helium burning stages can be sufficient to compensate for their relatively low neutron capture cross sections. The high neutron absorption rate on ^{16}O can potentially reduce the efficiency of the weak s-process unless there is a substantial recycling factor through the $^{17}\text{O}(\alpha,n)^{20}\text{Ne}$ reaction. The strength of the weaker (α,γ) channel, relative to that of the (α,n) , is crucial to determining weak s-process elemental abundances due to the reduction in neutron availability a strong channel would cause.

Prior to this work all astrophysical calculations were based on sparse data on the (α,n) channel and two wildly conflicting theoretical models on the (α,γ) channel. Calculations based on predicted reaction rates have so far resulted in a discrepancy of up to 10^4 in the abundance of elements from strontium to barium. This work presents the results of the first direct measurement of the $^{17}\text{O}(\alpha,\gamma)^{21}\text{Ne}$ reaction carried out on the DRAGON recoil separator at the TRIUMF laboratory in Vancouver, Canada. Cross section measurements were performed across the energy range of $0.6 < E_{cm} < 1.6$ MeV. Data was successfully taken enabling the calculation of a resonance strength within the Gamow window of $\omega\gamma = 4 \pm 0.3$ meV at $E_{cm} = 0.621$ MeV, as well as confirmed resonance strengths at 0.8 and 1.165 MeV and further upper limits.

The calculated reaction rate appears to oppose the assignment of ^{16}O as a poison, instead favouring neutron recycling via the (α,n) channel, the associated efficiency of the s-process and resulting higher Sr-Ba abundances. However, it should be highlighted that without further information covering the lower portion of the Gamow window this can only represent a lower limit on the $^{17}\text{O}(\alpha,\gamma)^{21}\text{Ne}$ reaction rate. The techniques, data and results relevant to this reaction are presented within this thesis.

Contents

Contents	ii
List of Figures	vi
List of Tables	ix
Acknowledgements	xi
Declaration	xiii
1 Introduction	1
1.1 In the beginning...	1
1.2 Nucleosynthesis	1
1.2.1 Nuclear Fusion: The primary method of isotope production	5
1.2.2 Above the Iron Group	7
1.2.2.1 The r-Process	7
1.2.2.2 The s-Process	11
1.2.2.3 S-, R- and P-nuclei	14
2 Astrophysical Motivation	16
2.1 Impact of ^{17}O	16
2.2 The status of the $^{17}\text{O}(\alpha,\gamma)/(\alpha,n)$ ratio	19
2.2.1 Estimated Reaction Rate	21
2.2.2 Theoretical Model: Generator Coordinate Method	21
2.3 S-process abundances	22
3 Nuclear Theory	25
3.1 Cross Section	25
3.2 Astrophysical S-factor	27

3.3	Thermonuclear Reaction Rate	28
3.3.1	Non-resonant Reaction Rate	29
3.3.2	Isolated Narrow Resonances	32
3.4	Nuclear Reactions	35
3.4.1	Reaction Energy	36
3.4.2	Inverse Kinematics	36
3.4.3	Angular Distributions	39
3.5	Helium Burning in Massive Stars	40
4	Experimental Setup	43
4.1	The ISAC facility	43
4.1.1	Isotope Separation On-Line	43
4.1.2	Off-Line Ion Source	45
4.1.3	Linear Accelerator	48
4.1.3.1	Beam Tuning	50
4.2	DRAGON - Detector of Recoils And Gammas Of Nuclear reactions . . .	50
4.2.1	Separator	50
4.2.1.1	E/M dipoles: How recoil separation is produced	54
4.2.1.2	“Leaky” Beam and Suppression Factors	56
4.2.1.3	Focussing Magnets	57
4.2.1.4	Field-Monitoring Devices	57
4.2.1.5	Faraday Cups	58
4.2.1.6	Beam Diagnostics	59
4.2.2	The Windowless Gas Target	60
4.2.2.1	Issues with Gas Targets: Beam Straggling, Gas Con- finement	60
4.2.2.2	Technical Aspects	62
4.2.2.3	Target Thickness and Profile	62
4.2.3	BGO γ -ray array	64
4.2.3.1	Bismuth Germanate as a Detector Choice	64
4.2.3.2	Detector Efficiency and Resolution	68
4.2.4	End Detectors	68
4.2.4.1	Micro-Channel Plates	68
4.2.4.2	Ionisation Chamber	70
4.2.5	Ancillary Measurements	72
4.2.6	Data Acquisition	74

4.3	The Experiment - S1216	77
5	Data Analysis	80
5.1	Overview of Analytical Process	80
5.2	Calculation of Yield	80
5.2.1	Selection of Events	81
5.2.1.1	Summary of Ion Chamber Histogram Features	83
5.2.1.2	γ ray Coincident Events	85
5.2.1.3	Separator Time-of-Flight	85
5.2.1.4	MCP calibration	87
5.2.2	Charge-state Fraction Measurement and Interpolation	90
5.2.3	GEANT simulations	92
5.2.3.1	Separator Transmissions	95
5.2.3.2	BGO Efficiency	99
5.2.4	MCP Efficiencies	101
5.3	Total Integrated Beam	103
5.3.1	Measurement of Elastics	103
5.3.2	True Beam Measurement	104
5.3.3	Beam Normalisation	106
5.4	Target Nuclei	108
5.4.1	Thick Target Yield and Resonant Reactions	110
5.4.2	External Temperature Investigation	113
5.5	Determination of Astrophysical Reaction Properties	115
5.5.1	Cross Section and S-factor	115
5.5.2	Error Analysis	116
5.5.2.1	The Absent Recoils	117
6	Results and Interpretation	118
6.1	The $^{17}\text{O}(\alpha,\gamma)^{21}\text{Ne}$ Cross Section	118
6.2	Extrapolating the Astrophysical S-factor	120
6.3	The Strength of the Resonance	121
6.3.1	$E'_{cm} = 806$ keV	123
6.3.2	Selection of Likely Resonances	127
6.4	Thermonuclear Reaction Rates	127
6.4.1	Resonant Contribution	128
6.4.2	Numerical Integration of the S-factor Excitation Function	130

6.4.3	Parameterisation of the Reaction Rate	132
6.4.4	Summary of Reaction Rate Calculation	133
6.5	Uncertainty of Results	134
6.6	“Other” Data	136
7	Conclusions and Further Work	139
A	Data	141
B	GEANT Input Parameters	147
C	Thick Target Yield	151
D	The S1216 Beamlog	153
E	Logic Symbols	155
	Nomenclature	157
	References	160

List of Figures

1.1	The chart of the local Galactic elemental abundances	2
1.2	Primordial nucleosynthesis reaction network	3
1.3	A schematic of the Coulomb barrier	5
1.4	Binding energy per nucleon curve	8
1.5	Path of the r-process	10
1.6	Path of the s-process	12
1.7	Solar system neutron exposure curve	13
1.8	Class assignments for s-, p- and r-nuclei	15
2.1	Thermal neutron capture cross sections $Z < 38$	18
2.2	Reaction chain for oxygen	18
2.3	Data and theoretical $^{17}\text{O}(\alpha,\gamma)$ and (α,n) S-factors prior to 2009	20
2.4	Full range of (α,n) measurements	20
2.5	The rival $^{17}\text{O}(\alpha,\gamma)/(\alpha,n)$ ratios.	22
2.6	S-process production fraction for CF88 and GCM reaction rates	24
3.1	Comparison of experimental cross section and S-factor	28
3.2	Dominant energy-dependent functions for charged-particle induced reactions	30
3.3	Cartoon of competing reaction mechanisms	35
3.4	Representation of the reaction recoil cone	37
3.5	Angular distributions for CoM and Lab reference frames	39
3.6	The ^{21}Ne level scheme for the states of astrophysical interest above the α -particle threshold	41
4.1	The ISAC-I experimental hall	44
4.2	Photograph of the TRIUMF Off-Line Ion Source	46
4.3	The Supernanogan ECR Ion Source	47

4.4	The ISAC-1 linear accelerator	49
4.5	Example of the CCD camera “beam spot”.	51
4.6	A representation of the DRAGON facility.	52
4.7	Schematic of the DRAGON recoil separator	55
4.8	Example of a Faraday cup	59
4.9	The interior of the gas target	61
4.10	Schematic of the gas target	61
4.11	Gas target pressure profile	63
4.12	The DRAGON BGO array	65
4.13	Schematic diagram of the DRAGON BGO array	66
4.14	Relative importance of the major γ -ray interactions	67
4.15	Intrinsic efficiencies for some common detector materials	67
4.16	The DRAGON MCP box	69
4.17	Example of a chevron pattern MCP system	70
4.18	Schematic of the DRAGON Ionisation Chamber	71
4.19	The DRAGON DAQ	75
4.20	The planned experiment	78
5.1	Standard analysis technique - ICsumMCPtof	82
5.2	ΔE -E ion chamber analysis	83
5.3	Particle ID combinations	84
5.4	Separator ToF cross-overs	86
5.5	Separator ToF analysis	88
5.6	Calibration of the MCP TAC for November energies	89
5.7	Charge-state distribution for $E_{beam} = 298.56$ keV/u	91
5.8	Charge-state fractions for the whole energy range	93
5.9	Assumed decay scheme for the initial GEANT3 simulations	95
5.10	Cartoon of “best/worse” case separator transmission technique	96
5.11	Distribution of separator transmissions for $E_{cm} = 0.829$ MeV	97
5.12	Effect of angular distributions on centre target separator transmissions	97
5.13	Separator transmissions for isotropic distributions at the ~ 0.8 MeV peak	99
5.14	Full Geant3 decay scheme	100
5.15	MCP efficiency	102
5.16	MCP foils	103
5.17	Elastic-scattering spectrum	104
5.18	Rossum Faraday-cup reading	105

5.19	Beam normalisation factors for November energies	107
5.20	Target Pressure Distribution for $E_{cm} = 0.831$ MeV	109
5.21	Target Pressure Distribution for $E_{cm} = 1.116$ MeV	109
5.22	Breit-Wigner resonance within the gas target	111
5.23	Effect of possible ambient temperature variation	113
5.24	Temperature in Vancouver during $E_r = 806$ keV measurements	114
6.1	The $^{17}\text{O}(\alpha,\gamma)^{21}\text{Ne}$ cross section.	119
6.2	The $^{17}\text{O}(\alpha,\gamma)^{21}\text{Ne}$ Astrophysical S-factor.	122
6.3	The $\omega\gamma$ s for the $^{17}\text{O}(\alpha,\gamma)^{21}\text{Ne}$ reaction.	124
6.4	BGO z-distributions for $E_{cm} = 0.814$ & 0.825 MeV	125
6.5	Assignment of the ~ 0.8 MeV resonance.	126
6.6	The $^{17}\text{O}(\alpha,\gamma)^{21}\text{Ne}$ $\omega\gamma$ reaction rates.	129
6.7	The fit to the non-resonant S-factors.	131
6.8	Error Budget of the Resonance Strength	135
6.9	Comparison of the $^{17}\text{O}(\alpha,\gamma)^{21}\text{Ne}$ $\omega\gamma$ reaction rates.	137
A.1	Upper and lower boundaries to the non-resonant contribution.	145
A.2	Boundaries of non-resonant reaction rate.	146
C.1	Thick target yield for a single resonance	152
C.2	Thick target yield for a double resonance	152
E.1	Standard Logic Box Symbols	155

List of Tables

1.1	Interstellar Medium (ISM) Mass Fractions	4
1.2	Examples of Coulomb barrier heights	6
1.3	Stellar burning stages	7
1.4	Free-neutron densities	8
1.5	Neutron Exposures	12
1.6	The influence of magic numbers on neutron capture processes	14
2.1	Relative strengths of the fundamental forces	19
3.1	Q-values of relevant reactions	36
3.2	DRAGON recoil cone half-angle	38
3.3	Energies of astrophysical interest	40
4.1	DRAGON characteristics	53
4.2	Mass-to-charge ratios for key isotopes	56
4.3	Sample target thicknesses	64
5.1	Charge State Distribution Widths	92
5.2	Charge State Fraction	94
5.3	GEANT simulation results	98
5.4	Calculated number of total target nuclei and the one variable, pressure, for each investigated centre-of-mass energy.	110
5.5	Fraction of target nuclei relevant to resonant reactions	112
5.6	Effect of temperature variation at different pressures on the number of target nuclei	115
6.1	Table of $^{17}\text{O}(\alpha,\gamma)^{21}\text{Ne}$ Cross Sections	120
6.2	Table of designated $^{17}\text{O}(\alpha,\gamma)^{21}\text{Ne}$ resonances	127
6.3	Analytical approximation for the DRAGON reaction rate	132

6.4	Parameterisation Covariance Matrix	133
6.5	Parameterisation Correlation Matrix	133
6.6	Resonance strengths from the University of Notre Dame group	136
A.1	$^{17}\text{O}(\alpha,\gamma)^{21}\text{Ne}$ Data	142
A.2	Results for the weighted averages of the multiply measured resonances.	142
A.3	Parameterisation of the $^{17}\text{O}(\alpha,\gamma)^{21}\text{Ne}$ reaction rate.	143
D.1	The Rossum heartbeat runlog	154
E.1	Boolean logic truth tables	156

Acknowledgements

Despite the premise of developing into a trained, independent researcher learning to rely on one's own skillset and education rather than the safety net of more senior academics, no PhD can be completed alone. Experiments are too vast, resources too limited, and time too precious to allow the student complete freedom to learn through their mistakes. Here I am able to thank the people who have supported me through the past four years of study, be it in an academic nature, an emotional one, or even those who might enjoy the occasional beverage.

The first person to thank is my supervisor, Dr Alison Laird. Without her support, patience and tolerance I would simply not have reached this stage. I cannot thank her enough, but I shall try nonetheless. Thank you. I cannot overlook the support offered from the rest of the nuclear physics group at York. Professors Mike Bentley and Brian Fulton were invaluable during both the experiment and in discussing my analysis. Dr Simon Fox was instrumental in all things experiment-y. The post-docs who do those many thankless tasks that post-docs are invariably forced to do; Christian, Paul, Jamie and Kelly, thank you for putting up with my frequent idiocy. Of course, no research department is complete without its students. Many, many students. I'm sure they contributed somehow to my experience over the last four years and statistically some of that is bound to be positive. So, Adam, James, Lianne, Dan and the remaining "meat in the room", thank you for your presence. The contribution of Alan Smithee to this thesis should also be acknowledged.

I was very fortunate to find myself stationed in Vancouver for a portion of my studies, and it would be exceptional poor form not to express my appreciation for all those who made me feel welcome when I was half the world away. The DRAGONeers: Chris, Dave, Ulrike, Lars and Jen, thank you for showing me what life at research facility is like. Not to mention all the work as my surrogate post-docs and afternoon coffee breaks. Continuing the TRIUMF theme, a great deal of thanks and appreciation is directed towards all those involved in the experiment, nuclear physics is not a one person show. A special thanks must go to Keerthi Jayamana for such a great job in delivering the ^{17}O beam at such short notice when our fluorine experiment had failed. I would also like to thank Bob Laxdal,

Marco Marchetto and the ISAC operations group for all their work getting the beam to DRAGON.

The next group I wish to say thank you to are my friends, although I wonder why they still put up with me at times. I'm far from convinced that they realise how much their friendship has meant to me, certainly over the last few years, but without Clare, Gemma, Phil, Mary and Ed, I'm not sure how I would have managed.

Then there is my family, Mum and Dad. You have shown me nothing but support regardless of what decisions I made. Throughout all my time at university, when I returned home not really knowing what I wanted to do with my life, and then when I eventually returned to academia to embark on these studies, I always knew you would be there if I needed you. Thank you both.

Finally, I must say thank you to Su, who is my favourite.

Declaration

I declare that the work presented in this thesis, except for those contributions explicitly acknowledged and referenced within the body of the text, is based upon my own research under the supervision of Dr A M Laird. No part of this research has previously been submitted for any award or qualification.

Matthew Paul Taggart

Chapter 1

Introduction

yugen /yoo-geh/ *n.* (japanese)

an awareness of the universe that triggers emotional responses too deep and mysterious for words.

1.1 In the beginning...

Nuclear astrophysics might be considered a field of bridge-building; not in the architectural sense, of course, but in the context of forging collaborations between two distinct groups. Neither wholly nuclear physics, nor in truth astronomy, the specific techniques of each field are forged together in the melting pot of scientific curiosity that is nuclear astrophysics. The purpose of the field is to study those nuclear reactions that take place within stars, to understand exactly how they burn, how their energy is generated to prevent stellar collapse, and where these reactions occur. This aim, the primary goal of nuclear astrophysics, can be put quite succinctly in terms of one figure, to explain the chart of the abundances as shown in Figure 1.1. Or, to steal a quote from the founders of the entire discipline, *“To attempt to understand the sequence of events leading to the formation of the elements it is necessary to study the so-called universal or cosmic abundance curve.”* [1]

1.2 Nucleosynthesis

Let us begin our analysis with two extremely simple (although not unrealistic) assumptions, from which one could sketch a predicted version of an abundance curve and compare to Figure 1.1. Assuming that all nuclei evolve from hydrogen [1] and that the primary

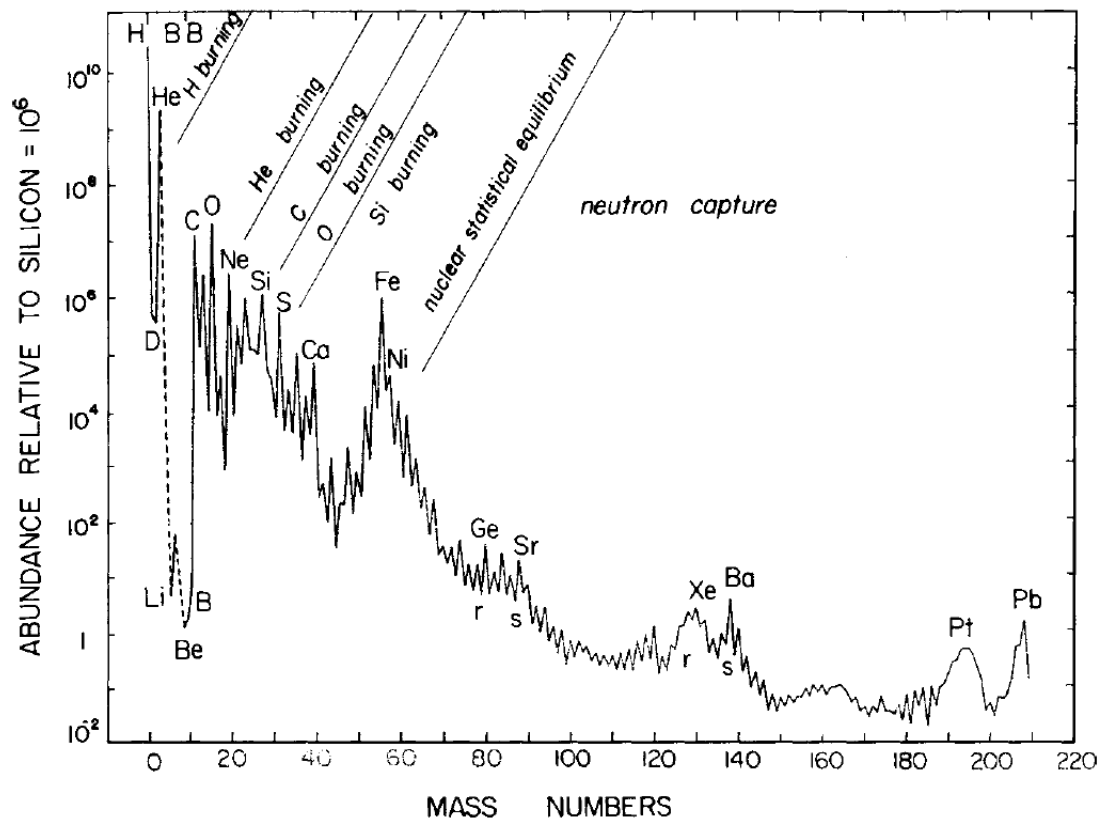


Figure 1.1: The chart of local Galactic elemental abundances [2, 3]. The data has been normalised to 10^6 atoms of ^{28}Si and is based on determinations of solar-system abundances with further input from nearby stars and emission nebulae. In addition to depicting the relative abundances, the plot also highlights the astrophysical processes responsible for particular elements. For example, stellar oxygen-burning is the source of the abundance of sulphur, whereas the elements more massive than iron are the result of neutron captures.

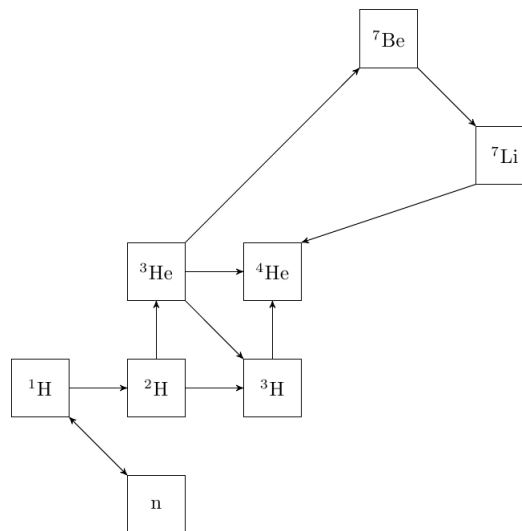


Figure 1.2: The reaction network for primordial nucleosynthesis [4, 5]

means of nucleosynthesis is fusion, one might naïvely expect the distribution to be of the form of a smooth curve, with the vast majority of matter being hydrogen with ever decreasing quantities of nuclei with increasing mass. This general trend holds true, although it is an obvious over-simplification. The chart in Figure 1.1 contains many features that need to be explained as the many peaks and troughs are not always easily understood.

One might ask the question, “How do we know the distribution of elemental abundances?” What data are there to examine? The answer, fortunately, is a great deal, and from a vast range of sources. Obviously the entire universe has not been measured, there is not some galactic set of scales, but there are both direct and indirect means with which this distribution can be calculated. The direct methods, those which require some form of chemical or laboratory analysis, include meteorites, lunar samples and interstellar dust, as well as extensive terrestrial samples. The indirect make use of remote techniques, such as stellar spectroscopy, thermal mapping and deductions from stellar structure and evolution [2]. Needless to say, a great deal of work encompassing a vast range of disciplines contributes to the field of nuclear astrophysics.

The colossal abundance of both hydrogen and helium relative to the entirety of the remainder of the nuclide chart is known to stem from the Big Bang, which in turn names the first of the three classes of nucleosynthesis. In fact the ratio of the abundances of the first two elements is readily understood and can be explained by simply considering the basic reaction network for the lowest metallicity (defined as the fraction of the star’s mass that is neither hydrogen nor helium [2]) scenarios shown in Figure 1.2 and the primor-

dial neutron-proton ratio [6]. Big Bang nucleosynthesis (BBN) reaches its limit at this point, with nuclei beyond the trace amounts of ${}^7\text{Li}$ precluded from production through this process for reasons that shall be explained momentarily. Therefore, one source of the nuclei has been ruled out already and an alternative explanation for the origins of the more massive elements must be sought.

Element	Mass Fraction
X	0.70
Y	0.28
Z	0.02

Table 1.1: Approximate relative solar abundances, also characteristic of those of the local interstellar medium (ISM) and young stars. Standard astrophysical notation defines: Hydrogen, X; Helium, Y and the “metals”, Z [2].

The “metals” (defined by astrophysicists as anything with an atomic number greater than 2) must therefore be a result of stellar nucleosynthesis, and introduces the oft-used thesis-opening quote of “*we are all made of stardust*” [7]. However, why this is the case needs to be explained. What causes the BBN to cease at ${}^7\text{Li}$? This happily provides a nice segue into describing the second feature of Figure 1.1, “the helium-carbon chasm”. A swift glance at any copy of the Segré chart provides this answer. There exist no stable mass 5 or mass 8 isobars. This greatly limits the escape from the non-metal region into the reaction networks of the more massive nuclei. The reaction of a proton on an alpha particle, or ${}^4\text{He}$ fusion will result only in a short-lived nucleus, i.e. one that will not last long enough for further reactions to take place on it. Whilst small amounts of ${}^7\text{Li}$ are produced and may act as seed nuclei, the cross sections of these reactions are well studied, the reaction network is known, and there is simply not enough time [8]. The universe has existed for a finite period, one that is not long enough for reactions on ${}^7\text{Li}$ seeds or three separate α particles to explain the existence of metals in the quantities that mankind has observed.

This raises the question of how other nuclei come into being if they cannot pass through masses 5 and 8. The answer lies in the triple-alpha process and the prediction of the Hoyle state [9], a resonance that allows an equilibrium of ${}^8\text{Be}$ to develop such that captures to ${}^{12}\text{C}$ might proceed. However, in terms of lithium and beryllium abundances, these are most likely the result of cosmic ray spallation on higher mass nuclei, as opposed to a more direct means of production through fusion or capture processes.

The next feature that warrants discussion is the saw-tooth pattern. This is displayed across the full mass range, although its effect may be diminished through being washed out due to other, more prominent phenomena. There are two contributions resulting in the

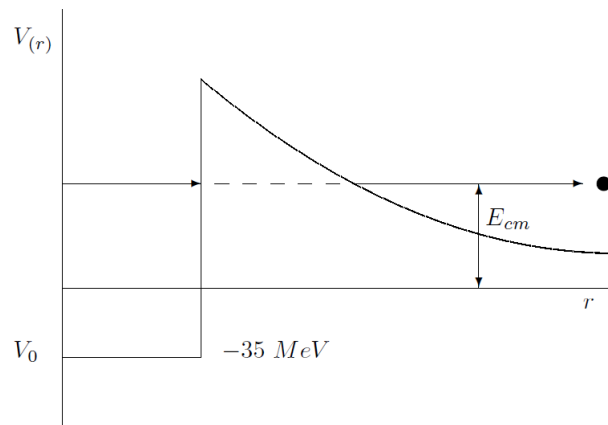


Figure 1.3: A schematic of the Coulomb barrier

saw-tooth, each from a separate source. The first contribution stems from an examination of the Semi-Empirical Mass Formula (SEMF), which does not need to be discussed other than to present the concept of the pairing term. Nuclei containing paired nucleons in their outermost shell exhibit a higher binding energy, and are thus more stable. Likewise, the “ α -effect” from successive captures of (extremely stable) α particles causes large abundance peaks at 4-integer mass intervals.

To provide an early summary, we see an increase in elemental abundance where there exists a mechanism to enhance the stability at that point.

1.2.1 Nuclear Fusion: The primary method of isotope production

Should nuclei attain sufficient energy, there is a probability that their surfaces might come into contact with each other and that a reaction might occur. Each nucleus contains a number of protons, which having an electric charge of 1^+ are subject to the electromagnetic force. For like charges this force is repulsive, and this repulsion is termed the Coulomb barrier, which in turn will hinder the probability of interaction.

Figure 1.3 shows a simple potential well diagram, featuring a Coulomb barrier. Should a nucleus attain sufficient energy to be removed from the potential well and be energetically above the barrier, the interaction is unimpeded by the Coulomb force and may proceed with a much greater probability. However, while the nucleus’ energy remains below the height of the barrier the reaction mechanism is hindered. This is not to say that the reaction is completely stopped; there remains a finite probability that the particle might tunnel through the barrier quantum mechanically. This probability increases with

energy, as can be seen in the diagram that the barrier narrows as energy increases.

Interactions between different elements will obviously have different barriers, as the Coulomb force scales with the atomic number. This barrier energy, E , can be determined through:

$$E = \frac{Z_A Z_B e^2}{4\pi\epsilon_0 r} \quad (1.1)$$

where Z_A and Z_B are the proton numbers of the interacting nuclei separated by a distance of closest approach, r , and e and ϵ_0 have their usual definitions as the electric charge and permittivity of free space. From Equation 1.1 it becomes clear that a proton-proton interaction will have a far smaller Coulomb barrier than, say, two ^{238}U nuclei attempting to fuse, or even the interaction between an oxygen nucleus and an alpha particle. These are displayed in Table 1.2 for a selection of relevant interacting partners.

reaction	barrier potential (MeV)
p + p	0.389
$^{17}\text{O} + \alpha$	1.92
$^{18}\text{Ne} + \alpha$	2.824
$^{56}\text{Fe} + ^{56}\text{Fe}$	85.63
$^{238}\text{U} + ^{238}\text{U}$	839.019

Table 1.2: Examples of Coulomb barrier heights [10]

This also explains why stars burn in distinct stages; the ignition of successive burning stages requires an increase in stellar temperature such that the interacting particles have a high enough energy for sufficient penetration of the Coulomb barrier. Stars burn their fuel to resist gravitational collapse. Once the present fuel, say, helium, is used up, the star cannot withstand the gravitational force any longer and so contracts. The collapse of the star releases further energy in the form of gravitational potential energy, which is converted into thermal energy. If the energy released is sufficient, i.e. if the star is massive enough, this will ignite the next burning stage with carbon as the fuel source.

Depending on the mass of the star, successive burning stages and stellar collapse might occur all the way up to iron, or it could continue to collapse until supported by electron degeneracy pressure, at which point it ceases to invoke the advanced burning stages. The ignition temperatures, T_i , for each burning stage, along with the respective mass star they might occur in are presented in Table 1.3. The Coulomb barrier provides the obstacle to stellar burning; it is why high temperatures are required to enable nuclear fusion and why the heaviest metals are only produced in the most massive stars.

Stage	Mass (M_{\odot})	T_i (T_9)
He	<8	0.2
C	>8	0.8
Ne	9	1.4
O	10-11	2
Si	15	3.5

Table 1.3: Stellar burning stages [11]

1.2.2 Above the Iron Group

Almost every text on nuclear physics discusses that the highest binding energy per nucleon occurs at ^{56}Fe , the peak on the famous curve shown in Figure 1.4. Technically this is not correct. In fact it is ^{62}Ni at $\text{BE}/A = 8.795 \text{ MeV}/u$, compared to the value of $8.790 \text{ MeV}/u$ of ^{56}Fe , that occupies the highest point on Figure 1.4. However, as discussed in [12, 13], the universal abundance of ^{62}Ni is relatively low when its status as most tightly-bound nucleus is considered. These texts state that ^{56}Fe is taken to be the end product of stellar fusion due to there being no convenient bridging mechanism to produce ^{62}Ni .

Returning to the binding energy per nucleon curve, it should be apparent that fusion of nuclei to the right of the peak will result in a decrease of energy, rather than a release. It is the basic principle behind nuclear power generation, fissioning high mass isotopes back towards the left of the plot or (possibly) fusing low mass isotopes up to the iron peak. Of course, in the scope of this work the latter is the primary method of stellar energy production.

Although it would be incorrect to say that nuclear fusion of these higher mass isotopes does not occur, the Coulomb interaction becomes such a colossal barrier that the temperatures, and thus energies, required are so great that should high-mass fusion take place, the resulting nuclei would subsequently be dissociated via photodisintegration. Certainly the observed abundances necessitate some alternative explanation.

1.2.2.1 The r-Process

The key limitation of nucleosynthesis via charged-particle interactions, the Coulomb barrier, can be totally bypassed when neutron capture is considered. The neutral charge, and therefore absence of a Coulomb barrier, means that neutron capture can occur even at relatively low energies, i.e. low-mass stars, and there is a far lessened probability of reduced abundances through photodisintegration.

Of course, that neutron capture can occur at lower temperatures is not to say that it doesn't occur at higher temperatures and in fact it is this scenario that shall be considered

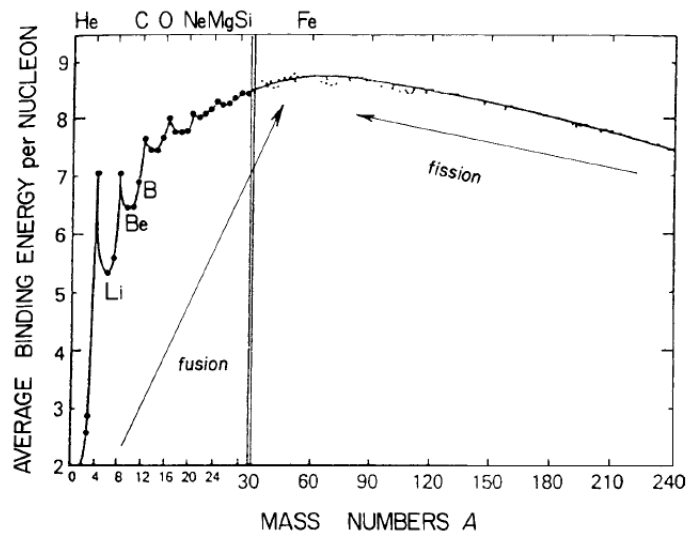


Figure 1.4: Binding energy per nucleon curve as a function of mass number [2, 14]. Note the peak value occurs around iron. The arrows labelled “fusion” and “fission” show that energy is released as the mass number approaches the peak.

first. The key parameter for neutron capture (something that will be constantly alluded to within this thesis, particularly in Chapter 2) is naturally the neutron density.

n_n (cm^{-3})	origin
10^5	s-process
10^{24}	r-process
10^7	fission reactor

Table 1.4: Free-neutron densities [15]

The neutron density determines whether nucleosynthesis follows one path or another. The densities characteristic of each process are listed in Table 1.4, and it is a curiosity, an extremely helpful simplification, that astrophysical neutron fluxes seem to occur as being either very large, or very small. Phenomena producing $10^5 < n_n < 10^{24}$ are rare [15]. Consider first a scenario where there might exist an abundance of neutrons so great that there is no possibility of that being the limiting factor to the reaction rate. It has been suggested that the extreme violence of supernovae or perhaps γ -ray bursters could provide such abundances, although this has yet to be proved [2]. Next consider what reactions might occur. With limitless reactants there should be a series of neutron captures on the nuclei present in such environments, occurring on nuclei of all masses with differing probabilities. The heavier, iron-group, nuclei will generally have greater neutron capture

cross sections than lighter nuclei such as oxygen or neon. This deficiency in cross section can often be offset by the sheer abundance of these lighter isotopes, the ashes of helium burning stages, and is an important point that shall be discussed shortly. However, in terms of nucleosynthesis, it is the successive captures on iron seeds that lead to the r-process abundance distribution. A lighter seed, such as oxygen, is prohibited from contributing significantly to the abundance curve twofold. Firstly, it would require an additional ~ 40 neutrons to populate those r-process nuclei, but secondly, and arguably more importantly, it is clear from Table 1.2 that charged particle reactions will be competing with the r-process and therefore remove the availability of those lighter nuclei as seeds.

These captures drive the abundance distribution away from the valley of stability, producing unstable nuclei with ever-shortening lifetimes, a characteristic of each specific nuclide. Naturally, these decay back towards the valley of stability once the neutron flux drops. Likewise, a reaction has a rate (thoroughly discussed in Chapter 3) that may or may not be greater than the radionuclide's lifetime. The scenario here, one of extreme violence and colossal neutron flux will be the first case. This is described by:

$$\tau_{nc} \ll t_{1/2}, \quad (1.2)$$

where it becomes clear that after the first capture, the timescale for the next neutron capture, τ_{nc} , is less than that for β decay, $t_{1/2}$, and so further captures will occur before the radionuclide can decay back towards stability.

This results in successive rapid (the r- of the r-process) neutron captures pushing out toward the neutron drip-line. Once the r-process distribution reaches some barrier, be it the neutron drip-line itself or the increased stability afforded by the neutron magic numbers, its path across the chart of the nuclides changes direction. At these points the half-life of the nuclide $t_{1/2}$ is in fact lower than the time for neutron capture, which allows the neutron-rich heavy nucleus to β decay back towards stability before tracing out another isotopic line (only with higher Z). This r-process path is much more easily explained by examining Figure 1.5. It is clear that in the presence of such a strong neutron flux captures on the seed nuclei, the iron peak from Figure 1.1, that material will be moved from abundant shell-burning ashes to populate the heavier portions of the nuclide chart. This is shown by the horizontal lines on Figure 1.5.

One must also consider the end stages of the r-process; what happens when this intense neutron flux becomes less intense? After all, the stellar scenarios highlighted have finite timescales (admittedly in terms of minutes, compared to a reaction timescale of

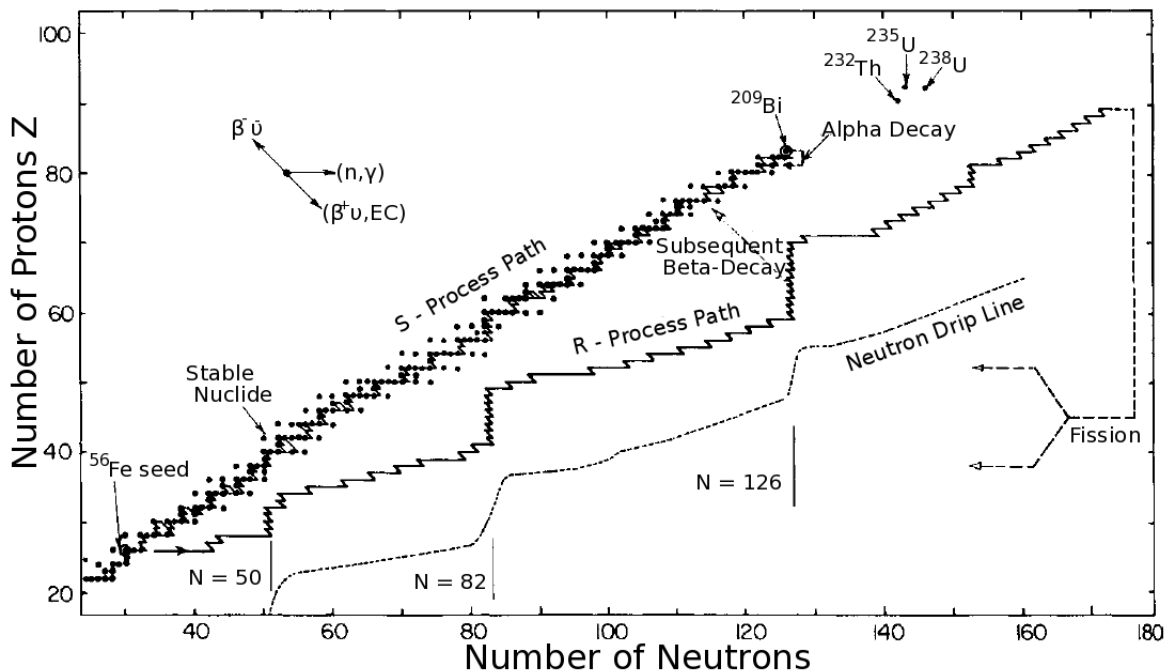


Figure 1.5: The respective rapid and slow neutron capture paths displayed on the N versus Z chart. The r -process path was calculated for a temperature of 1 GK and with a neutron density of 10^{24} cm^{-3} as described in Table 1.4. Amended from [2]

nanoseconds, but a timescale all the same). Once no longer in the presence of a sufficiently intense neutron flux to satisfy Equation 1.2, a condition known as freeze-out, the heavily neutron-rich r -process nuclides will undergo the same successive β^- decays that occur when the neutron separation energy is lowered sufficiently to also produce this effect. However, instead of a few separation-energy-increasing β decays before neutron capture restarts, there are now no further neutrons available. This leads to the abundance distribution transitioning through the respective isobaric chains as the decays continue until a stable, or sufficiently long-lived nuclide is reached. This return to stability is shown on Figure 1.6 as the diagonal lines from the r -process region.

Still to be discussed is the termination of the r -process, which is distinct from the cessation of neutron captures and freeze-out. The continuous cycle of neutron captures and β decays will eventually produce nuclei in the region of the super-heavies, where $A_{max} = 270$. Once this region is reached, termination is due to neutron-induced fission of the super-heavy nucleus, resulting in the production of two $A_{max}/2$ nuclei (plus a number of free neutrons) which are fed back into the stellar nuclear abundance. Should this termination happen prior to freeze-out and a significant neutron density still remains, then of

course, the r-process will continue and further captures can occur with the fission products acting as heavy seed nuclei.

1.2.2.2 The s-Process

In contrast to the r-process, and far more likely in the neutron flux during stellar burning stages, we have the slow neutron-capture process. Whereas previously we have discussed where stable seed nuclei achieve a rapid succession of neutron captures, allowing them to move horizontally across the Segré chart, we now consider a more sedate series of reactions. In a relatively low neutron flux, the time-scale of the β decay for each unstable nucleus resulting from any neutron capture will be significantly lower than the time-scale of the next, successive capture, which is presented as:

$$\tau_{nc} \gg t_{1/2}. \quad (1.3)$$

It is clear that Equation 1.3 is simply Equation 1.2 with the inequality sign reversed.

Since the unstable nuclei now have sufficient time to undergo β decay, the path more closely hugs the line of stability. In fact, the general assumption for the s-process as given in [15] is that “all beta decays of radioactive nuclei are assumed to be quite rapid compared to the rate for capturing neutrons” and consequentially experience an immediate decay back to stability from any unstable nucleus produced. Figure 1.6 shows that nuclei of the s-process path are not found more than one neutron away from stability. The low flux required for the s-process, shown in Table 1.4, in contrast to the explosive conditions thought necessary for the r-process, is likely to occur in standard stellar burning reactions. The primary neutron source will be produced during helium burning stages, when strong (α, n) reactions can provide the required flux. Specifically $^{13}\text{C}(\alpha, n)^{16}\text{O}$ and $^{22}\text{Ne}(\alpha, n)^{25}\text{Mg}$ provide adequate neutrons for the s-process and with positive Q-values are therefore uninhibited being exothermic reactions.

It has already been established how crucial the neutron density is to heavy element production but the cross section must have a role to play too. So far we have only discussed the contribution from lighter elements, yet their neutron capture cross sections tend to be significantly lower than, say, the heavier, iron group elements [15]. That the neutron density, specifically the number of free neutrons, is such a limited quantity it becomes more efficient in terms of element production for nucleosynthesis to occur as captures on the iron group nuclei, as opposed to lighter helium-burning ashes where fusion remains a viable alternative. Indeed, the higher cross sections will naturally favour neutron capture

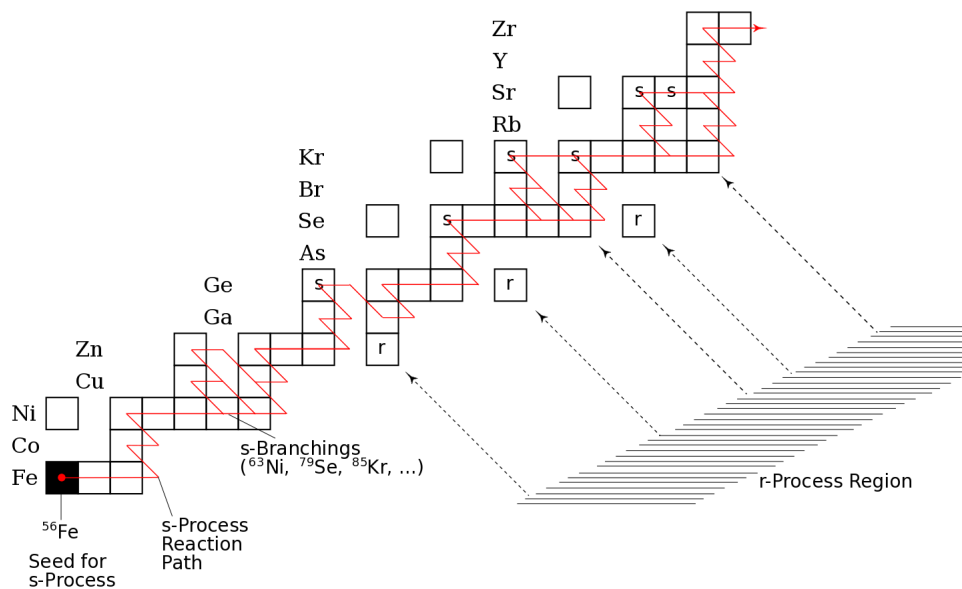


Figure 1.6: The path of the s-process [16]. The boxes correspond to stable isotopes which are closely traced out by the s-process, never straying more than one nucleon away from stability.

by these heavier seed nuclei, not to mention that a heavier starting point will obviously require fewer neutrons to populate the heaviest mass regions.

In order to fully explain the s-process contribution to the abundance curve, it becomes apparent that separate “components” of neutron densities are necessary [17]. Each component corresponds to a different exponential neutron exposure, as a direct result of specific stellar scenarios, and is responsible for a separate portion of the s-process abundance curve. The curve displayed in Figure 1.7 depicts the solar distribution of s-only nuclei, N_s , multiplied by the neutron cross section, σ . A single neutron exposure was shown incapable of reproducing the abundances [18]. However, later work established how multiple exposures can reproduce the abundance curve of Figure 1.7 and even the likely sites for the source of these exposures [17, 19–21]. Table 1.5 lists the neutron exposures required by each component of the s-process.

Component	τ_0 (mb ⁻¹)	Source
Weak	0.06	He-burning in massive stars
Main	0.3	AGB stars
Strong	7.0	

Table 1.5: Neutron Exposures [17]

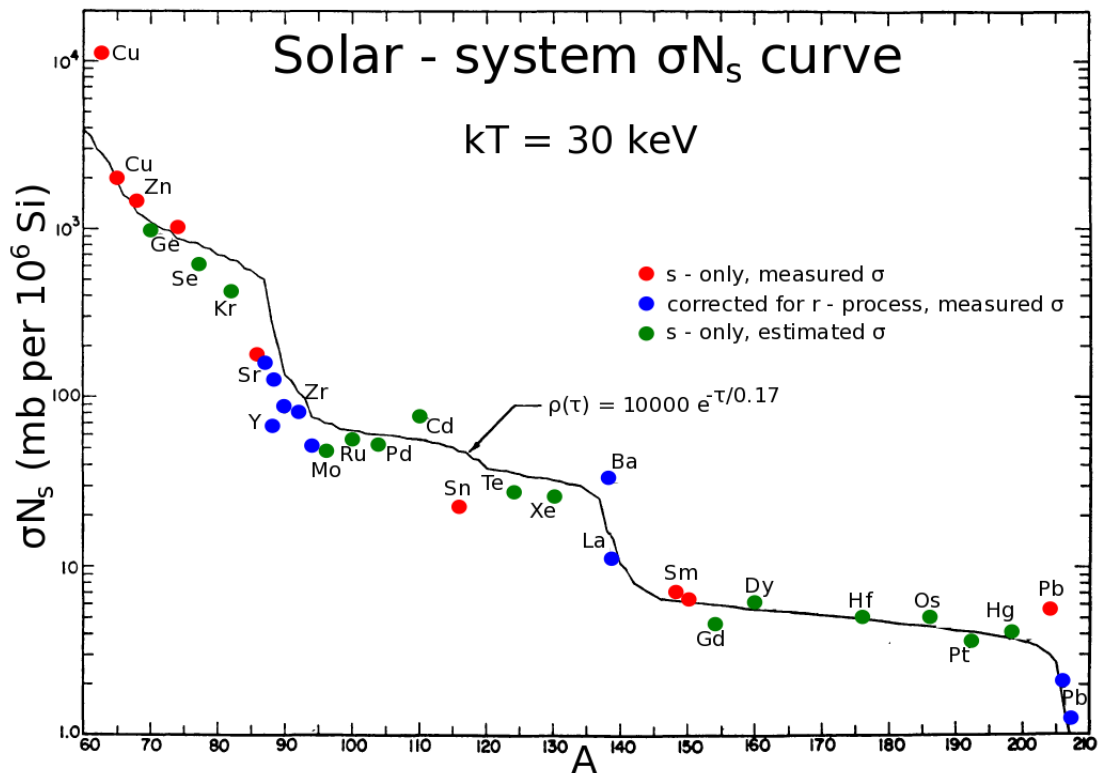


Figure 1.7: The product of s-only nuclei abundances and their neutron-capture cross section, σN_s , for Solar system abundances. The curve exhibits three distinct exponentials, which each correspond to a separate neutron exposure, τ_0 . Amended from [19].

The lowest “extra-Fe” nuclei are synthesised through the “weak” s-process during the pre-supernova evolution stages of massive stars ($M \geq 13M_{\odot}$). These same stars will also later contribute to the total isotopic abundances through the r-process, but their donations to s-process abundances occur in the mass range of $60 \leq A \leq 90$, around iron to strontium [22]. Occurring at the end of the helium burning stage, the star is hot enough that the $^{22}\text{Ne}(\alpha, n)^{25}\text{Mg}$ reaction is activated and drives the s-process as the main neutron source [23].

For the next section of the abundance chart, the stellar scenario changes to one that shoots out from the main sequence, the Asymptotic Giant Branch (AGB). The main s-process is the source of production for mass $90 \leq A \leq 204$, which is thought to occur primarily within the helium shell burning stages where the source of neutrons can be due to the $^{22}\text{Ne}(\alpha, n)^{25}\text{Mg}$ in more massive AGB stars or ^{13}C for $M_{AGB} < 3M_{\odot}$. The lower mass AGB stars do not reach sufficient temperatures for $^{22}\text{Ne}(\alpha, n)^{25}\text{Mg}$ to be the main neutron source and so (α, n) reactions on ^{13}C is the more favoured theory [17].

A separate strong s-process component is also sometimes discussed, although the need for a separate stellar scenario from the main component is in some doubt. This final component provides those heaviest s-process nuclei with the mass range of $204 \leq A \leq 209$, terminating with the heaviest stable isotope ^{209}Bi . Since the capture of a further neutron onto ^{209}Bi would result in ^{210}Bi , which is unstable to α emission and decays to ^{206}Pb , a final n-capture/ α -decay cycle will be the conclusion of the s-process. This end-stage is discussed in [20] alongside its effect on the abundance of Pb.

1.2.2.3 S-, R- and P-nuclei

It becomes an obvious conclusion that the r-process will populate nuclides that the s-process cannot possibly reach, since the decay would occur before the s-process can induce further captures. These r-nuclei inhabit most of the heavy, neutron-rich portion of the Segrè chart and are a result of successive β decays occurring as the r-process approaches the boundaries of the chart. What is less clear is that there also exist s-only nuclei, where only the s-process can account for their abundance.

Magic number	s-Process	r-Process
50	$^{88}\text{Sr}, ^{89}\text{Y}, ^{90}\text{Zr}$	^{80}Zn
82	$^{138}\text{Ba}, ^{139}\text{La}, ^{140}\text{Ce}$	$^{130}\text{Te-Xe}$
126	$^{208}\text{Pb}, ^{209}\text{Bi}$	$^{195}\text{Os-Pt}$

Table 1.6: The additional stability afforded by a completely closed neutron shell explains the increased abundances of certain heavy elements. That these shells are closed at different rates due to the respective neutron fluxes of the s- and r-processes explains the double peak features seen in the abundance curve.

This can be explained by examining Figures 1.5 and 1.6, as well as Figure 1.8 which displays a small section of the chart of the nuclides. Clearly visible are the successive β decays populating the isobaric chains, the r-nuclei. For the most part, these chains continue right up to the valley of stability, populating the nuclei labelled “s, r”, however a few notable cases are labelled simply as “s only”. When examining the stable isotopes on the full chart of the nuclides it can be seen that there are a greater number of stable isotopes for those elements with an even atomic number. Conversely, odd-Z elements tend to have few stable isotopes, often only one. The other line to consider aside from equal proton number, would be nuclei of equal mass, the isobars, the diagonal lines of β^- decay. Similar to what is found with the isotopes, isobars of odd mass number have fewer stable nuclei than those of even mass. For those isobaric lines with multiple stable isobars, it is clear that only the first, the most neutron-rich (or proton-deficient) can be

Chapter 2

Astrophysical Motivation

“I have always thirsted for knowledge, I have always been full of questions.”

- Hermann Hesse, Siddhartha

2.1 Impact of ^{17}O

The abundance of free neutrons within the stellar environment directly affects the final nuclear abundances at the end of the star’s life. As we are concerned in this case with stars and their associated neutron flux, we are, of course, discussing the impact upon the s-process nuclei. The background to this work began in earnest with an investigation into the specific case of rotating, massive stars at low metallicity [22], where metallicity is a measure of the proportion of nuclei within the stellar interior that are neither hydrogen nor helium. Stars containing these low quantities of metals are those that are both very large and very old, the first stars of the universe.

Chapter 1 established that massive stars play a substantial role in nucleosynthesis both in terms of the r-process once the star reaches supernova and more importantly, as far as this thesis is concerned, with the weak s-process. The contribution to s-process abundances in this case comes not from a significant source of neutrons (the exposure is relatively weak) but more crucially the metallicity, which both acts as the s-process seed and provides a secondary neutron source. With the introduction of rotation, the situation becomes very different. The weak s-process, that of the massive star, is dependent upon $^{22}\text{Ne}(\alpha, n)^{25}\text{Mg}$ as its neutron source and therefore does not begin until the star reaches a sufficiently high temperature to ignite the reaction. It is clear that s-process production should be proportional to the mass of the star; the more massive a star, the more neutrons released via ^{22}Ne [22].

After the star's mass, the second part of this special case is that the star is rotating. This has the effect of breaking down the barriers formed in shell burning, allowing for far greater mixing of nuclear species in convective zones. The standard, or non-rotating s-process is limited to the main neutron source, ^{22}Ne , a secondary nucleus produced as a result of the CNO cycle [24]. With the case of low metallicity stars, this neutron source is obviously removed, and the s-process will be far less efficient as a result. However, once the concept of rotation is introduced, the reliance on the two-step process is removed. The increased helium convective zone also leads to a higher core temperature than the non-rotating star [25]. The burn-up of the ^{22}Ne neutron source is proportional to the stellar mass, and therefore the stellar temperature. So, the introduction of rotation acts to increase the ^{22}Ne burn-up and consequentially leads to higher neutron flux.

Finally the consequences of this being applied to a star of low metallicity must be considered. Obviously in the standard s-process the answer is simply that the neutron sources are not present, and indeed the weak s-process efficiency is very low.

Although not as great as those of heavy, “beyond-iron” nuclei, low-mass isotopes tend to have substantial neutron cross sections, a fact that engineers frequently make use of in reactor physics applications (the boronated-water safety systems spring to mind [26, 27]). A portion of the chart of the nuclides is included as Figure 2.1, depicting the relative capture cross sections for thermal neutrons on low mass isotopes. In the stellar interior, at the evolution stage of interest, the abundance of these light nuclei is significant enough that when the minimal neutron exposure of the weak s-process [17] is taken into account, it becomes necessary to investigate the consequences regarding nucleosynthesis.

Our previously mentioned primary neutron source, the $^{22}\text{Ne}(\alpha, n)^{25}\text{Mg}$ reaction, comprises two potentially major neutron absorbers, or poisons, ^{22}Ne and ^{25}Mg . In fact, ^{25}Mg alone is thought to account for more neutron absorption than all $A \geq 56$ nuclei [28]. To lean the discussion back towards the main focus of this thesis we should consider the products of helium burning, ^{12}C and ^{16}O . These too can be considered a potential neutron poison despite their relatively low thermal-neutron capture cross section (^{12}C : 3.5 mb, ^{16}O : 0.19 mb compared to ^{22}Ne : 52.7 mb and ^{25}Mg : 190 mb [29–31]) which is compensated for by their abundance at the end of the helium burning stage.

The status of a nuclide as a neutron “poison” or merely an absorber is determined by the efficiency by which the captured neutrons might subsequently be recycled into the stellar interior. Note, once a neutron has been captured it becomes indistinguishable from any other neutron within the nucleus, so to say it might be re-emitted would be inaccurate. Within this work, “poison” is used to describe a nucleus which removes neutrons from circulation, for example, due to a radiative capture reaction. Conversely, “absorber” will

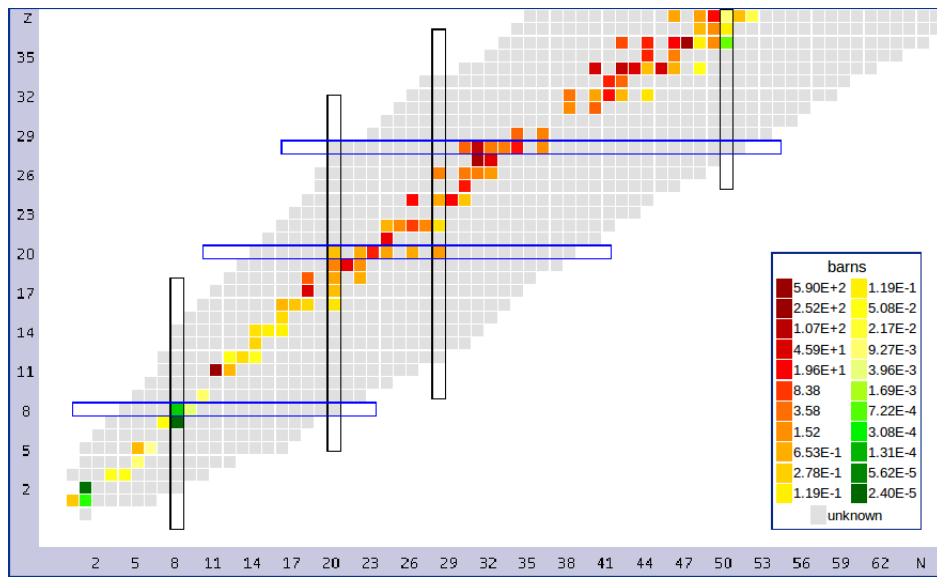


Figure 2.1: Plot of neutron number (x-axis) versus proton number (y-axis) and the relative thermal neutron capture cross sections of these low-mass nuclides amended from the NuDat 2.6 nuclear structure database [30].

generically refer to those nuclei that either contribute to s-process abundances as seeds, or those that recycle captured neutrons. The aforementioned (α, n) reactions, our primary neutron source, are responsible for this neutron recycling. The example of ^{12}C leads to the $^{13}\text{C}(\alpha, n)^{16}\text{O}$ reaction, which neatly approaches the experimental subject matter of this thesis. The capture of a neutron on ^{16}O obviously results in ^{17}O , which might then undergo a further helium capture reaction. These steps are displayed in Figure 2.2.

It becomes apparent that a critical value might be that of the (α, γ) to (α, n) ratio on ^{17}O , certainly with regards to the s-process nuclei abundances. Due to the interaction being a result of the strong force, it is clear from examining Table 2.1 that the $^{17}\text{O}(\alpha, n)^{20}\text{Ne}$

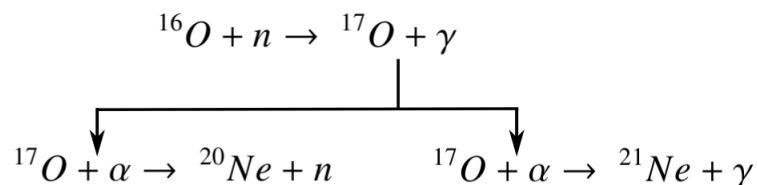


Figure 2.2: A simple representation of the reaction chain leading to ^{16}O being defined as either a neutron poison or absorber.

Interaction	Relative Strength	“Reactions involving”
Strong	1	α
Electromagnetic	10^{-2}	γ
Weak	10^{-14}	β
Gravitational	10^{-40}	~

Table 2.1: The relative strengths of interactions due to the four fundamental forces of nature. For example, the $^{17}\text{O}(\alpha,\gamma)^{21}\text{Ne}$ reaction, being a result of electromagnetic interaction, will be dominated by the strong force driven $^{17}\text{O}(\alpha,n)^{20}\text{Ne}$ reaction [32, 33].

reaction will dominate the $^{17}\text{O}(\alpha,\gamma)^{20}\text{Ne}$ reaction. In practice the branching ratios will be manifest in the partial widths for the neutron and γ channels, with the former being significantly larger than the latter (see Section 3.3.2). This dominance of the (α,n) channel allows for continued recycling of the neutron flux. What is less clear is the relative strength of the competing γ channel. If the ratio between the two channels remains as straightforward as the general case, then there would be a negligible effect on the final s-process abundances. However, any sufficiently strong resonance could possibly play a role, increasing the contribution from the γ channel, which would obviously remove neutrons from later s-process reactions.

2.2 The status of the $^{17}\text{O}(\alpha,\gamma)/(\alpha,n)$ ratio

Prior to the commencement of this work, data on the subject were sparse. No measurements had been made of the specific (α,γ) channel, and the most comprehensive work on the (α,n) reaction was found in an unpublished thesis by Denker [34, 35], investigating the energy range $0.521 < E_{cm} < 1.605$ MeV. Other preceding studies had taken place on the (α,n) reaction [36, 37] but across a range of energies far higher than those of interest, i.e. above the Gamow window, and with worse resolution of the excitation function (the work of [35] presenting over 400 individual measurements), thus removing any detail of resonant structures. As a result, in order to calculate the $^{17}\text{O}(\alpha,\gamma)^{21}\text{Ne}$ reaction rate, and the final s-process abundances, a reliance on approximations and theoretical models was required, a far from ideal situation. These data are displayed as S-factors in Figures 2.3 and 2.4. The first plot, Figure 2.3, highlights the agreement of the various (α,n) measurements/predictions when compared to the contrasting values for the (α,γ) reaction. Figure 2.4 shows only the experimental (α,n) data of Denker, Bair and Hansen and their respective energy ranges in relation to the Gamow window.

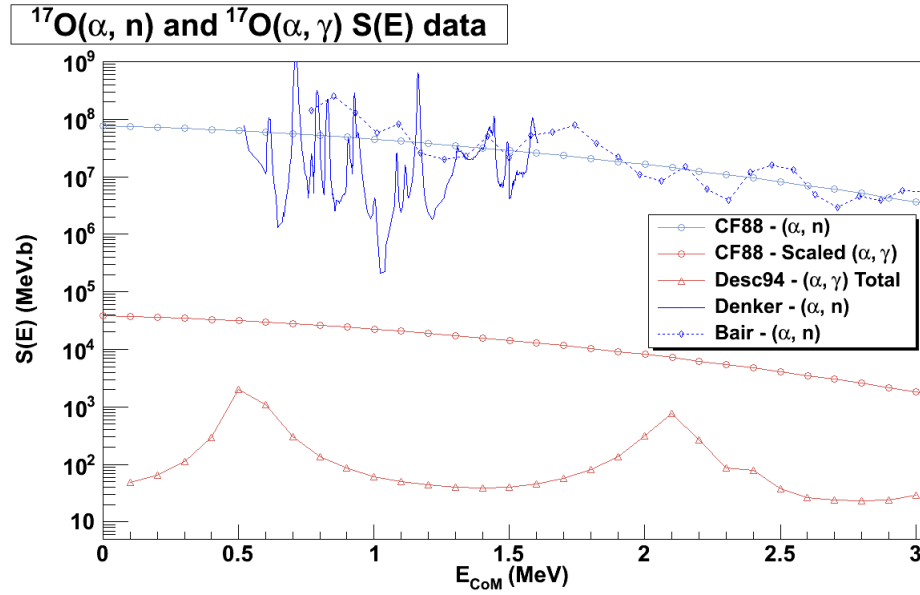


Figure 2.3: Previous status of $^{17}\text{O}(\alpha, \gamma)$ and $^{17}\text{O}(\alpha, n)$. The blue points represent (α, n) data while the (α, γ) is depicted by red points. The theoretical models are displayed as circles for CF88 and triangles for Descouvemont. The CF88 (α, γ) points come from a scaling of 5×10^{-4} across the full range of the (α, n) data [34–36].

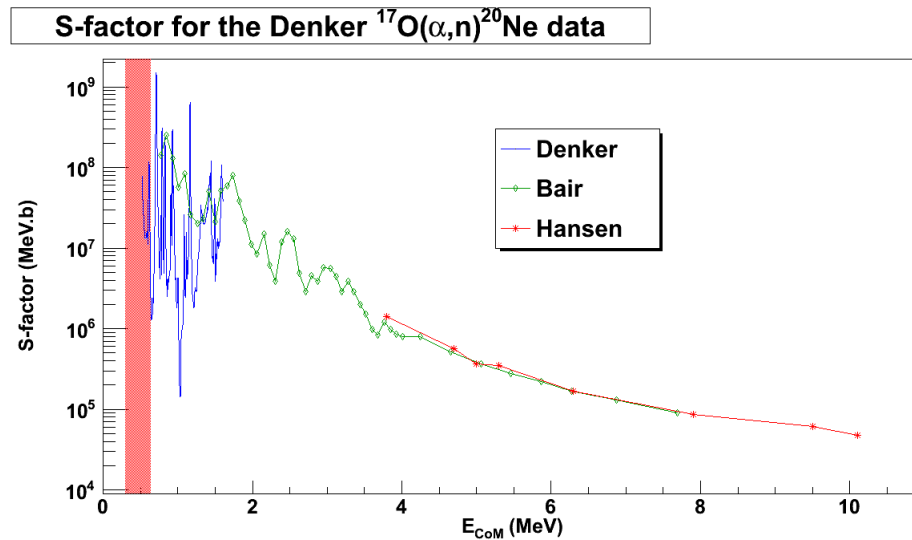


Figure 2.4: Experimental data taken for the $^{17}\text{O}(\alpha, n)^{20}\text{Ne}$ reaction, showing how the respective excitation functions compare to the region of astrophysical interest highlighted in red [34–37].

2.2.1 Estimated Reaction Rate

The first $^{17}\text{O}(\alpha,\gamma)^{21}\text{Ne}$ reaction rate made available for use in network calculations is CF88 [38–42]. This is the most recent edition of a series of reaction rate tables that are based on the work of Caughlan, Fowler and Zimmerman’s discussion on Thermonuclear Reaction Rates in 1967 [38]. The $^{17}\text{O}(\alpha,\gamma)^{21}\text{Ne}$ reaction was first discussed in the second of these articles [39], highlighting the lack of experimental data available to make the calculations of reaction rate. In fact, so sparse is the available data that the article introduces an approximation to its theoretical model for a number of $(\alpha,\gamma)/(\alpha,n)$ ratios including the $^{17}\text{O}+\alpha$ system.

At the time of the compilation of [39], calculations based on experimental data had been performed on the analogous $^{18}\text{O}(\alpha,\gamma)^{22}\text{Ne}$ reaction showing that the ratio to the corresponding (α,n) channel was $\sim 5 \times 10^{-4}$ for energies above the neutron threshold. In this case, the neutron emission cross section is approximately equal to the total cross section due to the negligible contributions of both the γ and α emission channels. However, below the threshold, the neutron cross section is obviously zero so the γ channel, being unimpeded by the Coulomb barrier, is taken to be approximately equal to the total cross section. For high temperatures, the ratio of 5×10^{-4} is taken to be true also for $^{17}\text{O}(\alpha,\gamma)/(\alpha,n)$ (plus other systems not important for this thesis). It is also noted that, as is the case with $^{18}\text{O}(\alpha,\gamma)/(\alpha,n)$, for low energies (defined in [39] as lower than ~ 1 MeV), Hauser-Feshbach calculations produce (α,γ) cross sections that are a “substantial fraction of the corresponding (α,n) cross sections”.

2.2.2 Theoretical Model: Generator Coordinate Method

The system was not investigated again until a newer theoretical approach by Descouvemont was attempted in 1993 [43] using the generator coordinate method. The microscopic three-cluster model is fully described in [43, 44] but relevant to this thesis is the case of the ^{21}Ne system, specifically the combination of ^{16}O , α and n particles. A microscopic model determines the cross section of a reaction through an investigation of both the nucleon-nucleon interaction and the appropriate, antisymmetrized wave functions. Fully antisymmetrized wave functions are determined from the possible coupling modes of ^{21}Ne , those of $(\alpha + ^{16}\text{O}) + n$ and $(n + ^{16}\text{O}) + \alpha$. In terms of the effect on low energy radiative capture reactions, the antisymmetrization is largely reaction-dependent [44].

While Descouvemont seems to be in agreement with the CF88 technique at the higher energies, for the stellar environment of interest there remains a significant discrepancy. Using the GCM, the prediction for the (α,γ) reaction rate is one greatly reduced from

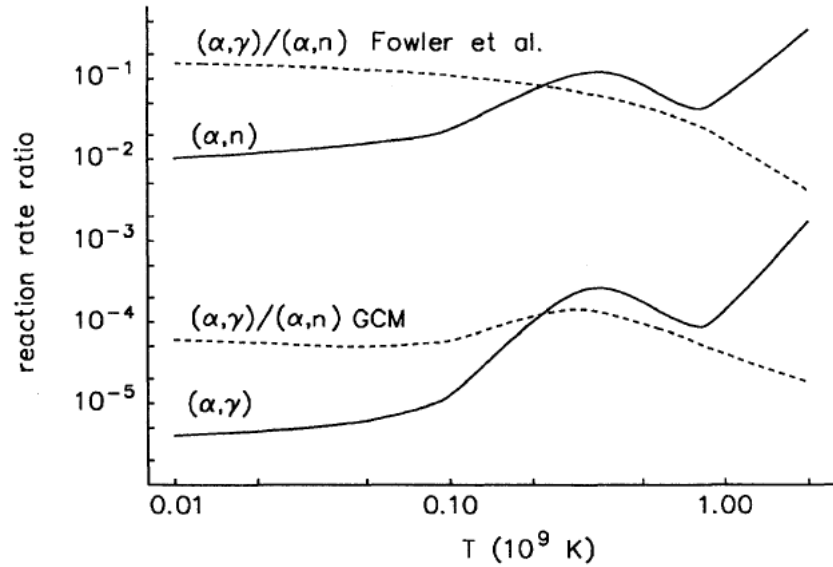


Figure 2.5: Comparison of the GCM and CF88 $^{17}\text{O}(\alpha,\gamma)/(\alpha,n)$ reaction rates. The solid lines represent the ratio of the GCM to the CF88 values for each reaction, whereas the dashed lines present the $(\alpha,\gamma)/(\alpha,n)$ ratio for each technique [43].

the “significant fraction” of CF88. Indeed, across the full temperature range, the GCM ratio is flatter and exhibits a shallow drop-off towards higher temperatures; this is clear in Figure 2.5.

2.3 S-process abundances

In the absence of an experimental value of the strength of the (α,γ) channel there is no option but to make a guess, albeit a highly-educated one. The paper that spurred the interest in this work examined the results of the two options presented thus far. What would be seen should the CF88 assumption be correct? Conversely, what differences would the GCM produce? This is discussed fully in [22] and their key results are presented as Figure 2.6. However, the effect of each model is clear to be seen. With the lower neutron exposure predicted from the CF88 estimate, the s-process is much less efficient, and produces an underabundance of elements between strontium and barium as a result of the strong $^{17}\text{O}(\alpha,\gamma)^{21}\text{Ne}$ channel. Conversely, the reduced Descouvemont GCM reaction rate allows seed nuclei a greater neutron exposure, thus improving s-process efficiency and the resultant effect on those same abundances is apparent. The difference between the two theoretical predictions has been shown to be up to 10^3 for the highest mass weak s-

process nuclides. It is clear to see that the $^{17}\text{O}(\alpha,\gamma)^{21}\text{Ne}$ reaction rate is a critical parameter in these calculations and therefore it was necessary to perform an accurate measurement to reduce this uncertainty.

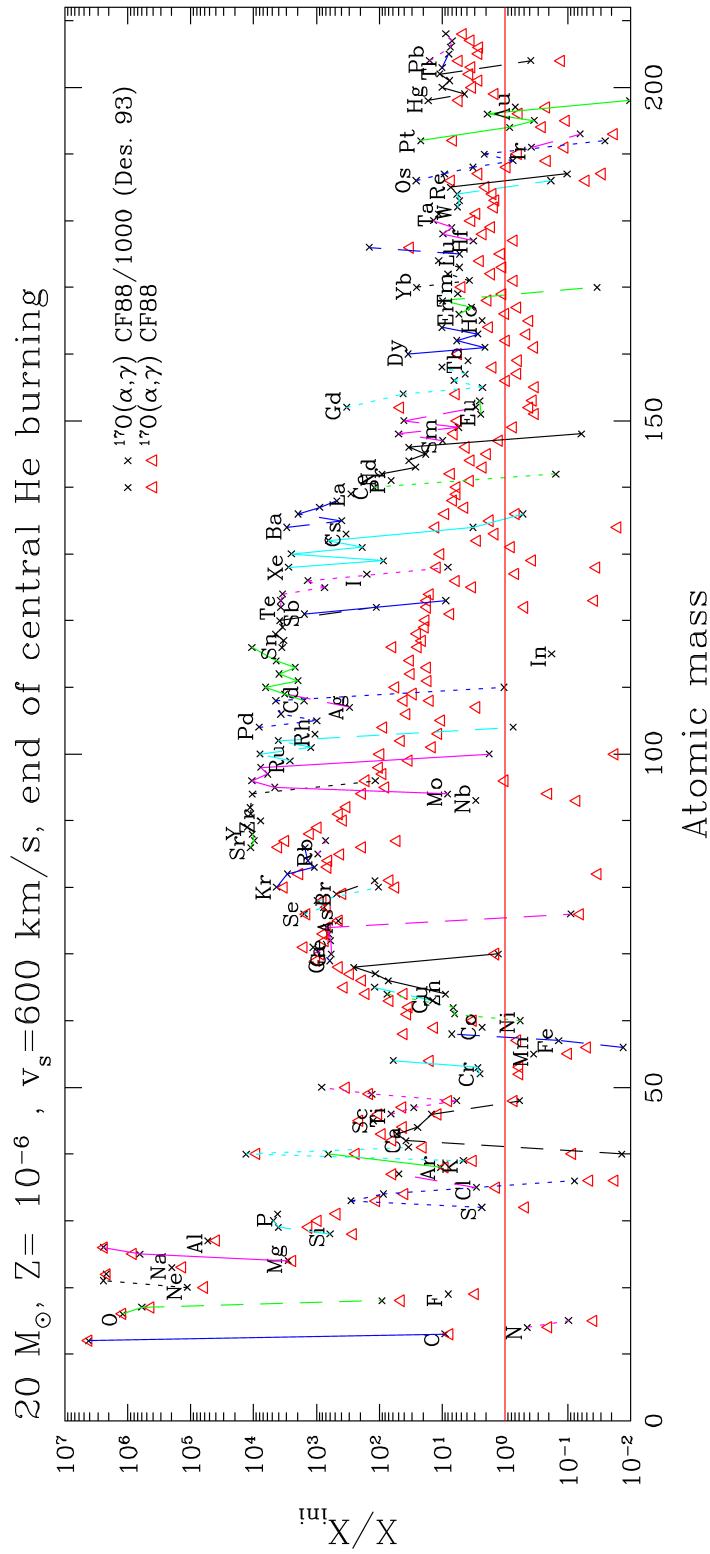


Figure 2.6: S-process overproduction as a fraction of the initial isotopic abundances for the rival theoretical models. The black crosses represent a lower (Descouvemont) reaction rate compared to the red triangles for the stronger, CF88, (α, γ) channel. The Descouvemont GCM produces significantly higher abundances from strontium and barium [22].

Chapter 3

Nuclear Theory

“Don’t spend too much time learning theory. It can’t all be right.”

- Prof. John Wood

3.1 Cross Section

The most fundamental property of a given reaction is its probability of occurrence. This probability of interaction is known as the cross section. The slightly unusual term stems from the classical interpretation and analogy with shooting at a target where the probability increases with the geometrical area of both projectile and target. The classical, or geometric, cross section, σ , is due to the combination of the areas of the two reacting nuclei. Simply, if the projectile and target have radii R_p and R_t , determined through:

$$R = R_0 A^{1/3}, \quad (3.1)$$

where $R_0 \sim 1.2\text{fm}$ and A is the atomic mass number of each nucleus, then the classical cross section is given by:

$$\sigma = \pi(R_p + R_t)^2, \quad (3.2)$$

as the region of overlap.

This explains the name “cross section” for what is in reality a probability. The units of cross section are metres-squared, although with the order of magnitude for the cross section of even the largest nucleon-nucleon interaction being 10^{-28}m^2 the unit of nuclear

area is defined as the barn (b), where $1\text{b} = 10^{-28}\text{m}^2$, for convenience of use.

However, only the classical approach has been considered, whereas the effects of quantum mechanics need to be included for the more correct cross section to be determined. An energy dependence must be introduced, and this is done by using the de Broglie wavelength, λ , which allows the quantum mechanical wave nature of the reactants to be taken into account. Therefore Equation 3.2 becomes Equation 3.3:

$$\sigma = \pi\lambda^2 \quad (3.3)$$

$$\lambda = \frac{m_p + m_t}{m_t} \frac{\hbar}{(2m_p E_l)^{1/2}} \quad (3.4)$$

where λ is the de Broglie wavelength given by Equation 3.4, with the energy of the projectile in the laboratory frame, E_l , the masses of the projectile and target, m_p and m_t , and the constant \hbar the remaining terms.

In terms of experimental analysis, and any calculations required, it is clear that none of the above definitions is of a suitable form from which a value for σ can be determined. The cross section can be succinctly defined as the reaction probability per unit incident flux per target nucleus. From this definition, a formula can be determined. Taking the input parameters of incident beam nuclei, i , and number of target nuclei per area, n , it is clear that the only remaining term to establish the interaction probability would be the primary measurement value, that of the number of outgoing recoil nuclei, the yield, Y . This presents the cross section as the ratio of “output” to “input” nuclei depicted as:

$$\sigma = \frac{Y}{ni} \quad (3.5)$$

which is possibly the most simple equation to be found within this work, although naturally, each variable is somewhat more complicated to determine and shall be dealt with in the forthcoming chapters.

3.2 Astrophysical S-factor

The cross section is not always the most straightforward value with which to interpret results. Whilst varying relatively smoothly at high energies, the cross section plummets at low energy due to the increasingly significant effect of the Coulomb barrier. The exponential nature of the transmission probability is described by the Gamow factor, $e^{-2\pi\eta}$, an approximation for sub-barrier s-wave transmission, with the s-wave describing an interaction with the lowest angular momentum transfer. As a result, the cross section tails off exponentially with decreasing energy making accurate, statistically significant, measurements difficult to obtain at the lowest energies. Furthermore, in the absence of data taken in the energy region of interest, one is required to make an extrapolation down to these energies. Since the cross section function contains an exponential component, thus varying strongly with energy, this extrapolation becomes increasingly less reliable and more problematic by introducing greater uncertainties, something the experimental campaign was proposed to reduce.

The standard practice is to make use of the astrophysical S-factor, which removes the well-understood, non-nuclear component of the cross section. By extracting the s-wave barrier penetrability, and therefore the dominant energy dependence, the effect is a flattening out of the excitation function to become far more stable with varying energy. This nuclear-specific term is

$$\sigma(E) = \frac{1}{E} e^{-2\pi\eta} S(E), \quad (3.6)$$

where the exponential factor, as discussed, is a result of the penetrability of the Coulomb barrier, but also includes a $1/E$ dependence due to the incident particle wavelength. Some further discussion should be directed towards the Gamow factor, specifically to define the Sommerfeld parameter, η , as:

$$\eta = \frac{Z_0 Z_1 e^2}{\hbar} \left(\frac{\mu}{2E} \right)^{\frac{1}{2}}, \quad (3.7)$$

with the energy dependence, a reduced mass term, μ , the product of the reactants atomic numbers and e and \hbar , which have their usual definitions.

The effect of removing these dominant energy dependences is particularly apparent for non-resonant, or flat, excitation functions with the smoothly varying function of beam energy becoming a useful tool in our extrapolation. This result can be seen in both of the

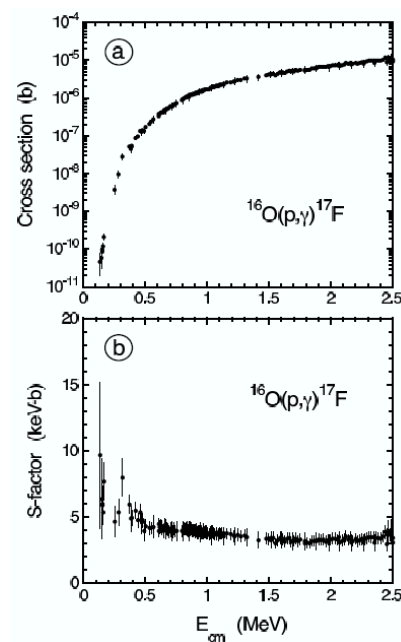


Figure 3.1: Comparison of cross section (a) and S-factor (b) for the $^{16}\text{O}(p,\gamma)^{17}\text{F}$ reaction. The difference in respective energy dependence is quite clear, with the astrophysical S-factor a far smoother function of energy [45].

example functions taken from [45, 46] in Figure 3.1 and by comparing the plots produced from this work's data in Figures 6.1 and 6.2 in the results chapter.

3.3 Thermonuclear Reaction Rate

The reaction rate is defined as the number of reactions that occur per unit time. Analogous to the definition of the yield/cross section relation, a similar formula defining the rate of nuclear reaction can be given as:

$$r_{01} = N_0 N_1 v \sigma(v), \quad (3.8)$$

with terms N_0 and N_1 being the number densities of the interacting particles in the centre of mass frame and with the reaction rate r_{01} also being due to the cross section, σ , it should be trivial to draw parallels between Equations 3.5 and 3.8. For all intents and purposes, here energy and velocity are practically synonymous, and so the velocity term, v , dictates that the reaction rate must also exhibit some energy dependence.

3.3.1 Non-resonant Reaction Rate

Within the stellar environment, indeed, any stellar environment (with the few obvious exceptions where the nuclei are degenerate and move relativistically [47]), not solely that described in Chapter 2, the particles will have a range of speeds which can be described by a Maxwell-Boltzmann distribution. However, since the probability of interaction depends on the relative speed between nuclei of independent Maxwell-Boltzmann speed distributions, then it follows that the distribution, $\phi(v)$, should be given by:

$$\phi(v)dv = \left(\frac{\mu}{2\pi kT}\right)^{3/2} \exp\left(-\frac{\mu v^2}{2kT}\right) 4\pi v^2 dv, \quad (3.9)$$

where μ is the reduced mass and v is the relative speed.

By introducing the speed distribution into the equation for non-resonant reaction rate the speed and cross section terms, v and $\sigma(v)$, in Equation 3.8 can be replaced with the “reaction rate per particle pair”, $\langle\sigma v\rangle$, to give:

$$\langle\sigma v\rangle = \int_0^\infty \phi(v)v\sigma(v) dv, \quad (3.10)$$

which nicely becomes:

$$R = N_x N_y \langle\sigma v\rangle. \quad (3.11)$$

By substituting Equation 3.9 into Equation 3.10, the thermonuclear reaction rate per particle pair is:

$$\frac{R}{N_x N_y} \equiv \langle\sigma v\rangle = 4\pi \left(\frac{\mu}{2\pi kT}\right)^{3/2} \int_0^\infty v^3 \sigma(v) \exp\left(-\frac{\mu v^2}{2kT}\right) dv. \quad (3.12)$$

The Maxwell-Boltzmann energy distribution is a special case of the Boltzmann distribution where $E = \frac{1}{2}\mu v^2$. If this relationship is used to change the integrating variable to energy, so that the speed distribution component is now written as an energy distribution, Equation 3.12 becomes:

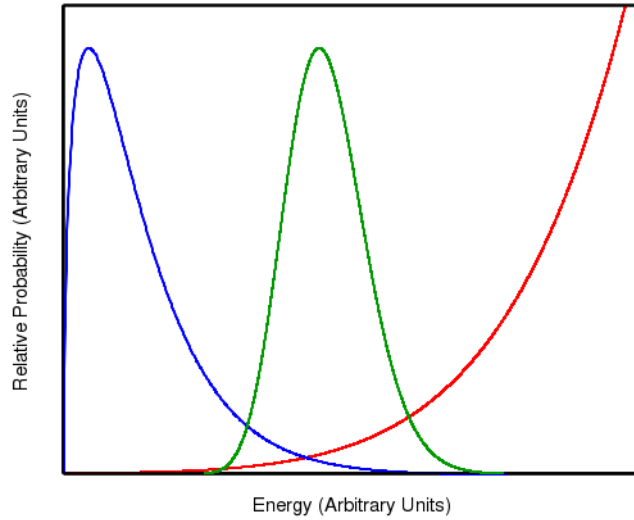


Figure 3.2: Convolution of the Maxwell-Boltzmann energy distribution (blue line) for charged particles with the probability of quantum mechanically tunneling through the Coulomb barrier (red line), as discussed in Chapter 2. This results in what is known as the Gamow peak, the energy region where the reaction occurs in stellar burning (green line).

$$\langle \sigma v \rangle = \left(\frac{8}{\mu\pi} \right)^{1/2} \frac{1}{(kT)^{3/2}} \int_0^{\infty} \sigma(E) E \exp\left(-\frac{E}{kT}\right) dE, \quad (3.13)$$

which numerically will yield reaction rate of:

$$N_A \langle \sigma v \rangle = \frac{3.7318 \times 10^{10}}{T_9^{3/2}} \sqrt{\frac{M_0 + M_1}{M_0 M_1}} \int_0^{\infty} \sigma(E) E \exp^{-11.605E/T_9} dE, \quad (3.14)$$

for a given temperature T_9 . In Equation 3.14 the centre-of-mass energy E is in units of MeV, the relative atomic masses M_i in u, the cross section σ is in barns and the reaction rate $N_A \langle \sigma v \rangle$ in $(\text{cm}^3 \text{mol}^{-1} \text{s}^{-1})$.

To take a slight step back, Figure 3.2 shows the energy distribution of the reacting species depicted by the blue line. This simply stems from Equation 3.9 being written as a function of energy. As previously discussed, the distribution of energies takes the shape of a Maxwell-Boltzmann curve and peaks at $E \sim kT$, therefore the majority of the particles

are at low energies. This point is pressed as one must now recall the earlier discussion of the issue of heavy element fusion and the presence of the Coulomb barrier. The barrier is also represented in Figure 3.2 by its probability of penetration, in this case depicted by the red line, and it is clear that most of the particles are at energies where the Coulomb barrier penetration probability is very low indeed.

This allows an important conclusion to be drawn; if the majority of reactants occur at extreme sub-barrier energies where their interaction must be greatly impeded, yet due to the existence and abundance of metals it is known that such reactions take place, then it stands to reason that there must be a favourable energy region.

If Equation 3.6 is substituted into Equation 3.13, then the integrand of:

$$\langle \sigma v \rangle = \left(\frac{8}{\pi \mu} \right)^{1/2} \frac{1}{(kT)^{3/2}} \int_0^{\infty} e^{-2\pi\eta} S(E) e^{-E/kT} dE \quad (3.15)$$

contains the energy dependence of the reaction rate.

Clearly, at high energies the contribution from the Maxwell-Boltzmann distribution will be negligible; likewise at low energies the same is true for the penetrability term, the region of interest therefore must occur where the product of the integrand is at its maximum [46]. This region is the third line displayed on Figure 3.2 and describes the convolution of the Maxwell-Boltzmann distribution and the Coulomb barrier penetration. It occurs where there exists a balance between the opposing effects of needing a sufficiently high energy that the Coulomb barrier can be penetrated at a reasonable frequency but one that is low enough that there are simply enough particles available to react.

It follows that this region of balance between the conflicting energy dependences is in fact the energy range over which the vast majority of reactions will occur within the stellar interior. This energy, known as the Gamow energy, derives its name from the Gamow factor from the integrand of Equation 3.15, where the formula:

$$E_G = 0.1220 \left(Z_0^2 Z_1^2 \mu T_9^2 \right)^{1/3}, \quad (3.16)$$

stems from the first derivative. The effect of the Gamow, or penetrability, term is therefore to move the effective burning energy from $\sim kT$ to the higher energy of E_G . Also introduced is the width of the Gamow peak, which itself has been approximated by a Gaussian, known as the Gamow window, Δ , and is given by:

$$\Delta = 0.2368 (Z_0^2 Z_1^2 \mu T_9^5)^{1/6}. \quad (3.17)$$

Again this stems from derivatives of the integrand but this is described more fully in [46]. Note that in Equations 3.16 and 3.17, the units are both MeV.

The combination of the two energy-dependent functions leads to Equation 3.15 which folds in the earlier definition of the S-factor to present the non-resonant reaction rate as a function of the S-factor. This allows for a value for the reaction rate, at least the non-resonant contribution to be found numerically, provided that the full excitation function is known i.e. there must be knowledge of the S-factor across the entire energy range being investigated.

3.3.2 Isolated Narrow Resonances

When considering a full excitation function, the various features, namely the resonances related to states in the compound nucleus need to be taken into account. In this instance, it is the situation where the level density is low (isolated) thus minimising the influence of overlapping resonances and where the width of the resonance is small (narrow) that is of interest.

It is worth noting that while many interpretations for what constitutes a narrow resonance exist; this work will define a resonance as narrow “*if the corresponding partial widths are approximately constant over the total resonance width (or Γ less than a few keV)*” [46], and isolated where the spacing between states is greater than the width of the individual state. If the reader cares to skip ahead and examine Figure 3.6, they will see that these conditions are met for the majority of the relevant states. For the few that have larger widths (the $E_x = 8.008$ MeV state particularly stands out), the level density is still low enough that adjacent states do not appear to overlap. Furthermore, overlapping states of different J^π values do not interfere across the angle-integrated cross section [46]. Therefore, the total cross section is described by an incoherent sum of their one-level Breit-Wigner contributions.

It becomes important to describe the physical shape of these resonances. Fortunately this is provided by the (previously mentioned) Breit-Wigner formula as:

$$\sigma_{BW}(E) = \frac{\lambda^2 (2J + 1)(1 + \delta_{01})}{4\pi (2j_0 + 1)(2j_1 + 1)} \frac{\Gamma_a \Gamma_b}{(E_r - E)^2 + \Gamma^2/4} \quad (3.18)$$

where J, j_0 and j_1 are the spin of the compound and reactant nuclei respectively, λ is the de Broglie wavelength, and Γ, Γ_a and Γ_b are the total width of the state and the partial widths of the relevant channels involved (in the case of this work that would be the α - and γ -channels). It should be noted that the widths of the channels are implicitly energy dependent. Equation 3.18 also introduces a new symbol, δ_{01} , the Kronecker delta, which has its standard definition of:

$$\delta_{ij} = \begin{cases} 0 & \text{for } i \neq j \\ 1 & \text{for } i = j \end{cases} \quad (3.19)$$

which accounts for the situation of identical particles in the entrance channel which has the effect of doubling the cross section due to the ‘‘beam’’ and ‘‘target’’ nuclei being indistinguishable.

Substitution of Equation 3.18 into Equation 3.14 provides the formula for the single narrow resonance reaction rate, and is given by:

$$N_A \langle \sigma v \rangle = \left(\frac{8}{\pi \mu} \right)^{1/2} \frac{N_A}{(kT)^{3/2}} \int_0^\infty E \sigma_{BW}(E) e^{-E/kT} dE \quad (3.20)$$

$$= N_A \frac{\sqrt{2\pi} \hbar^2}{(\mu kT)^{3/2}} \omega \int_0^\infty \frac{\Gamma_a \Gamma_b}{(E_r - E)^2 + \Gamma^2/4} e^{-E/kT} dE \quad (3.21)$$

with the parameter $\omega \equiv (2J + 1)(1 + \delta_{01}) / [(2j_0 + 1)(2j_1 + 1)]$. If the title of this section is now considered, for narrow resonances both the $e^{-E/kT}$ factor and the partial widths Γ_i are approximately constant across the resonance width. Replacing these terms with their value at E_r allows the integral to be calculated analytically, which leads to:

$$N_A \langle \sigma v \rangle = N_A \left(\frac{2\pi}{\mu kT} \right)^{3/2} \hbar^2 e^{-E_r/kT} \omega \gamma. \quad (3.22)$$

The resonance strength must then be introduced so that resonances of differing heights and widths may be compared. The resonance strength, now referred to as the $\omega\gamma$, is the integrated cross section for the resonance of interest, under the assumption that both λ and the decay widths are weakly energy dependent over the width of the resonance. It can also be expressed as the product of the maximum cross section and total width of the resonance [46] and given as:

$$\omega\gamma = \frac{(2J+1)(1+\delta_{01})}{(2j_0+1)(2j_1+1)} \frac{\Gamma_a\Gamma_b}{\Gamma} \quad (3.23)$$

One might conclude that, as is the case with $^{17}\text{O}(\alpha,\gamma)^{21}\text{Ne}$, without total knowledge of the full state information, the $\omega\gamma$ cannot be determined. However, the resonance strength can also be obtained from several measurable quantities [48] as:

$$Y = \lambda^2 \omega\gamma \frac{(M+m)}{m\epsilon} \quad (3.24)$$

where the yield, Y , de Broglie wavelength, λ , projectile and target masses, m and M respectively, are combined with the stopping cross section of the target, ϵ , which is defined as Equation 3.25. The stopping cross section itself is a function of number density, N , as given by:

$$\epsilon = \frac{1}{N} \frac{dE}{dx} \quad (3.25)$$

with the target energy loss represented by its usual symbols. It is worth highlighting at this point that the terms “stopping power” and “stopping cross section” are used somewhat interchangeably in texts [46], due to both functions experiencing only slight variation across a wide sample of absorbers for a given energy. It is important, however, that the reader be aware of the function in use for their own calculations.

Both the resonance strength and reaction rate are products of energy and cross section so it follows that a strong $\omega\gamma$ would be present for a strong reaction rate. When the resonances in the cross section are narrow and isolated, no interference occurs, so individual contributions are simply summed together. It is then possible to determine the respective contributions of each resonance in the excitation function through:

$$N_A \langle \sigma v \rangle = \frac{1.5399 \times 10^{11}}{\left(\frac{M_0 M_1}{M_0 + M_1}\right) T_9} \sum_i (\omega\gamma)_i e^{-11.605 E_i / T_9}, \quad (3.26)$$

which enables the total resonant reaction rate to be found. The terms of Equation 3.26 retain their usual definitions, with M_0 and M_1 the masses of the interacting nuclei, T_9 the stellar burning temperature in units of GK and E_i the centre-of-mass energy in units of MeV.

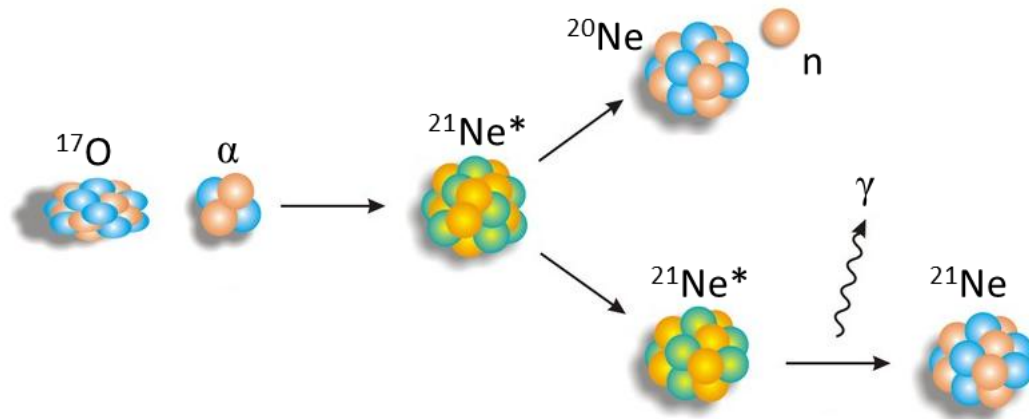


Figure 3.3: Cartoon of a radiative capture and compound nucleus transfer reaction.

Through using Equation 3.26 and assuming that the data describes a series of isolated resonances, a set of reaction rates can be produced to investigate the contributions of the different states across the full excitation function. Of course, this is not quite the finished result as there are both resonant and non-resonant contributions to consider, which data constitute which contribution is the topic of a later section. Obviously this is for the specific set of conditions where the resonances are both isolated and narrow; if these conditions are not present then the validity of this technique will be in question and an alternative would need to be sought.

3.4 Nuclear Reactions

There are many varieties of nuclear reaction, some involve species transmutation, others have no exchange of nucleons, but an energy transfer may possibly take place. These are all discussed in great detail in many other texts. Here, the main reaction of interest is the capture of an α particle with the emission of a γ ray, what is known as a radiative capture reaction.

The reaction mechanism is pictorially represented in Figure 3.3 where the difference between the two competing channels discussed in the previous chapter is apparent.

3.4.1 Reaction Energy

Within the stellar environment nuclear reactions provide the energy to oppose gravitational collapse, though this thesis is more interested with the secondary consequence of heavy element nucleosynthesis. The energy released by a reaction is due to the mass difference between the ingoing and outgoing nuclei. This was already alluded to in the introduction during the discussion of the binding energy per nucleon as the argument against fusion being the source of heavy element abundances.

The Q-value represents this release of energy, and is characteristic of the particular reaction. It is defined as the difference between the summed masses

$$Q = (\Sigma m_{initial} - \Sigma m_{final})c^2 \quad (3.27)$$

$$= (m_{^{17}\text{O}} + m_{\alpha} - m_{^{21}\text{Ne}})c^2. \quad (3.28)$$

which in the case of $^{17}\text{O}(\alpha,\gamma)^{21}\text{Ne}$ releases an energy of:

$$Q = (-0.8067) + 2.4249 - (-5.7317) \quad (3.29)$$

$$= 7.348 \text{ MeV}. \quad (3.30)$$

Reaction	Q-value (MeV)
$^{17}\text{O}(\alpha,\gamma)^{21}\text{Ne}$	7.348
$^{17}\text{O}(\alpha,n)^{20}\text{Ne}$	0.587

Table 3.1: The respective Q-values, the energy released, by the $^{17}\text{O}(\alpha,\gamma)^{21}\text{Ne}$ and $^{17}\text{O}(\alpha,n)^{20}\text{Ne}$ reactions for population of the ground state of the final system.

However, in terms of this work, the Q-value represents the kinetic energy carried away by the final products, be they the ^{21}Ne nucleus and accompanying γ ray, or the ^{20}Ne and emitted neutron. The effect of this energy is the subject of the next section.

3.4.2 Inverse Kinematics

The nature of this work is one that focusses solely on radiative capture measurements. In Chapter 4, the discussion will move to specifics of why and how the DRAGON facility is tailor-made for investigating these reactions. For this section, the background theory will continue to be presented.

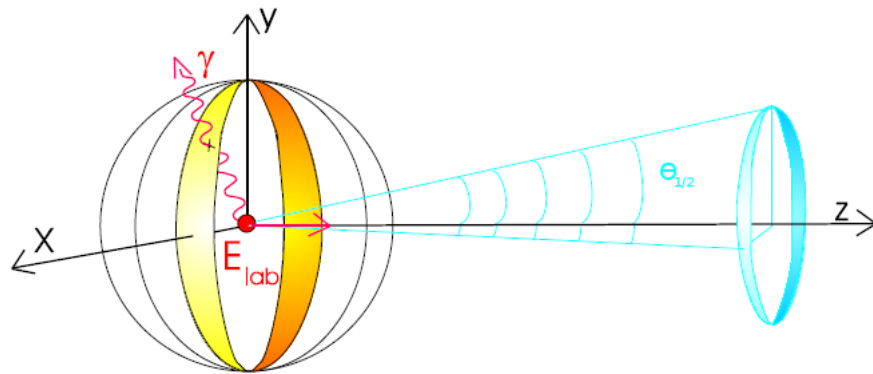


Figure 3.4: Representation of the reaction recoil cone and the influence of the de-exciting compound nucleus [52].

When Rutherford performed his early investigations it was the light α -particle that was the projectile incident upon the heavy gold-leaf target. This is known as direct kinematics. Unfortunately the term “direct reaction” is often used with many different definitions in several closely related fields, three of which appear in this thesis. However, in this instance it is the reaction of a light projectile nucleus on a heavy target nucleus which is termed direct kinematics.

With the advent of recoil separators, it is no longer always the best technique to use direct kinematics. By conservation of momentum, it can be shown that the recoil cone of a reaction in direct kinematics can be extremely wide; in fact this is literally what Rutherford was referring to when observing back-scattered α -particles. This poses a significant problem when dealing with a recoil separator as it has a fixed entrance aperture. Unlike arrays where the detectors surround the target mechanism and can therefore provide near- 4π coverage, as is the case with, say, TIGRESS, GAMMASPHERE or SHARC [49–51], recoils that occur at angles greater than the acceptance of the separator are lost. If the cross section, and therefore the expected yield are low, one cannot afford to lose any recoils due to acceptance issues.

The obvious solution to this problem is to allow physics itself to help the experimenter. By making use of inverse kinematics, i.e. where the projectile is the heavier nucleus, the distribution of recoil nuclei is naturally forward focussed. One might imagine the results of rolling a tennis ball into a bowling ball, and then vice-versa. The acceptance of the DRAGON facility is 20 mrad [53], a limiting value which is approached and then passed as the energy, and momentum, of the reaction decreases, and consequently the recoil cone

becomes less forward focussed. For the case of $^{17}\text{O}(\alpha, n)^{20}\text{Ne}$ a selection of recoil cone half-angles, $\theta_{1/2}$, are displayed in Table 3.2, but the important point is that the acceptance cone is breached with the energy of $E_{cm} = 0.931$ MeV. When investigating the Gamow window there is no option but to pass this limit. The situation is further worsened by the de-excitation of the recoil nucleus.

E_{cm} (MeV)	$\theta_{1/2}$ (mrad)
1.509	17.69
1.116	19.66
Acceptance	20
0.931	21.05
0.811	22.23
0.709	23.48
0.621	24.81

Table 3.2: Calculations of recoil cones for a selection of centre-of-mass energies. The inclusion of DRAGON's angle of Acceptance highlights the separation of energies into those where the recoil cone is wholly captured by the separator, and those where significant losses will occur.

The radiative capture reaction mechanism involves the emission of a γ ray. The $^{17}\text{O}(\alpha, \gamma)^{21}\text{Ne}$ reaction is exothermic, releasing 7.348 MeV. A γ ray of that energy alone will exhibit a significant force on the de-exciting nucleus, possibly deflecting the recoil away from the aperture in the same way that the emission of a neutron might. This is of course not yet a worst-case scenario, as the maximum E_γ is the Q-value plus the centre-of-mass energy. This maximum de-excitation would require a direct to ground state transition, but allows the lowest recoil transmission to be determined from:

$$\theta_{1/2} = \sin^{-1} \frac{E_x}{c \times p_p} \quad (3.31)$$

$$= 0.733 \frac{E_\gamma}{\sqrt{E_{lab} m_p c^2}} \quad (3.32)$$

where the recoil cone half-angle, $\theta_{1/2}$, which can be seen pictorially in Figure 3.4, is a function of the maximum de-excitation, E_γ , the laboratory frame energy, E_{lab} , in keV/u and the projectile mass, m_p , in amu. For the lowest beam energy of $E_{beam} = 200$ keV/u this was found to be ~ 25 mrad, outside of the acceptance of DRAGON. To account for these transmission losses, Monte-Carlo simulations were performed which will be discussed in Chapter 5.

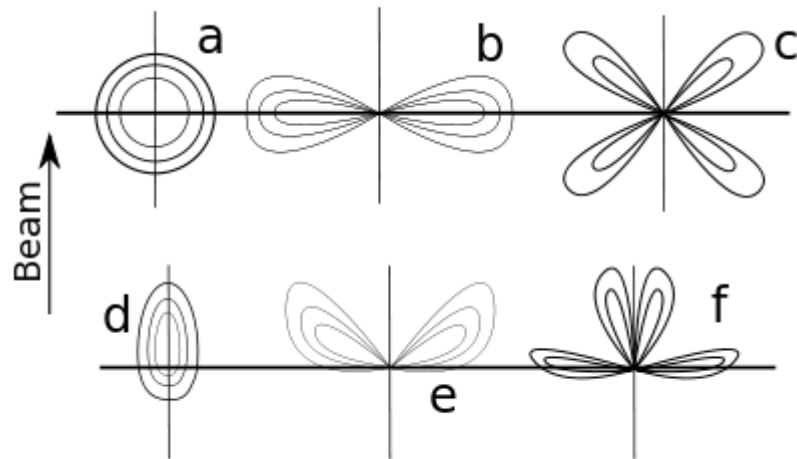


Figure 3.5: Angular distributions in the centre-of-mass frame: (a) isotropic, (b) dipole and (c) quadrupole, and the laboratory reference frame: (d) isotropic, (e) dipole and (f) quadrupole. The direction of the incident beam is vertically along the page.

3.4.3 Angular Distributions

The radiative capture γ ray can be emitted in any direction, but the probability of any particular heading is determined by the angular distribution of the reaction. Knowledge of this reaction parameter can greatly aid the experimental process, especially by increasing experimental yield at minimal increased monetary cost. If it is known that a particular direction is unfavourable then there is no need to waste expensive detectors in covering that angular region. A selection of distributions are shown in Figure 3.5 for comparison.

The most basic distribution is the uniform or isotropic distribution. Here, all angles of emission have equal probability, and yield would indeed be increased as coverage approaches 4π . In addition to the isotropic, there are also dipole and quadrupole distributions represented in the upper portion of Figure 3.5, labelled “a”, “b” and “c”. In these cases, there are strongly favoured regions of intensity where the probability of γ emission is higher. With these distributions the yield would not be improved simply by arbitrarily including additional coverage, a few accurately positioned detectors would provide just as complete a picture. Of course, for that to be practical, it is therefore crucial to know which of these distributions one is investigating.

The distributions presented thus far have only considered the centre-of-mass reference frame, that of the reaction, what the nuclei will experience within the star. However, it has already been established that DRAGON is not in the centre-of-mass frame and the

use of inverse kinematics greatly affects the trajectory of the recoil nucleus. Once the distributions have been transformed into the appropriate laboratory reference frame, as depicted in the lower portion of Figure 3.5, labelled “d”, “e” and “f”, they take on a very different, more forward-focussed shape.

3.5 Helium Burning in Massive Stars

The key properties of a star are its mass and its temperature. The two are intrinsically linked, with massive stars requiring more energy to oppose gravitational collapse; consequently they burn hotter, live shorter lives (“only” 100 million years for a $10M_{\odot}$ star [6]) and most crucially in the context of this work, they activate higher nucleosynthesis stages. For the type of star discussed in Chapter 2, massive, rotating and of low metallicity, the effective burning temperature for the $^{17}\text{O}(\alpha,\gamma)^{21}\text{Ne}$ reaction was found to be $200 < T_6 < 300$ [54] ($0.297 < E_G < 0.646$ MeV) which is in accordance with standard helium ignition conditions of $\sim 0.1T_9$ [6, 14, 46] and the effect of rotation on massive stars [22]. Using the previously established formulae, the Gamow peak for the given temperature range is found via Equation 3.16, displayed on Figure 3.6 and in Table 3.3.

T_6	E_G (MeV)	$E_G - \frac{\Delta}{2}$	$E_G + \frac{\Delta}{2}$
200	0.392	0.297	0.487
300	0.514	0.381	0.646

Table 3.3: Calculated energies in the centre-of-mass frame corresponding to Gamow peaks, upper and lower window boundaries for the effective burning temperature range of the $^{17}\text{O}(\alpha,\gamma)^{21}\text{Ne}$ reaction in massive stars at low metallicity.

The recoil of the $^{17}\text{O}(\alpha,\gamma)$ reaction and compound nucleus for $^{17}\text{O}(\alpha,n)$ is ^{21}Ne . The level scheme [55] for this vitally important nucleus is displayed in Figure 3.6 with the excitation energies, spin and parity, J^{π} , and widths, $T_{1/2}$, for each state shown (where data is available). The Gamow window, ΔE_G , is also displayed and it is clear that there lie 6 states in the nucleus that could contribute to resonant burning within this energy range. However, the lack of structure knowledge in this region makes determining whether a state will contribute difficult to ascertain. Of particular interest would be the J^{π} information, as certainly one factor that determines the strength of any resonance is the relative angular momenta, a property that directly effects the barrier penetrability. Likewise, without also having clear knowledge of the widths from detailed nuclear structure information, one cannot determine the interference between the wave functions of the compound nucleus and those of the entrance/exit channels [56], but this is the subject of far more specialist

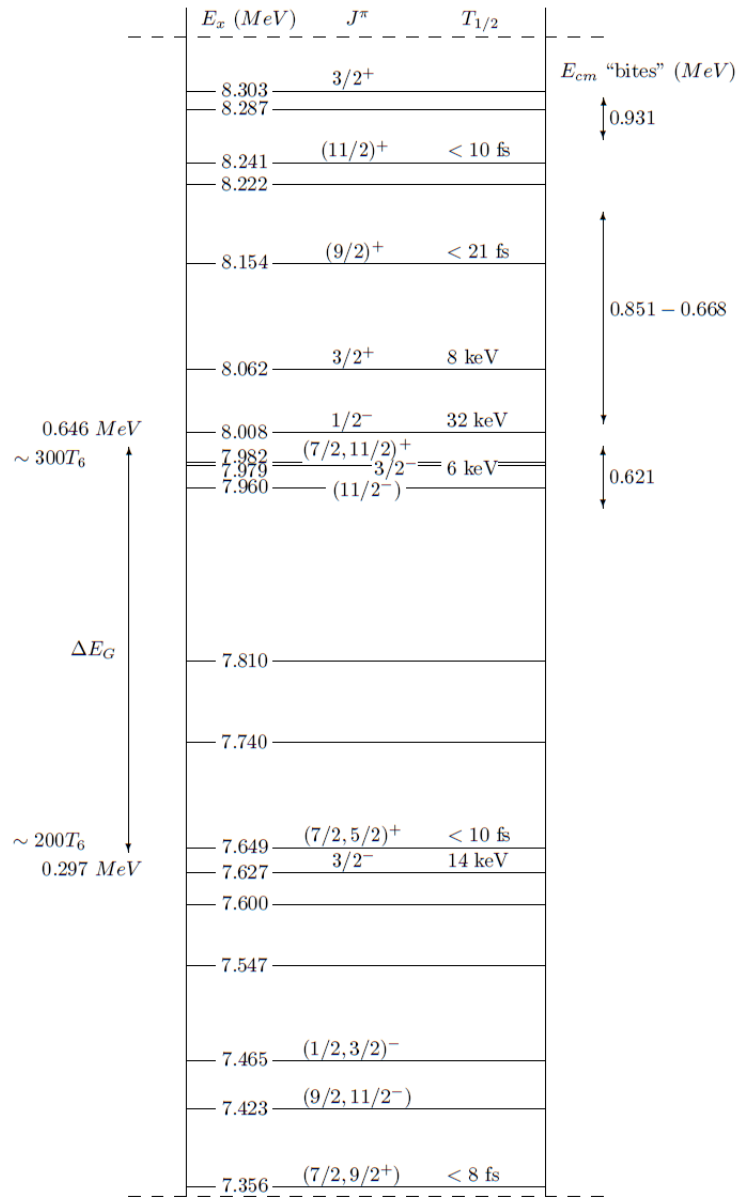


Figure 3.6: Level scheme for the compound ^{21}Ne nucleus [30]. State information in the form of excitation energies in MeV, the spins and parities, and widths, where known, are shown. On the right-hand side the regions of the excitation function investigated by DRAGON are displayed as the centre-of-mass energy “bites” (explained later in Section 5.4.1) which can be compared to the run plan in Figure 4.20. Finally, on the left-hand side of the level scheme the Gamow window for the temperature range $200 < T_6 < 300$ is labelled ΔE_G .

texts.

To close the Chapter it seems necessary to reiterate one crucial point, the astrophysical energy regime of interest. As shown in Figure 3.6 and stated in Table 3.3 the upper boundary of the Gamow window occurs at $300 T_6$, which corresponds to $E_{cm} = 0.646$ MeV. This upper edge of the Gamow window in turn corresponds to an excitation energy in the ^{21}Ne compound nucleus of $E_x = 7.994$ MeV.

Chapter 4

Experimental Setup

“Me Grimlock not bozo, Me Grimlock King.”

- Grimlock

4.1 The ISAC facility

TRIUMF’s Isotope Separator and ACcelerator facility was constructed to deliver radioactive beams for experiments, at energies up to 1.8 MeV/u [57, 58]. The later addition of the ISAC-II facility enables further acceleration to deliver beams of up to 6.5 MeV/u [59]. This additional acceleration was not used for this work due to DRAGON being permanently located in the ISAC-I hall, although other TRIUMF-based experiments, namely TACTIC and TUDA, are somewhat portable and have been moved between halls depending on the campaign energy requirements.

4.1.1 Isotope Separation On-Line

ISAC’s primary purpose is as a Radioactive Ion Beam (RIB) facility, so it seems appropriate that some discussion should be devoted to the production mechanism. Despite this work requiring stable accelerated beam a brief overview of the ISAC RIB will be given here. The facility can produce substantial beam intensities of isotopes in the mass range $8 \leq A \leq 160$ via the Isotope Separation On-Line (ISOL) method. However, due to reasons that will be discussed in a later section acceleration is limited to isotopes with a mass-to-charge (A/Q) ratio less than 30.

The ISOL technique occurs in two major stages: the initial production of the isotope of interest, followed by the extraction and acceleration of that isotope. The production of the radioactive nuclei is due to the main proton beam being directed onto a target. The

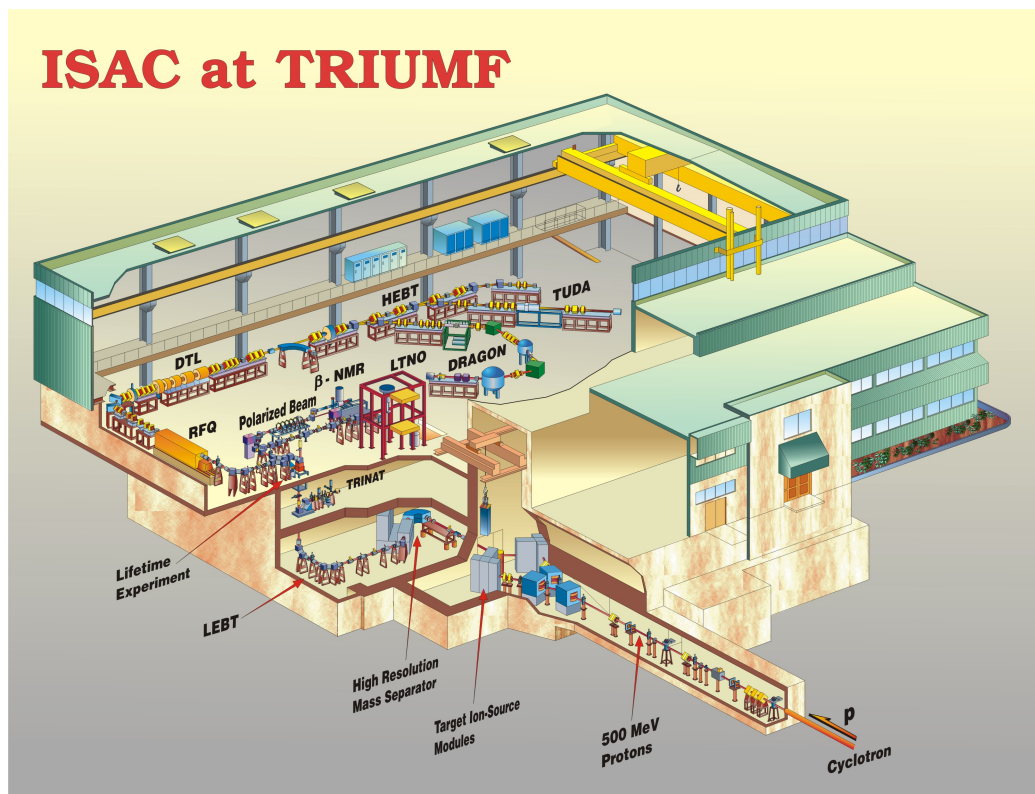


Figure 4.1: The ISAC-I experimental hall

proton beam, produced by TRIUMF's cyclotron at energies of $\sim 500\text{MeV}$ and currents of up to $100\mu\text{A}$ [59], collides with a thick, heated target to produce a range of spallation products that will form the beam.

At this point the spallation reaction products must be extracted and separated to select the nuclide of interest. Thermal diffusion is the method used to extract ions, and is often the bottle-neck for achieving sufficiently high yields for nuclear astrophysics experiments where low cross sections are an issue. The extracted ions are delivered to the ion source where they are ionised and continuously extracted into the separation stage. The drift velocity can be somewhat altered through heating of the ion source itself [60], it being one of the most significant limiting factors to beam intensity. Finally, a high resolution mass spectrometer [61] provides separation by A/Q for the desired species before being delivered to the experiment or injected into the accelerator.

4.1.2 Off-Line Ion Source

The beam used for the entire experimental campaign was produced using the off-line ion source (OLIS). The OLIS terminal houses three ion sources: a microwave source; a surface ion source, both restricted to delivering ions only in the lowest charge states, 1^+ and 2^+ ; and a newer multi-charge ion source, the supernanogan. The terminals are separated by an electrostatic switch which allows for ease of transition without a mechanical intervention being necessary [62] thereby permitting a rapid turnover period. The OLIS system, with two of the three terminals in use, is shown in Figure 4.2.

The microwave source comprises a 10cm quartz-lined cylinder with water-cooled SmCo_5 bars to confine the plasma and a second vacuum chamber of 15cm in length. The plasma is created via injection of a source gas before the 2.45GHz microwave power source is introduced axially between two of the back plate magnetic SmCo_5 bars. The source gas initially comprises neutral atoms as well as charge carrying free ions and electrons. As the microwave discharge is applied the free electrons are excited, experiencing an increase in kinetic energy. These excited electrons will undergo collisions with neutral atoms, possibly freeing further electrons, creating both the desired ion and increasing the electron density of the plasma, an important condition for high currents [64].

The surface ion source makes use of three separate ovens of differing temperature ranges (25-600, 600-1200 and 1200-2000 °C) within an ionising chamber. The ionising chamber is a tantalum tube of 5mm diameter and 5cm in length, heated by a tungsten filament. Surface ion sources, being a relatively simple technology, comprise of a heating element with which the neutral atoms are brought into contact. The technique is used for

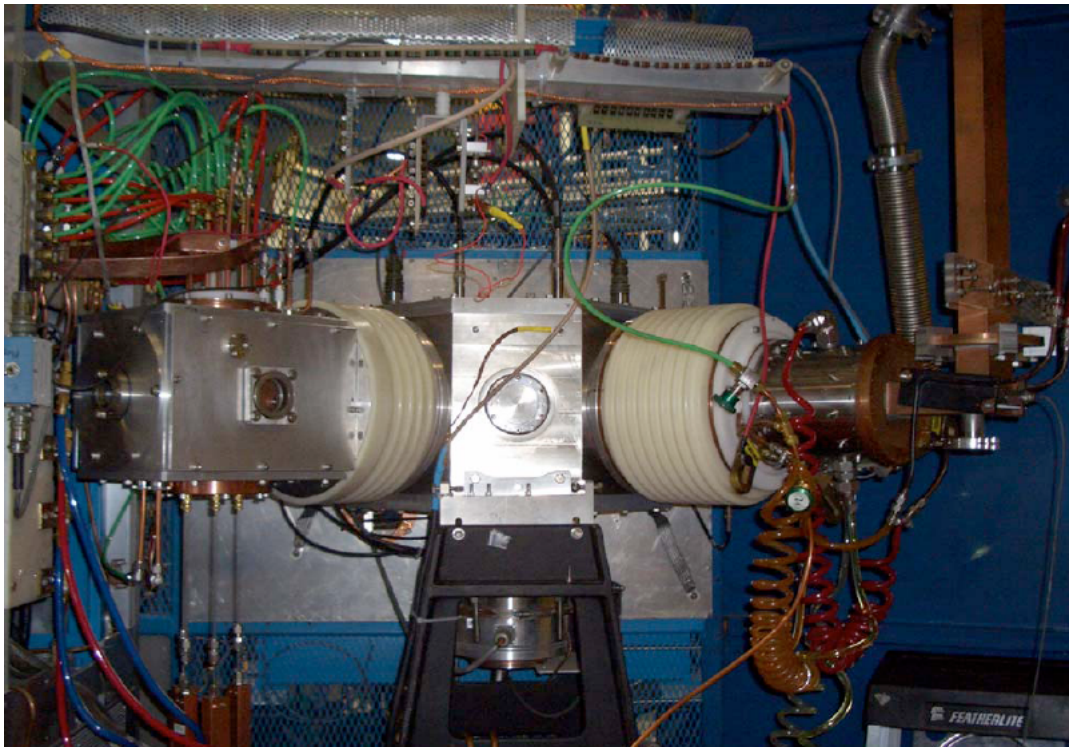


Figure 4.2: The two single charge state OLIS terminals, the surface and microwave sources visible on the left and right terminals respectively. The centre port is for the addition of the multi-charge state Supernanogan ECR ion source [63].

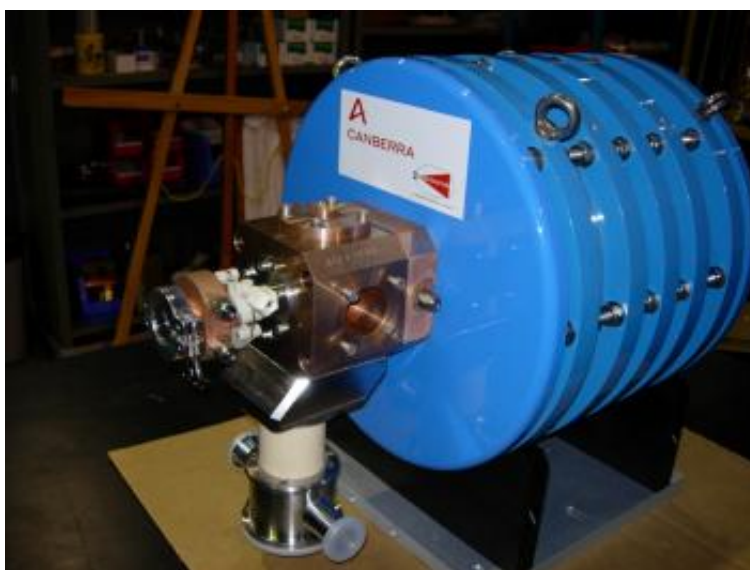


Figure 4.3: The third OLIS terminal, an electron cyclotron resonance multi-charge ion source, the Supernanogan. This terminal provided the beams used in the experimental portion of this thesis.

metals with a low ionising potential, such as the alkali and rare earths.

However, the OLIS station of most relevance for this work is the supernanogan, multi-charge source, which is depicted in Figure 4.3. The supernanogan is an Electron Cyclotron Resonance (ECR) ion source using permanent magnets to produce both the radial and longitudinal magnetic fields. The application of microwaves (200W to 500W at 14.5 GHz) increases the kinetic energy of free electrons within the source gas. Collisions between these accelerated free electrons and the gas molecules of the desired isotope (in this case enriched oxygen) cause the sought-after ionisation. The basic principles behind the operation of an ECR source being that multicharged ions are created by step-by-step ionisation [64].

The advantage over the microwave and surface ion sources is that the containment time is sufficient for multiple collisions to occur on a single molecule thereby allowing the production of multicharged ions [65]. Furthermore, the supernanogan has even been labelled with the “green” moniker, as typically an ECR ion source will require less power to operate.

The acceleration of incident beam particles is performed by the RFQ and Drift-Tube Linac (DTL). The secondary accelerator, DTL, requires a maximum mass-to-charge ratio of approximately 6 so beams delivered in the 1^+ state are subject to passing a stripping

foil to reach the desired A/Q value. The stripping process will produce a range of charge-states, only one of which can be transmitted through the accelerator, and obviously, will also attenuate the beam to a certain degree. The combination of these will have the effect of lowering the maximum beam intensity; in fact, the addition of the supernanogan station resulted in a factor of 10 increase due to the removal of the stripping stage [66].

4.1.3 Linear Accelerator

Once the ions of interest have been produced within OLIS they need to be delivered to DRAGON (or other experimental station, depending on the experiment to receive beam) at the appropriate energy. The ions are extracted from OLIS through the application of electric fields and accelerated up to 2 keV/u. Masses are separated out by magnets, although in this case a high-purity [67] sample of ^{17}O was used so contamination was minimal. The magnetic field is set such that only the desired species passes through the slits to enter the Radio Frequency Quadrupole (RFQ). The technique used is the same as that within the DRAGON separator and so will be thoroughly discussed in Section 4.2.1.1.

The full post-acceleration stages are depicted in Figures 4.1 and 4.4, showing the whole experimental hall, and schematic from source to transport line respectively.

The RFQ is a simple accelerator designed to accelerate beam up to 0.15 MeV/u. The RFQ bunches, focuses and accelerates beam particles purely through the use of RF fields [69]. Its efficiency at low-energy acceleration makes it ideally suited for the energy regions of interest to nuclear astrophysics experiments, with typical Gamow windows being of the order of hundreds of keV for stellar burning scenarios.

After the primary acceleration of the RFQ, the beam enters the Medium Energy Beam Transport (MEBT) section at an energy of 150 keV/u where it is further bunched to maintain a low energy spread. Prior to installation of the supernanogan the beam was required to pass through a carbon foil ($\sim 40\mu\text{g cm}^{-2}$) to strip electrons in order to produce the required charge state for the next acceleration stage. The Drift Tube Linac (DTL) requires $3 \leq A/q \leq 6$ so unstripped beam from the single ion sources would not be acceptable.

Acceleration by the DTL is due to an oscillating field of 106MHz. The principle of operation is similar to that behind the RFQ, that the beam particles are subjected to an AC voltage. However, as the beam is accelerated by one electrode and then passes into the field of the next, opposite polarity region, it would then be decelerated due to the reverse in the field. To overcome this problem the DTL is in fact a series of hollow tubular electrodes through which the beam travels. As it passes through the electrode it

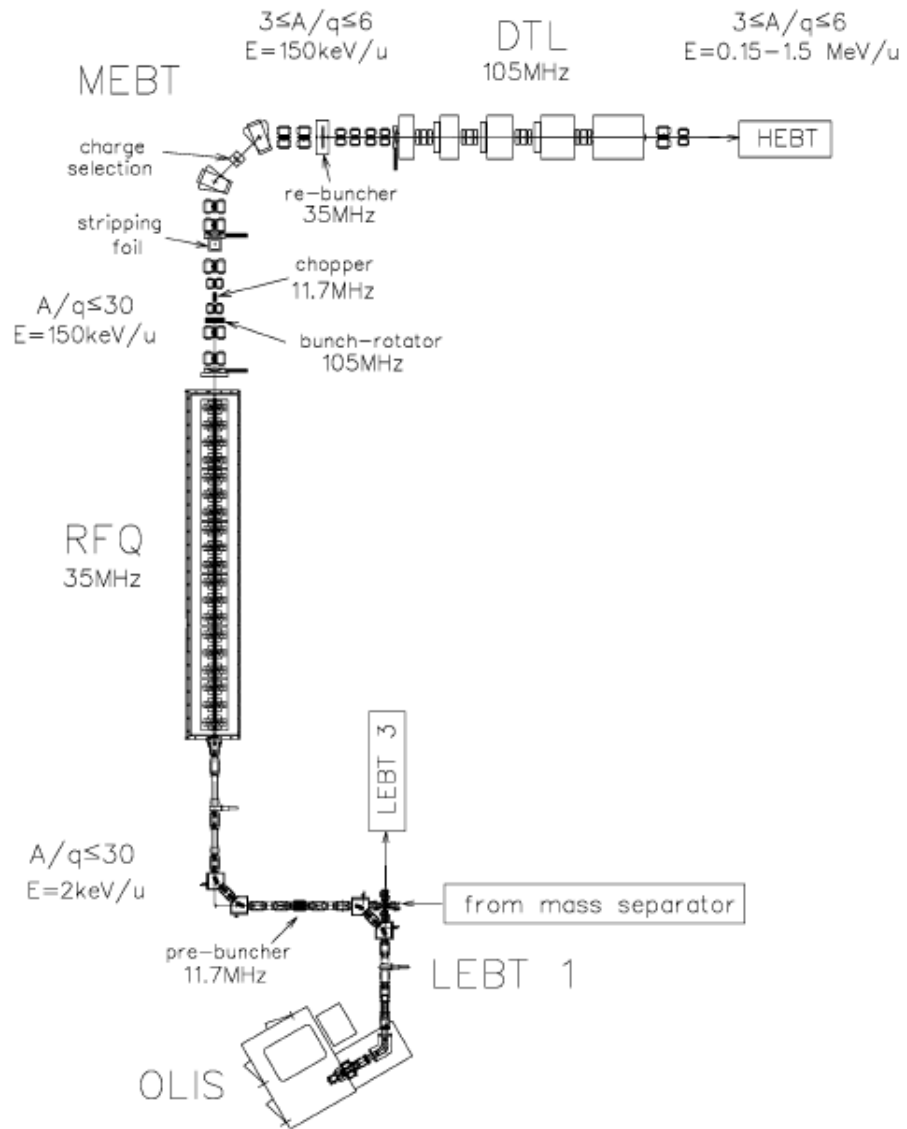


Figure 4.4: The ISAC-1 linear accelerator [68]; see text for details.

enters a field-free region, through which no acceleration is experienced and instead the beam particles simply drift through the section, the Drift-Tube of the name. The DTL is engineered so that the beam particles remain within the shielded section during the period of decelerating voltage, before emerging from the drift-tube to experience the next acceleration phase. For a fixed voltage, each successive electrode will need to be longer than the previous section due to the increase in beam energy and therefore velocity.

Finally, on emerging from the DTL, the beam enters the High Energy Beam Transport (HEBT) section from which it is delivered to the experiment. The whole ISAC-I acceleration stage allows beam energies of $0.15 \leq E_{lab} \leq 1.8$ MeV/u; higher energies are available via the ISAC-II hall, but not for use with the DRAGON facility.

4.1.3.1 Beam Tuning

Once the beam has been produced it needs to be delivered to DRAGON itself at the desired energies. Several experiments are located in ISAC, so the beamline consists of various switching magnets and separators as well as acceleration tanks. The nature of the tuning process causes the beam to diverge at each stage, magnetic quadrupoles are required to refocus the beam. As the entrance (and exit) apertures of the DRAGON target are of finite size, it is of crucial importance that the “beam spot”, the apparent cross-sectional area of the beam of incident ions, is as small and tightly confined as possible. This is monitored by a CCD camera mounted on the straight-on line after the first magnetic dipole and focussed onto the gas target which can be seen in Figure 4.5.

4.2 DRAGON - Detector of Recoils And Gammas Of Nuclear reactions

DRAGON is designed specifically to perform radiative capture experiments for the investigation of nuclear astrophysics questions. The facility comprises of four key features: the recoil mass separator; the windowless gas target; the γ -ray array; and the heavy-ion detector system, all of which can be seen in Figure 4.6 and will be discussed in detail in this section.

4.2.1 Separator

The most substantial portion of DRAGON, certainly in terms of physical dimensions, is the ElectroMagnetic Separator. The DRAGON EMS comprises of 10 magnetic quadrupoles,

4. Experimental Setup

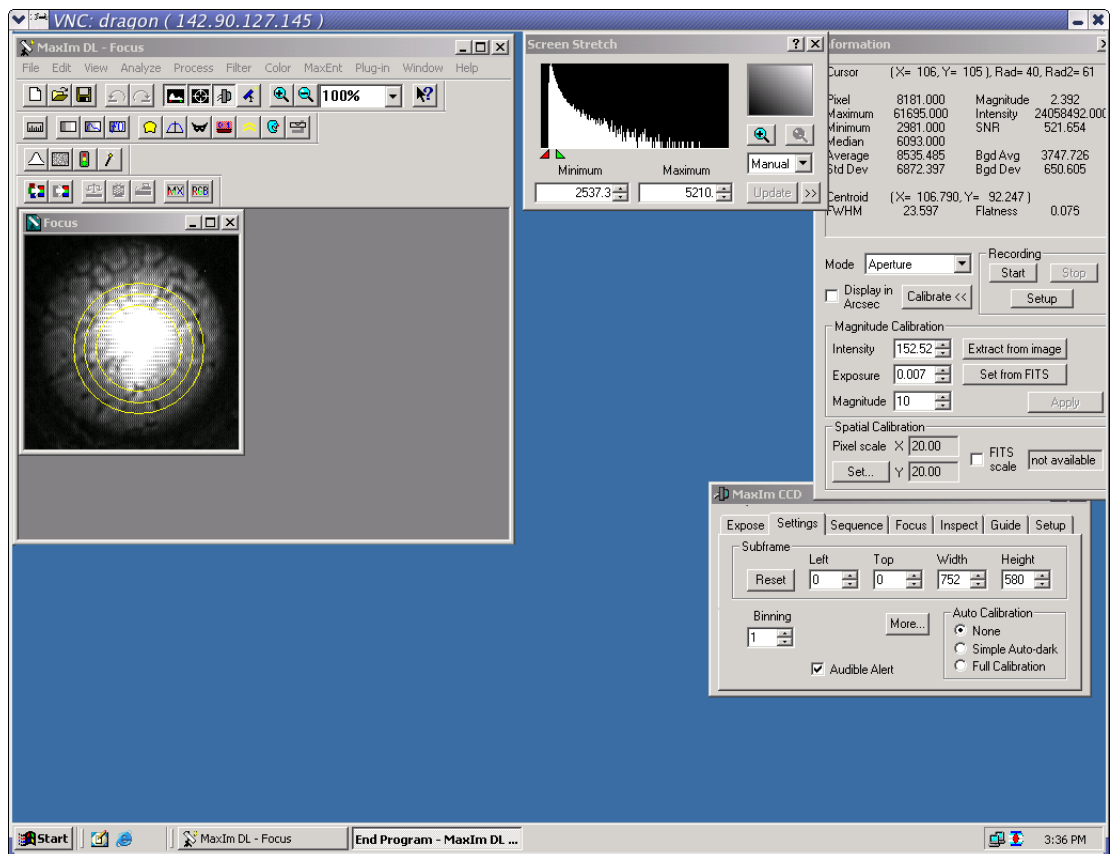


Figure 4.5: Example of the CCD camera “beam spot”. The large spread of glare outside of the first of the concentric yellow circles indicates saturation in this case.

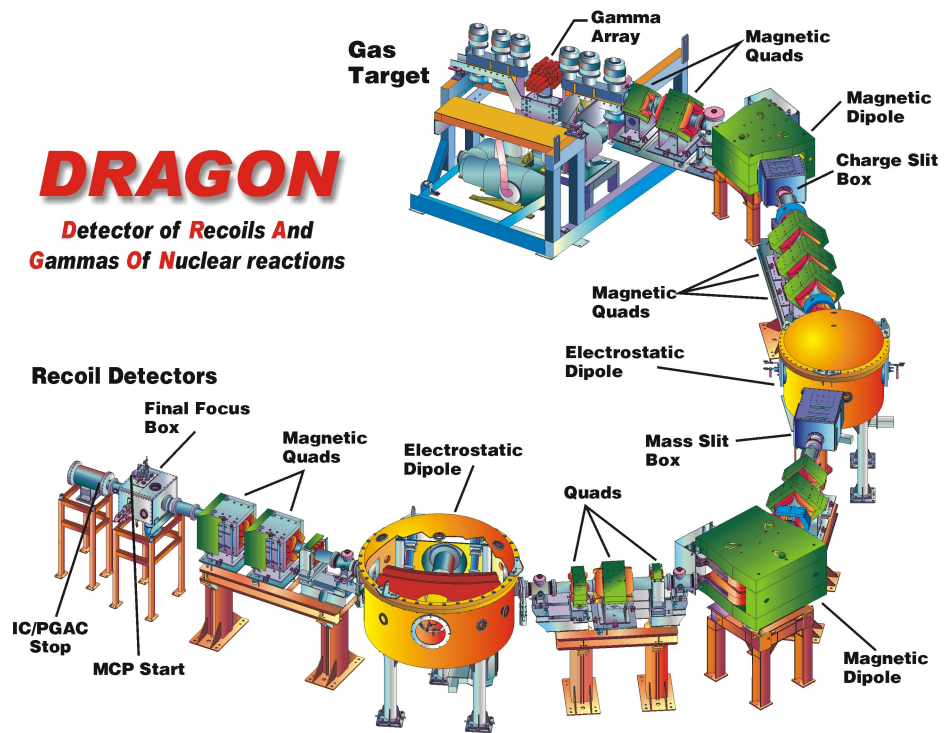


Figure 4.6: A representation of the DRAGON facility.

4 magnetic sextupoles and 2 electric (ED) and 2 magnetic (MD) dipoles. Within the separator there are also various beam-monitoring devices, namely the slits and Faraday cups, that allow for the beam to be tuned through DRAGON to the focal-plane of the separator. These devices are separate to the previously mentioned CCD camera mounted on MD1 in that they are only used in the tuning stages before being retracted so as not to hinder full transmission through the separator. Conversely the CCD camera can be used to monitor the beam in real time for any deviation, but only when there is gas in the target. The entirety of DRAGON, the EMS, the diagnostics, the vacuum etc. can be monitored and controlled remotely with the Experimental Physics and Industrial Control System (EPICS), details of which can be found in reference [70].

The reaction products, as well as the substantially more intense beam, leave the target with the same momenta, therefore the recoil mass separator is required in order to discriminate between the species of interest and those that make up the background. The low yields and cross sections inherent in low-energy nuclear astrophysics measurements necessitate the use of a complicated recoil mass separator. To briefly summarise the method of separation, the first stage, a magnetic dipole, is used to select a single charge-state of the recoil ions, before the first electric dipole provides separation of beam and recoil particles based on their slight difference in kinetic energy [71]. Despite the ED1 separation being due to kinetic energy, conventionally it is described as a mass separator due to the combination of magnetic and electric dipole separation mechanisms. The beam delivered to the second separation stage has been pre-selected based on the charge-to-mass ratio, which allows ED1 to further discriminate the beam by selecting the kinetic energy that matches the desired nuclide mass. This is more fully explained in the subsequent sections. Some of DRAGON’s key specifications are shown in Table 4.1, further details can be found in [71, 72].

Characteristic	
Optical Path Length	20.4 m
Angular acceptance	± 20 mrad
Maximum MD1 Field	5.9 kG
Mass Resolution ($M/\delta M$)	600
Velocity Acceptance	± 2 %

Table 4.1: A few key features of the DRAGON system. The angular acceptance, MD1 field and mass resolution are widely known, having been published in previous papers and theses [71, 72].

4.2.1.1 E/M dipoles: How recoil separation is produced

The DRAGON separation mechanism relies on successive stages of electrostatic and magnetic dipoles, shown in Figures 4.6 and 4.7. By considering the separation stages individually it is possible to show how each component contributes to the overall separation of nuclei. The electrostatic stages separate nuclei based on their kinetic energy to charge ratio (E/q) whilst the magnetic dipoles will operate as a function of momentum and charge (p/q) which can be determined by equating the relevant forces.

First consider the force for the circular motion of the separator bending section, the force due to a magnetic field and then due to an electric field. The familiar formulae give:

$$F = \frac{mv^2}{r} \quad (4.1)$$

$$\vec{F} = q_0 \vec{v} \times \vec{B} \quad (4.2)$$

$$\vec{F} = q_0 \vec{E} \quad (4.3)$$

where the terms have their usual definitions of F (and \vec{F}) the respective forces; m , the particle mass; v , the velocity of the particle; r , the radius of curvature of the bending section of the separator; q_0 , the charge of the particle and finally \vec{E} and \vec{B} the electric and magnetic fields. If the electromagnetic forces are then equated to the centripetal, the earlier assertions can be confirmed.

Since both beam and reaction product recoil exit the gas target with similar momenta, by positioning a magnetic dipole in the first separation position,

$$\frac{p}{q} = rB \quad (4.4)$$

shows that only the selection of specific charge states of emerging ions occurs. This also prevents non-selected charge-states striking the electrostatic dipole electrodes. This initial charge-state selection introduces the single biggest yield reduction factor with the most intense charge-state accounting for some 30-50% of the recoils depending on particle energy. This is thoroughly discussed later in Section 5.2.2.

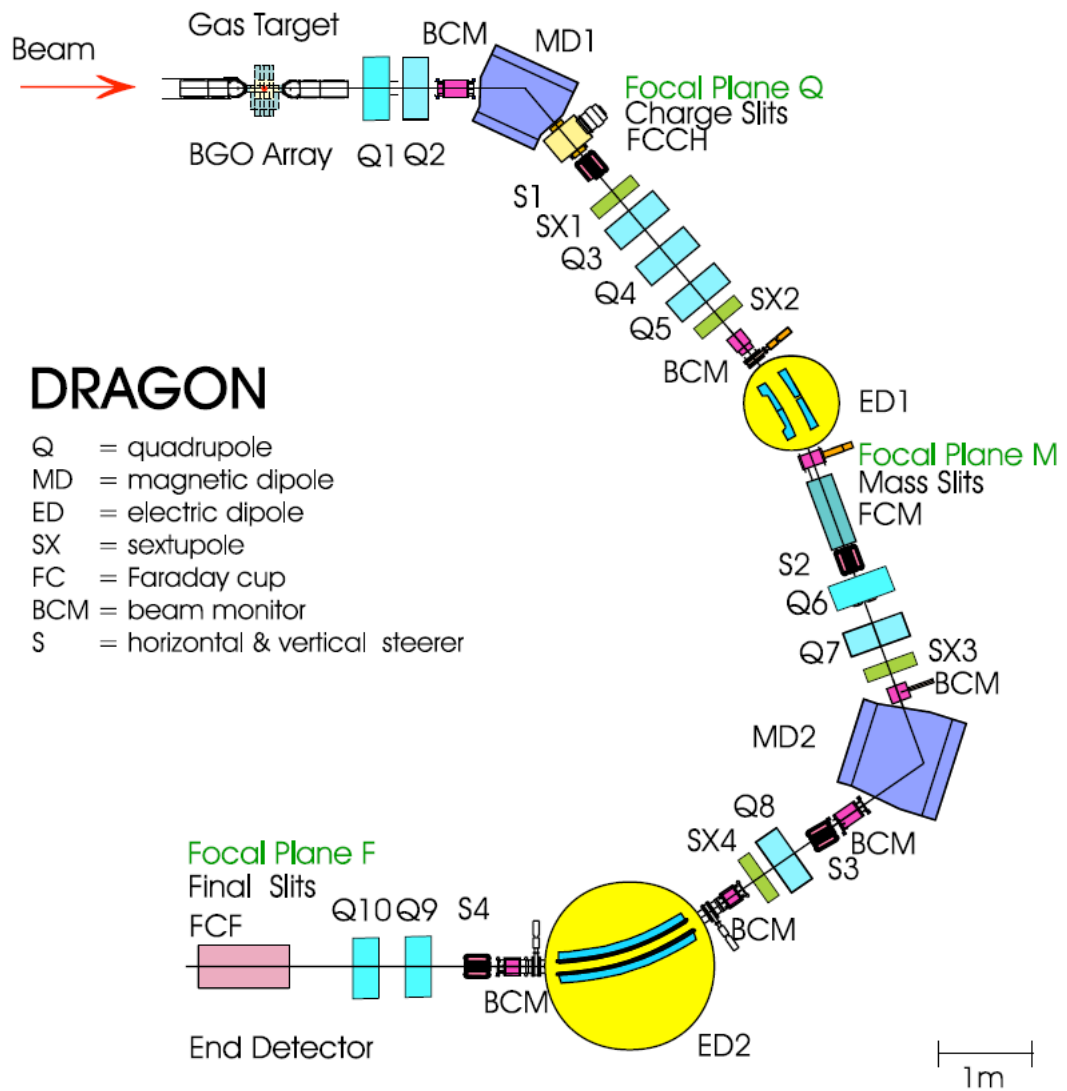


Figure 4.7: Schematic of the DRAGON recoil separator [53].

Due to the similarity in momenta, the MD stage alone is insufficient to completely separate out the recoils from the beam nuclei. Applying the same treatment as before, only now equating Equations 4.1 and 4.3, it is clear that:

$$\frac{pv}{q} = rE \quad (4.5)$$

describes the second separation stage. However, since the beam/recoil are of a single charge state, under the influence of a defined electric field, with near-identical momenta, then Equation 4.5 can be rewritten as:

$$mr = \frac{pmv}{qE} \quad (4.6)$$

which is rearranged into:

$$r = \frac{p^2}{mqE} \quad (4.7)$$

establishing the ED mass separation.

Finally one can determine that the separator as a whole, will therefore act as a mass-to-charge filter.

4.2.1.2 “Leaky” Beam and Suppression Factors

The use of a recoil separator might suggest that the job is done, the laws of physics are in place, and the operator has chosen their magnetic and electric fields so that only the nuclei of interest is selected, experimental physics is now nothing more than an operation of arithmetic. If only that were true.

q ⁺	¹⁷ O	²⁰ Ne	²¹ Ne
3	5.666	6.667	7.000
4	4.250	5.000	5.248
5	3.400	4.000	4.199
6	2.833	3.333	3.499

Table 4.2: Mass-to-charge ratios for isotopes, and charge-states, q⁺, encountered in the present work. Note the proximity of certain ratios, for example ²¹Ne⁵⁺: (20.993843 / 5) and ¹⁷O⁴⁺: (16.999131 / 4).

Experiments are not perfect. The separation relies upon the similarity of the beam and recoil momenta, yet this is a quantity that can change relatively easily through energy losses due to scattering. Table 4.2 contains mass-to-charge ratios, and the proximity of certain ratios to each other highlights the importance of charge-state selection (sometimes the most intense charge-state is not the best choice), as nuclei of differing species but similar A/q might both be accepted by the same separator. Unwanted beam particles that do in fact pass all of the separation stages, resulting in an event at the end detector are termed “leaky” beam. It is the ratio of these leaky beam particles to the total number of nuclei incident on the target which determines the quality of separation, the suppression factor. In DRAGON’s case, a suppression factor greater than 10^{-12} has been observed for coincident events.

During the commissioning of the facility, optical calculations were performed to establish this optimum separation due to EMS configuration. The final design of two successive MD-ED stages was found to require three charge-changing collisions in the gas target before beam particles would be transmitted to the end of the separator [72].

4.2.1.3 Focussing Magnets

Throughout DRAGON both quadrupole and sextupole magnets are made use of to re-focus the ions. The full layout of separation and focussing magnets is depicted in Figure 4.7. Immediately post-target, Q1 and Q2 are required to correct for the resulting recoil cone, whereas the remaining quadrupole magnets return the separated ions to an achromatic focus while the sextupole sections correct any resulting aberration. With the exception of Q2, the magnetic quadrupoles were manufactured with hyperbolic poles to reduce the non-quadrupole component, whereas Q2 had a sextupole component built into its field with a shaping of the pole-tips. The multiple focusing quadrupoles are necessary simply due to the nature of beam optics, and that as it converges in one axis, it must diverge in the perpendicular transverse axis. The successive quadrupoles aim to minimise any divergent spread by alternating the axis to be focussed.

4.2.1.4 Field-Monitoring Devices

The magnetic field produced by both the magnetic dipoles is continuously monitored by Nuclear Magnetic Resonance (NMR) probes to give a precise measurement of the field strength, whilst the quadrupoles are all equipped with Hall probes. The probe attached to the first magnetic dipole (MD1) is also used to provide a beam energy measurement which is given as:

$$\frac{E}{A} = \kappa \left(\frac{qB}{A} \right)^2 \quad (4.8)$$

which relates the beam energy, E , of a nucleus of mass, A , to the charge state, q , and the magnetic field, B , as measured by MD1. The magnetic constant, κ , has the value of 48230 keV/u/(Tesla/u)². The calibration of MD1 itself was performed by correlating beam energy with target pressure. As the beam energy is varied, the position of the resonance peak will move within the target (a reduction in beam energy corresponding to repositioning the resonance upstream of the target centre). If the target pressure is subsequently also varied to return the resonance to the centre of the gas target, by extrapolating down to a pressure of 0 Torr the MD1 constant and the relationship of Equation 4.8 can be confirmed [53, 72].

4.2.1.5 Faraday Cups

“The most commonly used method for collecting and measuring external beams on low- and medium-energy accelerator facilities is a cup-shaped electrode usually known as a Faraday cup” [73]. Indeed, DRAGON makes use of a series of Faraday cups; pre-target, post-target and post-MD1, for primary beam monitoring.

Essentially the Faraday cup is a metal “catcher”, a hollowed out cylinder attached to an ammeter, an example is shown in Figure 4.8. When exposed to a beam of incident ions, the cup receives a small charge while neutralising the ions. The Faraday cup, being a conductor, can then discharge to the DAQ. Since the current produced is directly proportional to the number of incident ions, this allows for an accurate measure of the number of beam particles. To ensure that the current is indeed proportional to the incident beam, the primary design concern of the Faraday cup is the number of escaping ions as a fraction of those incident on the cup in total. The mechanisms by which escape might occur primarily include backscatter of secondary electrons, compensated by reducing the solid angle of the exit aperture. For beams of a sufficiently high energy, electron shower penetration may also be a concern but this is generally engineered out. A more detailed description of design parameters can be found in [74]. At this juncture it may be worth mentioning that for beams of the highest intensity, a heating effect can become enough of a concern that cup insulation might be compromised, thus introducing leakage currents into our escape conditions. DRAGON is equipped with the capability to incorporate water-cooling into the Faraday cup system, but before this work the beam intensity had not reached sufficient levels for this to be of any concern.

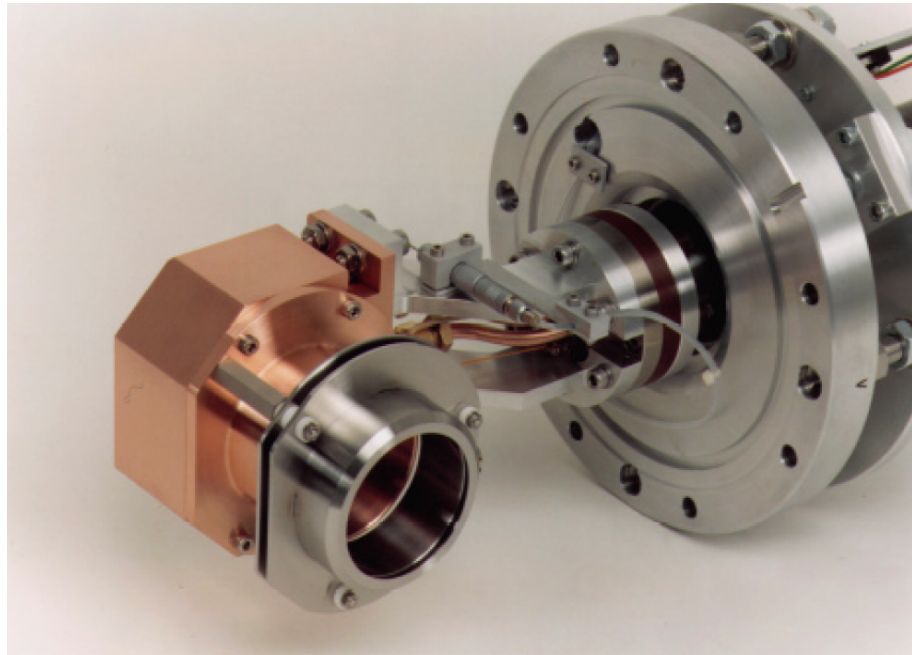


Figure 4.8: Example of a standard Faraday cup [75].

The Faraday cups therefore fill multiple roles. They are required to test and confirm the quality of each individual beam tune, by measuring the transmission through the target (anything less than 95% transmission is scrapped and the tune is restarted) as the ratio of FC1 (post-target) to FC4 (pre-target). Secondly they provide the true beam measurement to which our real-time scattering data can be normalised (discussed in Chapter 5). Finally, the Faraday cup is an extremely effective beam-stop (as can be seen in Figure 5.17) and can be used to protect some of the more sensitive radiation detectors, i.e. a DSSSD, should they be in position during beam tuning.

4.2.1.6 Beam Diagnostics

In addition to the CCD camera and Faraday cups there are further beam-monitoring and diagnostic apparatus. A series of slits are positioned after each separation stage for beam tuning. The slits are two metal plates that can measure incident charge. By monitoring the charge incident either side of the central slit the position of the beam can be determined and so then by altering the magnetic or electric fields of the dipoles the desired species can be selected.

DRAGON also contains Beam Centering and Beam Profile Monitors (BCM and BPM). The Beam Centering Monitor is simply a metal plate divided into quadrants. Analogous to the use of the slits, if the beam is stopped by the BCM plate, four separate currents will

be recorded. A good, central tune will result in equal currents on all four quadrants. In a similar way, the BPM will record a current due to an incident beam, although in this case it is from a wire grid instead of plates. Through the use of a small wire separation, and by comparing the variation of current across the grid, it is possible to view the effective profile of beam-spots with even sub-millimetre diameters.

4.2.2 The Windowless Gas Target

The DRAGON facility makes use of a differentially-pumped windowless gas target. In this way experiments can be performed on relatively pure target materials, i.e. hydrogen or helium gas, rather than suffering from contaminants to be removed in analysis stages by using, say, a CH₂ foil. It also removes problems of energy loss and beam straggling due to the nuclei having to pass through entrance or exit windows. The need for confinement windows to contain the gas is removed through a substantial pumping system to maintain the pressure differential between the exterior beamline and the centre of the target itself. The interior of the target box can be seen in Figures 4.9 and 4.10 (also in 4.12), with the gas intake tube, silicon surface barrier detectors and the target proper, clearly visible. The intake tube feeds the recirculated gas back into the underside of the target which can be controlled via EPICS, as discussed in Section 4.2.1, and the two surface barrier detectors are used to measure elastic scattering of target nuclei in real time, for the purposes of beam normalisation and will be featured in greater detail in Section 5.3.1.

4.2.2.1 Issues with Gas Targets: Beam Straggling, Gas Confinement

The main issue with using a gaseous material as a target is containment. Obviously a gas is free flowing and will dissipate unless housed in some sort of container but access needs to be provided for the incident beam particles, and possibly any recoils emitted in the reaction.

Unlike γ rays, charged particles are not highly penetrating, and certainly would not make it through the steel that beam lines are made from. Some kind of entrance aperture is therefore necessary. However, this creates its own problems as a beam line is generally held at high vacuum in order that heavy ions might be effectively transmitted to the experiment. An opening from the gas target directly into the beam line would result in a rapid loss of target gas, and compromise the integrity of the high vacuum. To maintain gas containment, usually, some form of window is required, one that is sufficiently thin so that it remains transparent to heavy ions, whilst also being structurally sound across the variation in pressure between target and beam line.

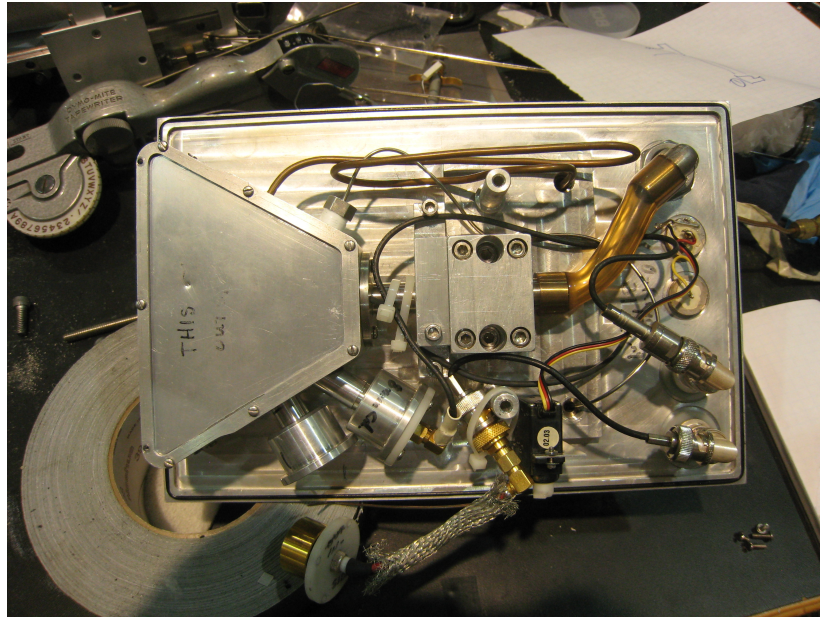


Figure 4.9: The interior of the DRAGON gas target when removed for work on the surface barrier detectors. The target gas is confined within the trapezoidal shape at the left of the picture (The top of the target).

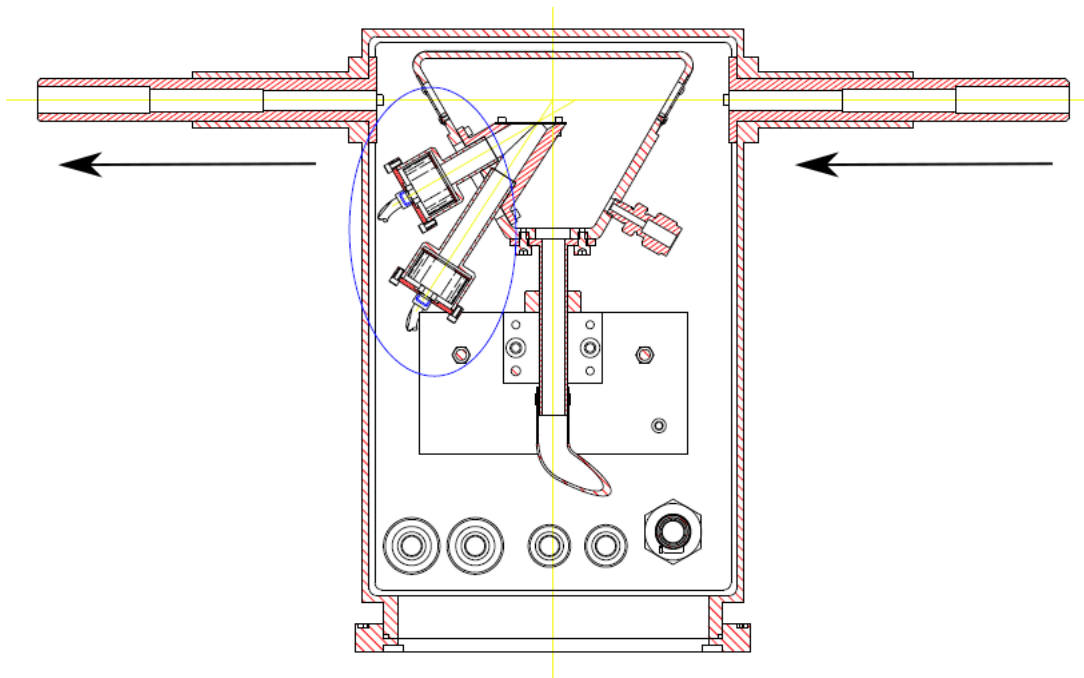


Figure 4.10: A schematic of the windowless gas target. Highlighted by the blue circle are the two surface barrier detectors at 30° and 57° used for beam normalisation with the black arrows indicating the direction of the beam [76].

The TUDA facility [77] makes use of a gas-cell with a $2\mu\text{m}$ thick Ni window but faces frequent problems of the ion stopping in the entrance/exit window. Should all these problems be overcome, and the incident heavy ion reaches the target, a reaction indeed occurs, and then the recoil nucleus passes through the exit window to reach the final detector (or separator in the case of DRAGON), further problems still remain due to the effect of straggling.

As the heavy ion passes through any medium, in this case the entrance/exit window, it will experience the usual associated energy loss and also the resolution of the “beam spot” will reduce, as the beam is spread out in what is known as straggling.

4.2.2.2 Technical Aspects

To achieve its aim the DRAGON target makes use of an intricate system of pumps. The system comprises 8 turbo pumps and 6 Roots blowers (a positive displacement lobe pump) [78] which in combination with the series of apertures allows for an impressive pressure differential of up to 10^7 Torr from the centre of the gas target to “just” outside.

The target gas is continually recirculated throughout the system by the pump arrangement. Any gas leaking from the central target cell must pass a series of apertures before any might reach the beamline proper. The tightest apertures, those of the cell entrance and exit, are machined to the size of 6mm and 8mm respectively. This allows for good transmission of both beam and the increased recoil cone at the lower energies, without compromising gas containment. These apertures are also slanted at an angle of 30° so that exiting jets of gas are directed towards the Roots blowers, thereby removing gas from the bottom of the target box, as opposed to along the beam line itself.

The recirculated gas is extracted from the system and compressed to a pressure of 45 Torr by the Roots blowers. Prior to being returned to the target the gas is first passed through a zeolite cooling trap to purify the recirculating gas and remove any contamination caused by the pumping mechanism, i.e. oil or air. The trap also returns the gas to the nominal operating temperature of 300 K due to internal heat exchange [52].

4.2.2.3 Target Thickness and Profile

To now revisit Figure 4.9, the actual target is the trapezoidal shape to the left (the upper portion of the box) with a physical, geometric length of 11 cm along the axis of the incident beam. However, since one of the conditions for nuclei to interact is not whether they happen to be travelling through an area designated as “the target”, one must consider how sharp a cut-off the pumping system truly provides, and what portion of the gas may

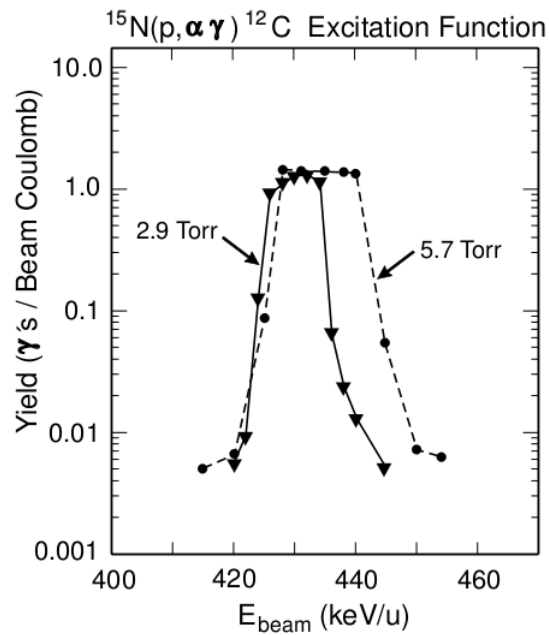


Figure 4.11: The thick-target yield curve of the $^{15}\text{N}(p,\alpha\gamma)^{12}\text{C}$ reaction as a measure of the target pressure profile [72]. The effective target length is taken as the FWHM of the excitation function.

be outside of the target's boundaries.

Despite the effort of the differential pumping system, some small amount of gas still leaks from the target and into the beamline (both upstream and downstream into DRAGON). During the commissioning stages of DRAGON, measurements were taken to understand features of the target such as the pressure profile and uniformity. By utilising the $^{15}\text{N}(p,\alpha\gamma)^{12}\text{C}$ reaction, specifically a narrow resonance at 420 keV/u, the emission rate of 4.4 MeV secondary γ -rays was obtained with a γ -ray array configured to have uniform efficiency across a 20 cm section of beamline. This covered the 11 cm target cell itself, as well as the wider entrance and exit apertures. The results of these commissioning tests are discussed in [72], but if Figure 4.11 is now examined it is clear that the pressure cut-off is indeed a sharp one. The difference between yield measurements where the beam energy is selected to place the resonance inside and then outside of the target cell is a factor of ~ 300 . It is the width of this excitation function shown in Figure 4.11 from which one can deduce the effective target length that then becomes the important value.

The effective target length was further confirmed with a more accurate method directly measuring the energy lost by 275 keV/u beam of ^{21}Ne ions through the target. This is discussed more fully in [72], but an energy loss of $83 \pm 2 \text{ eV}/10^{15} \text{ atoms/cm}^2$ was found, which equates to an effective target length of $12.3 \pm 0.4 \text{ cm}$.

When “target thickness” is discussed, it is not the length, geometric or effective, that is really of interest, but rather it is in terms of the energy loss which becomes most applicable. Of course, the energy lost as a particle travels through a medium is a function of projectile energy, various material properties and the distance travelled [79], but since almost all variables are kept constant for a given run, it is really only the target pressure that is of concern. The calculations for target number density are discussed later, in Section 5.4 but it is worth giving a brief summary here. For the range of pressures used in this experimental work, $\sim 3 < P < \sim 8$ Torr, the energy loss is determined to be $23 < \Delta E < 56$ keV. These are shown in Table 4.3 and were calculated according to Equation 4.8 for a target with and without gas.

P (Torr)	E_{cm} (MeV)	ΔE_{tab} (keV/u)
3.11	0.825	7.3
4.00	1.170	9.5
5.16	0.818	11.6
6.26	0.814	14.0
8.04	0.621	16.4
8.38	0.695	17.1

Table 4.3: Sample target thicknesses as measured via energy loss through the target gas. The uncertainties are due to the energy measurement and therefore $< 1\%$ [72].

4.2.3 BGO γ -ray array

In Chapter 3 the nature of a radiative capture reaction was defined, that being a reaction where a recoil ion and associated γ ray are produced. In order to detect the γ ray some sort of detector system must be present and optimised for detection of this emission. The system utilised by DRAGON is the array of bismuth germanate (BGO) crystals shown in Figures 4.12 and 4.13.

4.2.3.1 Bismuth Germanate as a Detector Choice

The DRAGON γ -ray array comprises 30 hexagonal prism BGO crystals surrounding the gas target, which we can see in both the photograph of the retracted array in Figure 4.12 and the schematic drawing of Figure 4.13. The primary attribute of BGO for γ -ray detection is its high proton number. In Figure 4.14 it can be seen how the high Z of bismuth (83) accounts for its unusually high detection efficiency. This is especially true in comparison to more traditional detectors in fields such as γ -ray spectroscopy, namely hyper-pure germanium (HPGe). Although highly regarded for its excellent energy resolution

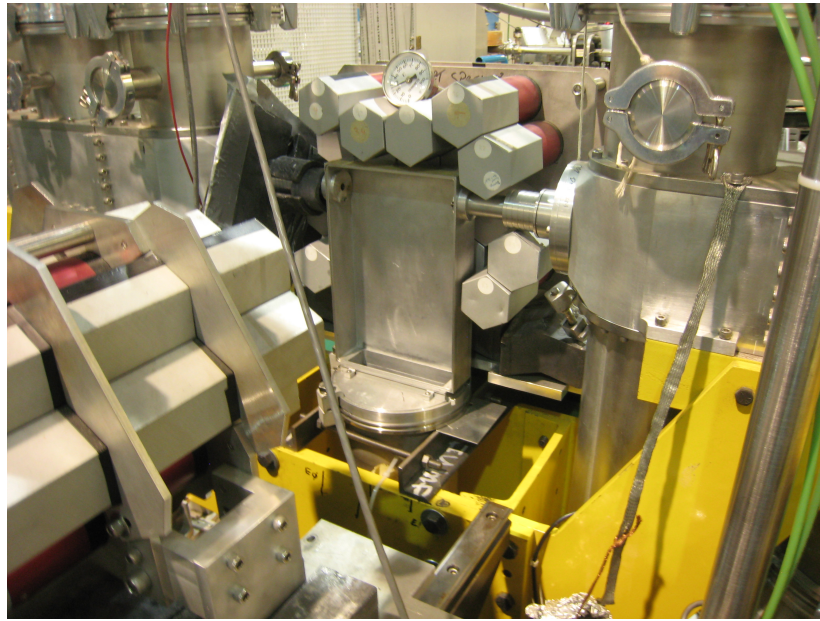


Figure 4.12: The DRAGON BGO array retracted from its standard position surrounding the gas target for maintenance. Visible are the hexagonal BGO crystals, the target containment box, entrance and exit apertures to the beamline and turbo pumps.

($\sim 0.15\%$ for a $1.33\text{ MeV } \gamma$ ray [79]), the intrinsic efficiency of HPGe for an $8\text{ MeV } \gamma$ ray is $\sim 3\%$, which is simply insufficient for DRAGON's needs. Figure 4.15 highlights the general energy dependence of intrinsic efficiencies for a range of common detector materials. It is clear to see how BGO easily outperforms HPGe at higher energies, the latter being severely handicapped by its relatively low atomic number. In addition to the high Z , BGO's density of 7.13 g/cm^3 results in "the largest probability per unit volume of any commonly available scintillation material for the photoelectric absorption of gamma rays" [81].

It is an entirely mundane argument, but cost will always play a role in determining which technology to utilise. Figure 4.14 shows that a single transition γ emission for $^{17}\text{O}(\alpha, \gamma)^{21}\text{Ne}$ of 8 MeV will interact with, say, germanium ($Z = 32$) or bismuth primarily through Compton scattering, thereby requiring a large detection medium to ensure the total energy deposition. Obviously it is substantially more cost-effective to produce a large BGO crystal than HPGe. Furthermore, when scaling up the array to provide as great a solid angle coverage as possible, the additional liquid-nitrogen cooling facilities required place significant logistical constraints in terms of space availability, with that around the target already home to the pumping system necessary to operate without win-

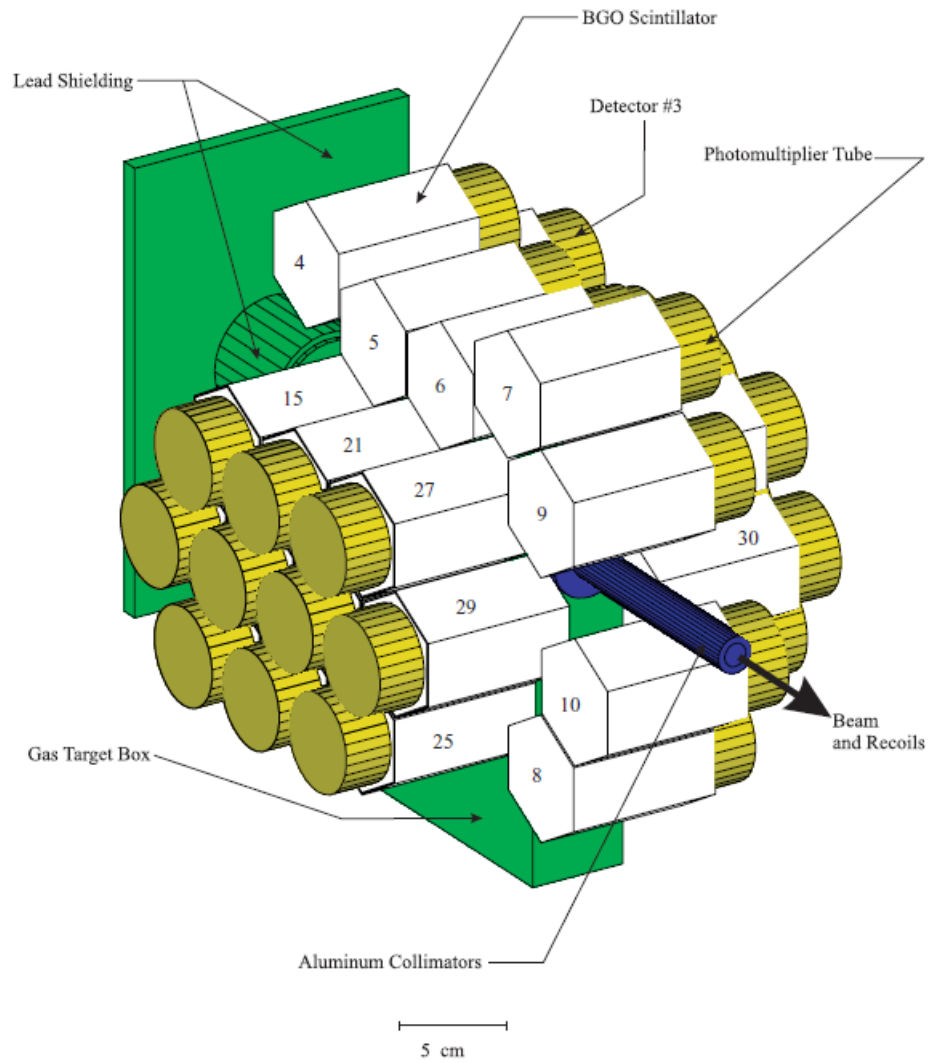


Figure 4.13: Schematic diagram of the DRAGON BGO array produced through the GEANT3 simulation package [80].

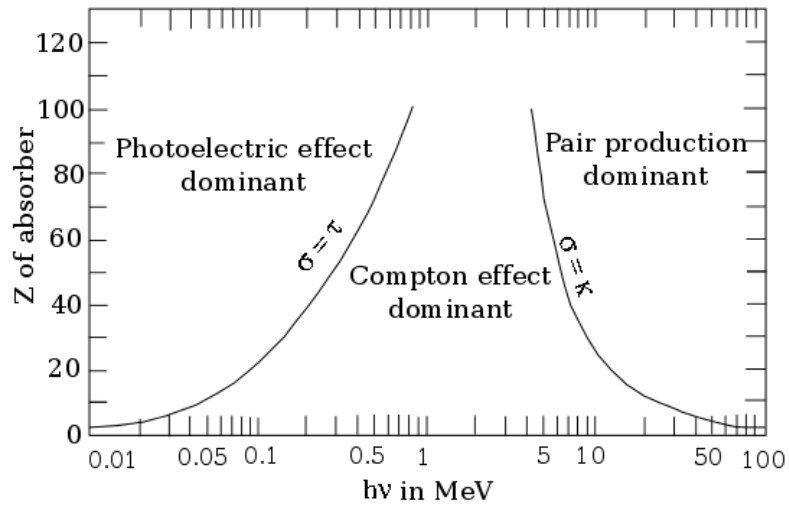


Figure 4.14: Relative importance of the major γ -ray interactions for absorbers of different proton numbers. For instance, a 100 keV γ ray travelling through a material with $Z = 32$ (HPGe) will most likely result in the photoelectric effect (PE), being squarely in the PE effect dominant region. However, should a more energetic γ , say 1 MeV, impinge on the same material, then it is clear that Compton scattering is more likely. The lines highlight the values of Z and $h\nu$ for which neighboring effects are equal (adapted from [82]).

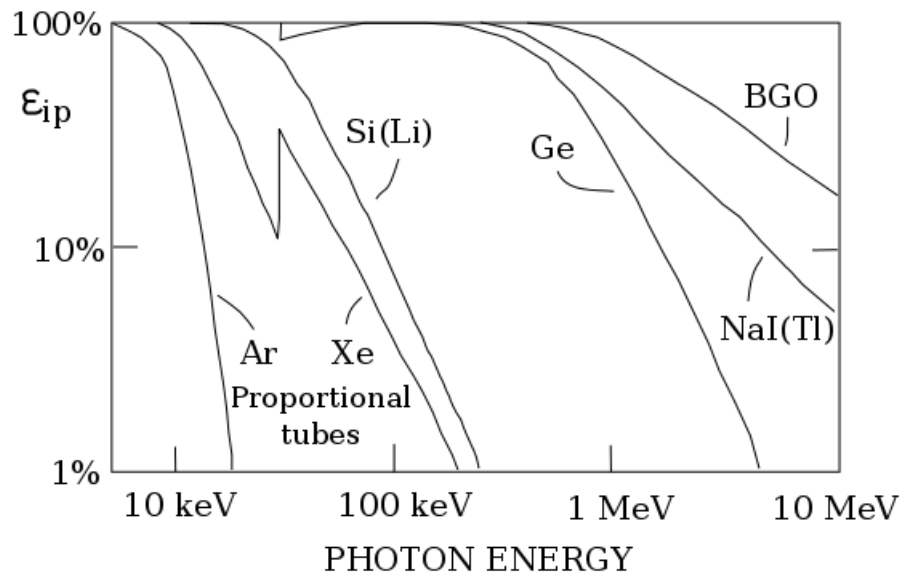


Figure 4.15: A generalisation of the intrinsic full-energy peak efficiency with respect to the energy of the photon incident on some common detector materials (adapted from [81]). Of particular note are the relative efficiencies of BGO and HPGe (labelled Ge) in the energy region of interest for the $^{17}\text{O}(\alpha, \gamma)^{21}\text{Ne}$ DRAGON experiment, namely ~ 8 MeV.

dows. Notwithstanding that the bismuth component allows for transition to the more favourable photoelectric dominant region of Figure 4.14 to occur at higher energies and thus reduce the probability of energy loss via scatter out of the detector.

4.2.3.2 Detector Efficiency and Resolution

It has been the work of a previous study to determine the relevant efficiencies and resolutions of the DRAGON γ -ray array. The work by [80] developed the Geant3 simulation used by this (and all previous) thesis, as well as verifying the results through experimental measurements. It also established the geometric coverage of the array to be ~ 89 - 92% , depending on whether additional lead shielding at the target entrance was required, as is the case for radioactive beam experiments. For the investigation of the $^{17}\text{O}(\alpha, \gamma)^{21}\text{Ne}$ reaction, the higher coverage arrangement was in use.

In the study by [80], simulated efficiencies and resolutions were produced for both a single crystal and the fully implemented BGO γ -ray array. These results were then verified with a variety of γ sources. The energy resolution of the array for the 6.13 MeV γ ray of a $^{244}\text{Cm}/^{13}\text{C}$ source was found to be $\sim 7\%$ FWHM.

The simulation established the efficiency of the entire array to be of the order 45-60% for γ rays of energy 1-10 MeV. The variation is in part due to the adjustable threshold of the DRAGON ADCs.

4.2.4 End Detectors

In order to obtain a coincident event, the detected γ ray requires something for it to be in coincidence with. DRAGON has the capability of using a variety of systems to detect the relevant recoil nucleus, the heavy ions that are directed through the separator. Firstly, there are a pair of micro-channel plates (MCP) which provide a local time-of-flight measurement, before the focal-plane detector. This final section is interchangeable, as DRAGON can make use of either a Double-Sided Silicon Strip Detector (DSSSD) or an Ionisation Chamber (IC). For this work the ionisation chamber was used.

4.2.4.1 Micro-Channel Plates

The penultimate stage of DRAGON is the local time-of-flight (TOF) system. In this case “local” specifically refers to this end-stage recoil detector system in contrast to the full separator TOF which takes one signal (either start or a delayed stop) from the triggering of the BGO γ -ray array.

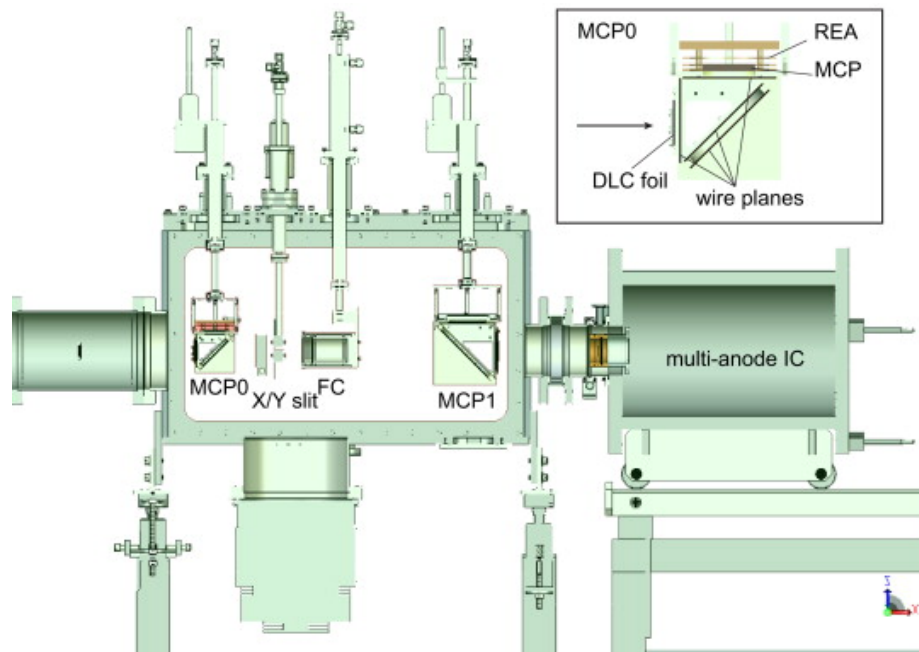


Figure 4.16: The DRAGON local time-of-flight system showing position of the two MCPs in relation to the ionisation chamber end detector [83].

The local TOF system comprises two micro-channel plates, fast transmission detectors, positioned at the extremes of the “MCP box” in order to obtain the greatest distance for TOF particle separation. This flight path is measured to be 59 ± 0.5 cm [83] with MCP0, the smaller of the two, in the upstream portion of the box, and MCP1 positioned just upstream of the ion chamber. This set-up is shown in Figure 4.16.

The charged particle passes through the carbon foil, releasing electrons which are then deflected by the electrostatic mirror onto the MCP. The MCP then multiplies this electron signal, which produces the fast-timing pulse used to determine the local TOF.

The MCP is an array of many millions of microscopic glass capillaries, each of which acts as an electron multiplier. The individual tubes, some $15\text{-}50\mu\text{m}$ in diameter [81] have a semi-conductive surface which allows for emission of secondary electrons once the primary incident electron has struck this surface. A potential is applied along the length of the glass tube which accelerates the electrons towards the exit, producing further electron multiplication as the number of collisions increases.

Positive ions can be created within the MCP capillaries, especially if the vacuum integrity is compromised during routine maintenance or set-up procedures, which then cause feedback problems by being accelerated back out towards the entrance of the plate. To avoid such problems the MCP tubes are often shaped into a chevron pattern which

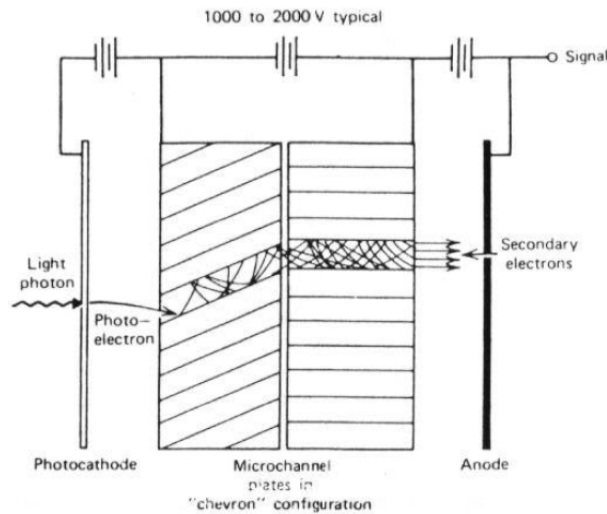


Figure 4.17: Example of a chevron pattern MCP system [81].

causes any positive ions to strike a wall before their energy is sufficient to produce their own secondary electron cascade. The DRAGON MCP system makes use of two stacked plates in an asymmetric chevron formation which can be seen schematically in Figure 4.17.

4.2.4.2 Ionisation Chamber

One of the oldest types of radiation detector, the ionisation chamber has been widely used throughout the course of nuclear physics experiments. The detector simply consists of a conducting container, usually a cylinder, filled with gas, and a window through which particles can enter. There are also a set of anode plates, shown in Figure 4.18, whereby a potential is applied such that the anode attains a positive voltage relative to the cathode.

As a particle travels into the detector, a number of molecules will be ionised, creating both a positive ion and a free electron. Due to the application of the electric field, each member of an ion pair will be accelerated to their respective collector, with the electrons accelerated to the anode and the ions towards the cathode. The total number of ion pairs provide the required energy information of our particle, the amount of charge collected being proportional to the total energy deposited in the detector.

The ionisation chamber is a rugged and cost-efficient means of detecting both charged particles as well as γ rays. The low cost allows detectors of virtually any size (within reason) to be constructed. The stopping power in particular can be tailored to the specific requirements of the experiment at that time by simply altering the pressure of the gas

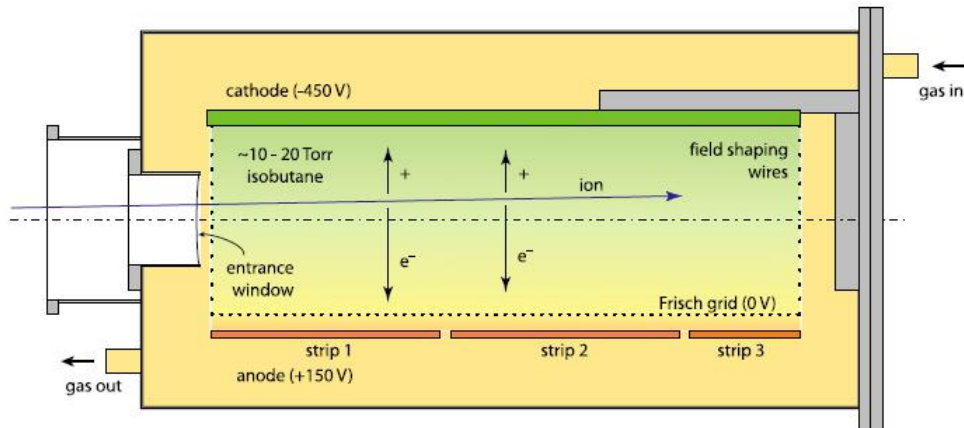


Figure 4.18: Schematic of the original DRAGON Ionisation Chamber. To improve particle identification, the DRAGON IC underwent an upgrade whereby the number of anodes was increased from the 3 depicted to 5 for the study of $^{23}\text{Mg}(p,\gamma)^{24}\text{Al}$ [63, 84]. However, prior to the $^{17}\text{O}(\alpha,\gamma)^{21}\text{Ne}$ experiment the final anode failed, so for this work a slightly improved configuration of 4 anodes was used.

in comparison to, say, a semiconductor, or other solid-state detector medium with a set geometry. In high yield situations, when “leaky” or attenuated beam are impinging on the end detector, a rugged (cheap!) material is highly advantageous. The ionisation chamber is extremely resilient to radiation damage which would otherwise irreparably effect an expensive DSSSD.

The ionisation chamber used in the DRAGON experiment comprised 4 anodes surrounded by isobutane at a nominal pressure of 8 Torr [71, 85] which is separated from the vacuum of the beamline by a mylar window of $130\ \mu\text{g}/\text{cm}^2$. The first two plates, IC0 and IC1, each covered 10cm in the direction of the beam axis. The remaining plates, IC2 and IC3, were slightly smaller at 5cm in length. The use of the multiple anode system allows for energy deposition across a number of separate anodes. Through initial calculations using SRIM [86] the IC pressure was calculated so that the recoil nuclei would stop in the third anode, thereby allowing sufficient stopping power that the total energy should be deposited within the detector whilst maintaining a spread across a number of anodes to allow further particle ID methods.

The nature of the ion chamber is that a relatively large volume is enclosed, there can be problems due to the respective drift times of the electron-ion pair. The heavy ion obviously has a much lower drift velocity than its paired electron, and consequentially the variation in drift time becomes a function of interaction position and ion velocity. For the

case of electron-sensitive ion chambers this effect can be removed through the application of a Frisch grid [81]. This is achieved through the separation of the stopping gas medium into two sections by an electron-transparent grid at an intermediate voltage. Regardless of the location of the interaction within the stopping gas, the heavy ions are attracted to the cathode whilst the electrons move toward the grid/anode. During this phase there is no signal generated by the electron-ion pair. However, once the electron passes through the grid and experiences the further potential difference to the anode, a signal voltage occurs with a much steeper rise than would be the case were the Frisch grid not present.

4.2.5 Ancillary Measurements

In addition to the count of ^{21}Ne recoils, and their associated data (timing, beam normalisations, γ ray events etc.), there are also a number of further measurements that must be performed by DRAGON in order to properly analyse the results of any experiment. Several of these auxiliary experiments have been performed in the past, and need only be confirmed rarely, others remain species, or campaign specific.

Those measurements that do not require repeated readings are the system-based ones, for example the density profile for a particular target gas, as was discussed in Section 4.2.2.3, or the efficiency of the BGO γ -ray array. These have all been the subject of previous theses and articles [52, 72]; little is gained by repeating the material here.

Although substantially more robust than the alternative DSSSD, it is still unwise to unleash the full beam intensity on the ionisation chamber. Likewise, the MCP foils would rapidly cease to be MCP foils should they be directly exposed to beam. Nevertheless, it is often advantageous, if not necessary, to take a direct measurement of beam particles. By measuring the beam directly, it is possible to provide a background reading showing where “leaky beam” particles will appear in analysis histograms. Examples of these plots can be found throughout Chapter 5. Both the DRAGON experiment and ISAC I-II facilities have a range of “pepper pot” attenuators which can stop various portions of the incident beam intensity. This allows for measurements to be taken of the reduced, or “attenuated”, beam.

It has already been mentioned in Section 4.2.1.1 (and should be intuitive) how DRAGON can only be tuned to a single charge state at any time, and in Section 4.2.1.2 that as a beam travels through the target gas charge-changing collisions will occur. If this is then coupled with the knowledge that nuclear reactions will produce recoils in a range of charge states themselves, it is clear that some fraction far less than 100% will be selected by the separator. In order to accurately determine the cross section of the reaction it is essential

that the proportion of recoils existing in each charge state, the charge-state distribution, is known.

The measurement of the charge-state distribution is performed separately to the main experiment, using a beam of ^{21}Ne produced through OLIS. Stable ^{21}Ne is used rather than taking the measurements with an ^{17}O beam, as the low cross section would make the experiment duration prohibitively long, also, it has the added benefit of saving expensive ^{17}O gas. With the beam on target, DRAGON is part-tuned through the first (charge-selecting) separation stage onto FCCH (the Faraday cup immediately after MD1 and the “charge slits”) where the incident beam current is measured. This is then performed with DRAGON tuned (partly) for each possible charge state (although, dependent on the energy, the DRAGON magnets may not be able to generate a sufficient field to bend the lowest charge states), over a range of energies. Then following on from the work of a previous DRAGON thesis [87], the charge-state distribution for the energies measured in the main experiment can be obtained. The analysis of this stage can be found in Section 5.2.2.

As is mentioned during Section 4.2.1.4 measurements were performed both with, and without, gas being present in the target. Obviously, the experiment proper can only take place where ^4He nuclei are present for the beam to react with. However, several important criteria can only be determined when the gas target is empty, namely the energy of the incident beam, and the energy loss that occurs as nuclei traverse the target gas. The beam energy is determined without gas in the target using Equation 4.8, this is the E_{in} value, the energy going “in” to the target. A second measurement is then taken once the desired target pressure has been achieved and the separator is tuned for the ^{17}O beam, again using Equation 4.8 to determine the energy, only in this case it is E_{out} that is calculated. The energy loss for each set of runs, or beam energy, is then simply the difference between the respective E_{out} and E_{in} .

Finally it should be mentioned that, while not strictly an ancillary measurement in the same sense as those already mentioned, for the lowest energy, $E_{cm} = 0.621$ MeV, a “detuned” run was recorded. The purpose of this detuned measurement was to investigate whether the correct portion of the recoil distribution was being acquired (as shown by Figure 3.5) as for a dipole or quadrupole distribution one would expect to see an increased yield during the detuned runs. The experiment was performed as standard for runs 21258-338 before a 3% detune was applied for the remainder of the beamtime. These standard runs are designated with the subscript “A” in any tables and histogram titles (i.e. “ $E_{cm} = 0.621_A$ MeV”), whereas runs 21339-358, the detune, have the subscript “B”.

4.2.6 Data Acquisition

A schematic of the electronics used by DRAGON is shown in Figure 4.19. Signals from each data source, e.g. the γ -ray detectors and heavy-ion detectors, are dealt with separately, allowing for thorough analysis at the computational stage. The first part of the data acquisition (DAQ) process is establishing an event has taken place; an electronic trigger is required and provided by the BGO array, it being the first detector system encountered by the reaction products. Although Figure 4.19 depicts only BGO's #1 and #30, all 30 PMT's have individual signals split with one output sent to the analog-to-digital converter (ADC) along a coaxial cable bundle causing a 128 ns delay and the second amplified by a factor of 10 before being split a second time and passed to separate modules, leading-edge (LED) and constant-fraction discriminators (CFD). The CFD branch is also directed through an 8 MHz low-pass filter to remove noise before reaching the CFD itself.

Leading-edge discrimination occurs when a pulse crosses some predefined threshold. In this way any electronic noise can be removed due to the amplitude of any generated pulse not being large enough to meet the threshold criteria, as such it is the simplest method to provide a trigger. Alternatively the technique of constant fraction can be used, which removes the effect of signal "walk" where signals of different pulse amplitudes both cross the threshold, inherent with LED. It was found empirically that the best leading-edge discrimination occurred where the threshold was set to 10-20% of the pulse amplitude which produced a signal independent of amplitude for a given shape. The CFD therefore provides improved timing resolution, although the LED is retained due to its better performance for high data rates [79–81, 88]. Each LED output provides the input to a separate time-to-digital converter (TDC) stop. This TDC measures both the leading and trailing edges of the pulse in order that a width can also be calculated and stored to memory. Finally, the RF time signal is made available to correct for any time slewing in the TDC conversions [72].

As can be seen in Figure 4.19, the CFD (and 8 MHz filter) signals are labelled "trig", this is for the very appropriate reason of their being used as the trigger for the system. The separated trigger signals are combined through a series of logic gates satisfying "OR" conditions (see Appendix E) to provide a master gate trigger. The trigger is used to initiate the read-out of data from the ADC for those events meeting the γ -ray threshold [89]. Once the system has been triggered this generates a 1 μ s gate during which the data output from the whole DRAGON system is available to be read into memory.

The heavy-ion (HI) signals from both the ion chamber and MCPs are treated separately from the γ ray events but the principles behind the electronics remain very similar.

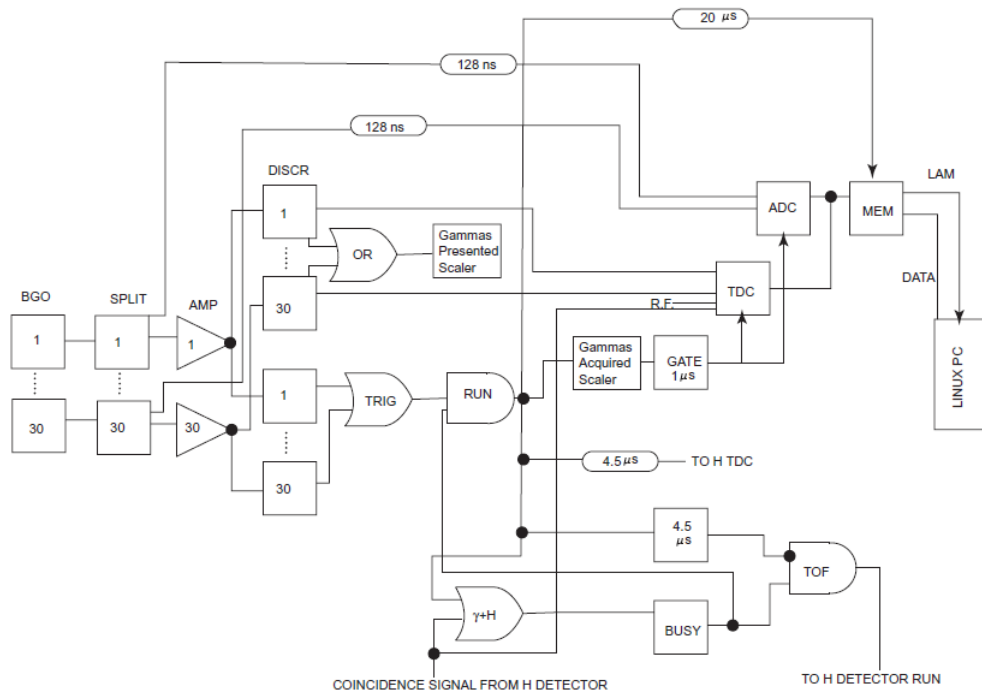


Figure 4.19: DRAGON data acquisition electronics diagram (Amended from [72]). Definition of diagram terminology: ADC (analogue to digital converter), AMP (amplifier), BGO (Bismuth Germanate detector), DISCR (discriminator), MEM (memory), TDC (time to digital converter), H DETECTOR (the ion chamber recoil end detector). The dotted lines between blocks labelled #1 and #30 signify that the circuitry is repeated for multiple detectors (30 in fact). For reference, a reminder of standard electronics logic box symbols is included as Appendix E.

However, instead of a signal being generated from a PMT, it is the ion chamber anodes that produce the pulse. The signal from the relevant plate is then initially pre-amplified before being split after a second amplification stage. Again, the split signal provides a trigger via a CFD and low pass filter [88] as well as an LED output for higher data rates. A major difference is the increase to $4.5 \mu\text{s}$ of a gate. This is specifically chosen to be greater than the full separator time-of-flight. As conditions are met, and triggers fired, analogous to the γ events, the HI TDCs and ADCs read-out their data to their own individual memory banks. In addition, should both γ event and HI event occur within the HI $4.5 \mu\text{s}$ gate, they are labelled in coincidence. The combined γ and HI electronics open a separate coincident gate which writes data to a further memory bank.

The circuitry for the elastic scattering monitors is even simpler still. The surface barrier detector pulse is preamplified before splitting, with the signals sent to a CFD single channel analyser (SCA) which acts as the trigger for the ADC/TDC read-out.

It is also vital to know the deadtime of the DAQ. This is calculated by using the same scalar information already available and takes the form of “triggers presented” and “triggers acquired”. The “gammas presented” scalar, shown on Figure 4.19, is simply the count of all events that meet the threshold requirement of the LED/CFD system and triggered in the manner discussed previously. However, as the electronics require a finite time to read and write data to the computer memory, the trigger also initiates a $20 \mu\text{s}$ stop on further acquisition. Obviously any events occurring within this time period will not be recorded by the DAQ. To establish some measure of this loss of data another scalar (“Gammas Acquired” on Figure 4.19) is positioned ahead of the ADC to record the number of triggers that produce events entering the data stream. The ratio of this triggers acquired value to the total triggers presented is simply the deadtime of the DAQ.

The acquisition of the data is performed using the MIDAS system before being converted into a ROOT format for offline analysis by the KOMODO program [90]. For real-time monitoring purposes basic analysis spectra were produced before the full analysis was then performed offline using the ROOT package. Throughout the experiment there was no need for the operator to perform a manual “runlog”, as the process has been automated with the installation of the rossum-heartbeat program [90]. Rossum is responsible for the hourly Faraday cup readings that separate each “run”. In addition to the cup readings, it also records various data at 5 minute intervals providing a monitor of beam energy, NMR readings for both MD1 & 2, the ED settings and the gas pressure of the target and ion chamber.

4.3 The Experiment - S1216

With the exceptions noted in the preceding sections, e.g. end detector, target pressure, beam species etc., one DRAGON experiment is undertaken very much like another and generally follows the form described in [71, 72]. Here, the specific requirements for the campaign of studying $^{17}\text{O}(\alpha,\gamma)^{21}\text{Ne}$ will be discussed.

A most important decision to be made during any experiment is the energy to be studied. Often this is for precise kinematic reasons or to populate chosen states favourable to the reaction channel of interest. In this case the most important criteria was to maximise any potential yield that might occur, again the point is pressed that low yields and the Coulomb barrier are the bane of any nuclear astrophysics experiment. The original proposal called for a study in the region of $1 < E_{cm} < 2$ MeV, admittedly, far above the Gamow window, but an area where the cross section should be sufficiently high that significant statistics could be acquired in a reasonable run duration [91, 92]. However, with the uncertainties introduced through the necessary extrapolation being not inconsequential the task was changed to break into the Gamow window.

Since the cross section was expected to be $\sim 5 \times 10^{-7}$ b [89] at the originally proposed higher energies, once the decision was made to push even lower, it was necessary to take advantage of the possible resonant structures in the cross section excitation function. Previous data was in short supply (the DRAGON group performing the first experiment on $^{17}\text{O}(\alpha,\gamma)^{21}\text{Ne}$), so the energies of study were selected based on the most extensive work on the (α,n) channel in [35], the results published in [36, 37] being too high an energy for this work (although they were in good agreement with [35] as can be seen in Figure 2.4). The run plan is presented in Figure 4.20 which breaks down the studied energies into ‘‘May’’ and ‘‘November’’ runs. It can be clearly seen how certain energies were repeated in order to test for any systematic effect that might enter play between the two experimental runs.

As a proof of technique, to ensure that DRAGON was indeed functioning correctly, the experiment first probed the highest energy regions to be investigated, $E_{cm} \sim 1.6$ MeV. Corresponding to an (α,n) channel resonance, it was expected that sufficient yield could be quickly attained. After the initial runs the beam energy was successively stepped down, taking advantage of states in ^{21}Ne as shown in Figure 4.20. On reaching the double resonance structure in the (α,n) channel at $E_{cm} \sim 0.8$ MeV a region of unexpectedly high yield, analogous to that of the $E_{cm} = 1.159$ MeV measurement, was encountered. After scanning this resonance, and obtaining more than adequate statistics, the experiment probed further, down to the next strong (α,n) resonance of $E_x = 8.062$ MeV. The subsequent experiment

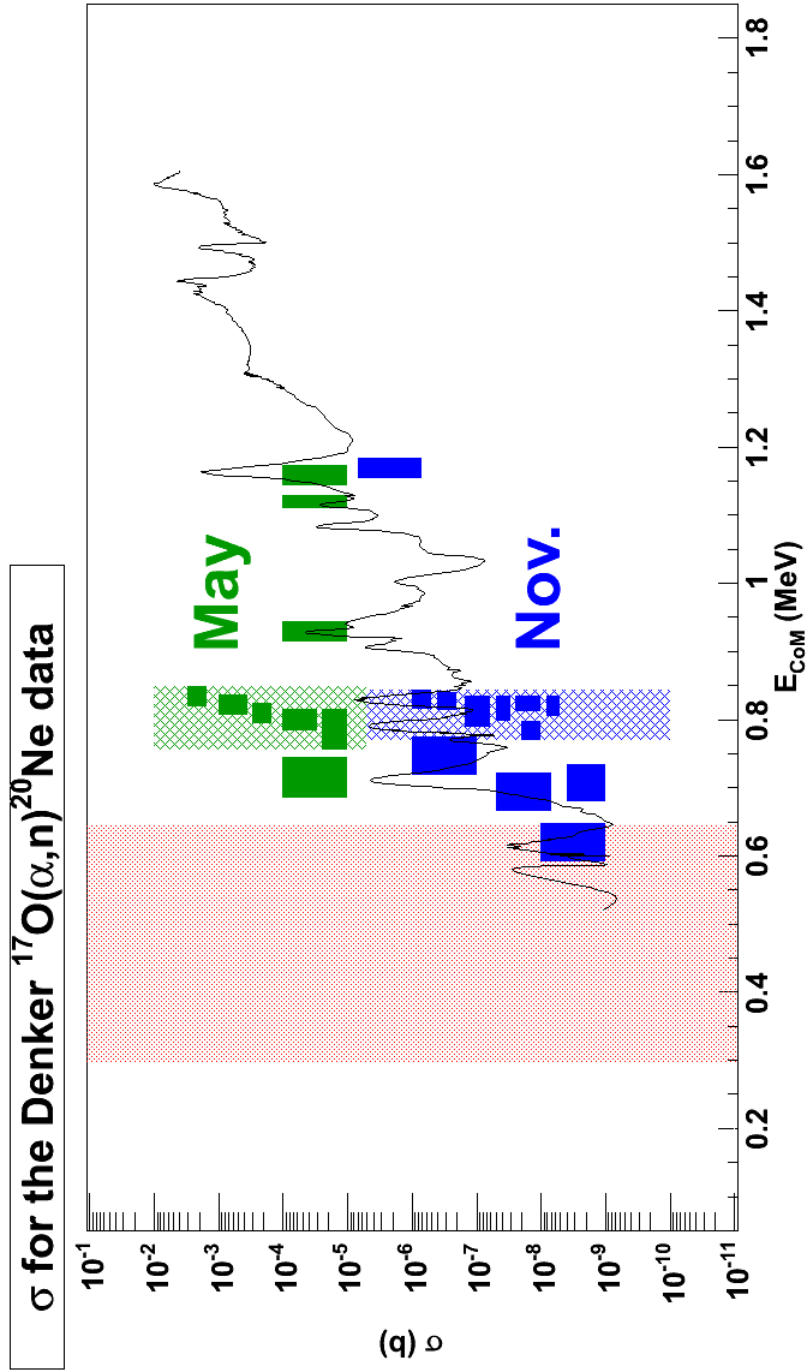


Figure 4.20: In combination with the level scheme presented in Chapter 3 the low-energy (α,n) data [35] was used to select energies to be investigated. Those energies studied during the initial experiment in May 2009 are displayed as green boxes, whereas the later experiment in November is highlighted in blue. Regions of many repeated measurements are displayed as the cross-hatched area and once again the Gamow window is shown as the red band. It is most important to note that there is no Y-axis information in the green and blue boxes.

performed in November used the same selection criteria for beam energies, but with the additional information from the May campaign. A high, strongly resonant energy was selected to provide a check on systematic effects, before a fuller scan of the region of unexpectedly high yield was performed. The scan of the $E_{cm} \sim 0.8$ MeV peak used the same incident beam energy of $E_{beam} = 258$ keV/u, while varying the gas target pressure. In this way different portions of the resonance could be investigated in order to get a better idea of the shape of the distribution.

Finally, as with the May experiment, the energy was pushed lower by centering the gas target energy “bite” on corresponding resonance energies in the (α,n) channel. This allowed DRAGON to perform the first measurement probing the upper portion of the Gamow window as well as establishing upper limits for the region between the states at $E_r = 7.979$ and 8.154 MeV.

Chapter 5

Data Analysis

“Curse my metal body, I wasn’t fast enough, it’s all my fault! My poor master.”

- C3P0

5.1 Overview of Analytical Process

Within the subsequent chapter all the techniques and assumptions made by the author throughout the course of analysing this experiment will be presented, discussed and justified. However, in any experiment with the complexity of DRAGON it is necessary to have some check of the results obtained. For the $^{17}\text{O}(\alpha, \gamma)^{21}\text{Ne}$ study a TRIUMF-based PDRA, Ulrike Hager, performed an independent analysis in parallel to this work.

To aid the reader, it seems necessary to define some of the terminology, particularly when it comes to the identification of the many (see Appendix D) runs. A run is defined as the period of data acquisition between Faraday cup readings. Usually this is an hour long, however, the operator may override this automation for various reasons, e.g. a change in beam energy, charge-state distribution measurements or an attenuated beam run. The runs are then grouped by beam energy for purposes of collating the data. Unfortunately, several energies in difference reference frames are used for different purposes. Unless otherwise stated, the energy quoted will be that of the centre of the target, either E_{cm} or E_{lab} , for the centre-of-mass and laboratory reference frames respectively.

5.2 Calculation of Yield

The first variable to discuss in the calculation of cross section via Equation 3.5 is the reaction yield. Throughout the experiment the raw yield is directly observed as the num-

ber of detected ^{21}Ne recoils. However, some degree of processing, or adjustment, to the raw yield must take place before the cross section can be calculated. This adjusted yield factors in the various efficiency terms of the DRAGON system and is calculated as:

$$Y = \frac{R_Y}{\delta\eta\theta\psi} \quad (5.1)$$

where the adjusted yield, Y , is equal to the raw yield (number of events detected), R_Y , over the efficiency factors of MCP efficiency, δ ; the charge state fraction, η ; the separator transmission, θ ; and, in the case of coincident events, the BGO efficiency, ψ , which otherwise was set to 1. It should be noted here that often the term ‘‘Yield’’ refers to the number of detected recoils per beam particle. In this thesis this definition of yield will be termed the ‘‘Yield per incident ion’’ in contrast to the ‘‘adjusted’’ or ‘‘raw’’ yields referring to the event count only, with and without the efficiency factors included respectively. In general, the discussion will be concerned with single events, defined as any nucleus reaching the ion chamber. The introduction and complications inherent in coincident γ rays will be highlighted when appropriate. The standard format for all particle ID figures will be for ‘‘singles’’ to be displayed in red, and ‘‘coincidences’’ to be displayed in blue.

5.2.1 Selection of Events

DRAGON has various methods of ‘‘good’’ event selection. The use of a recoil mass separator greatly simplifies the process of particle identification. A high quality tune allows for selection with only the bare minimum of analysis required. The standard, or initial, technique used involved plotting the total energy deposited in the ionisation chamber versus local (MCP) time-of-flight, referred to from this point on as the ‘‘ICsumMCPtof’’ plot. Using this technique, a distinct recoil locus away from the arc of the leaky-beam nuclei becomes apparent, as can be seen in Figure 5.1. For this energy, $E_{cm} = 0.811$ MeV, a good tune provided good separation in the preliminary analysis stage, so further analysis was used only for confirmation, as a test of technique. However, many cases, particularly those runs performed during the November experiment, where the tune was often worse, resulted in poorer separation on ICsumMCPtof, the primary analysis stage was therefore not sufficient and further analytical methods were required.

Various combinations of IC anodes were also used to provide ΔE -E analysis, and generally the best separation was found to be when using the total IC energy versus that deposited in the first anode, IC0 (ICsumIC0). The recoil nuclei, entering the separator,

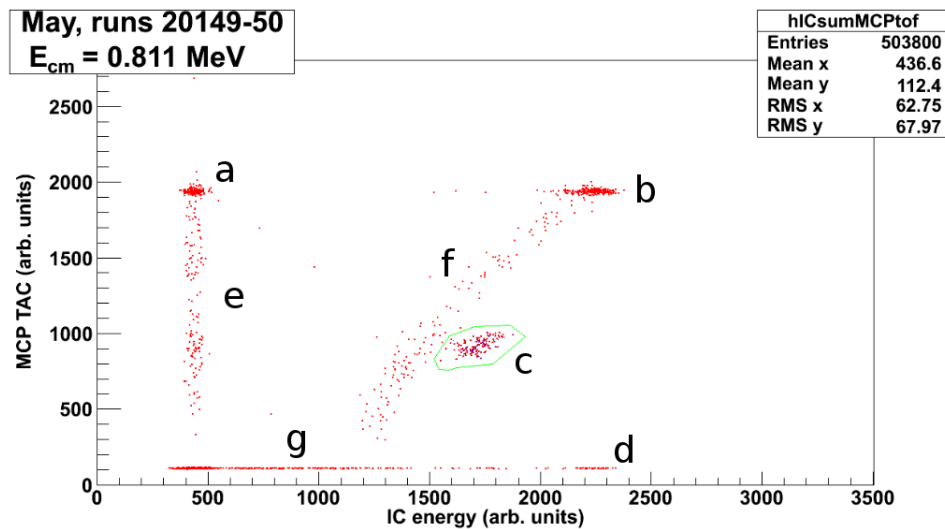


Figure 5.1: The standard analysis technique plotting the total energy deposited in the ionisation chamber (ICsum), on the X-axis, versus the local time-of-flight (MCPtof) on the Y-axis. In this case the separation was sufficient that the ^{21}Ne recoils could easily be distinguished from the ^{17}O “leaky beam” and are passed through the green graphical cut for further analysis. See text for details of the labelling “a-g”.

and subsequently, the ionisation chamber, will have a characteristic energy loss curve. By including a two (or more) stage end detector system, i.e. a ΔE -E telescope, different nuclei will deposit a different portion of their total energy in the thinner, ΔE portion of the ionisation chamber. This allows for separation of various nuclei and enables one to select only the desired nuclei, in this case the ^{21}Ne . An example analysis using this technique is shown in Figure 5.2. However, as with the ICsumMCPtof method, the ICsumIC0 analysis alone would not always achieve the goal (certainly where one technique had failed in isolation the case was the same for the second) and so combinations of analysis techniques were required where one remained insufficient.

Where multiple techniques were combined an initial “preliminary” analysis was performed with extremely wide gates on the standard plot where the whole recoil locus would be selected but also allowing a good portion of leaky beam events to pass through this first cut. These events were subsequently passed into the next projection where separation was easier to achieve. This graphical process can be seen in Figure 5.3 where each successive histogram contains only those events that passed the preceding gate. In this manner, events corresponding to nuclei of different species e.g. ^{17}O , ^{20}Ne or ^{21}Ne , that would otherwise overlap in position on one histogram, can be adequately differentiated so that they might be identified.

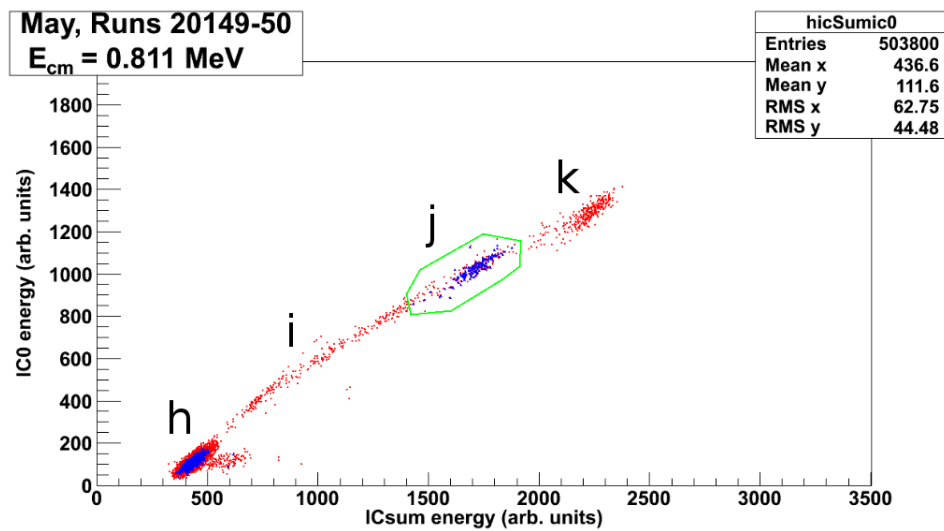


Figure 5.2: The first alternative analysis (although often the macros were run contiguously) examines the separation due to the energy losses of different species through the IC. The data is plotted as the energy deposited on the first anode, IC0 (our ΔE), on the Y-axis, versus the total energy deposited within the ion chamber as a whole, ICSum, on the X-axis. The ^{21}Ne recoil locus is highlighted in green. The labels “h-k” are detailed within the text.

5.2.1.1 Summary of Ion Chamber Histogram Features

The ion chamber combination histograms were the most heavily utilised throughout this analysis, so common, important features (and those not-so-important, but included for clarity) will be briefly discussed here. The colour system for analysis histograms is simply blue for coincident events, red for singles, and grey for a superimposed attenuated beam run, as described in Section 4.2.5.

Now examining Figure 5.1 seven features can be distinguished, which can helpfully be split into two categories, loci and bands. The 4 loci, labelled “a-d” on Figure 5.1, signify events where the recoil has been detected. However, in loci “a” and “d” the event has only registered on either the MCP or in the IC respectively, but not in both. This can be directly compared to loci “b” and “c” which show a number of events recording hits in both detectors, in this case the difference is due to DRAGON working as planned, but not at 100% efficiency. Although DRAGON’s beam suppression is impressive, it is not perfect. As was discussed in Section 4.2.1.2 some beam particles will still “leak” through the separator and reach the end detectors, these are then displayed in locus “b”. Since DRAGON is tuned for ^{21}Ne of a particular energy, these recoils that trigger events on both detectors, then show up as locus “c”, highlighted by the green gate and provides the

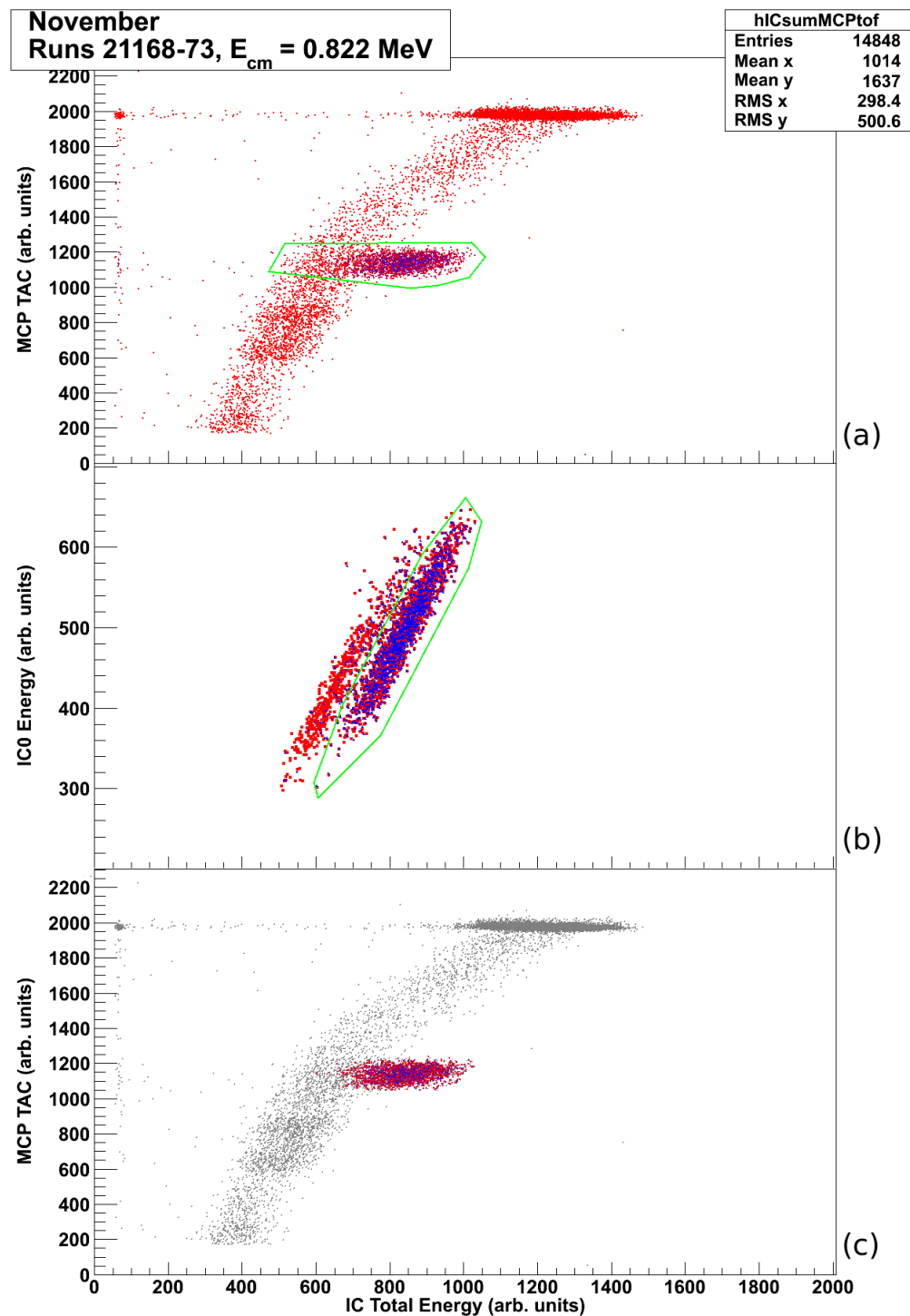


Figure 5.3: Successive analysis stages for the $E_{cm} = 0.822$ MeV measurement. The uppermost figure, *a*, depicts the standard ICsumMCPtof plot, in this case with poor separation. The large graphical cut includes a significant portion of “leaky beam”. Events passing this first cut are projected onto the ΔE - E plot, *b*, the increased separation is clear. Finally, *c*, shows the original ICsumMCPtof data in grey, with those events passing both graphical cuts in red (singles) and blue (coincidences).

raw yield for the chosen run, or runs.

The remaining features of Figure 5.1, the 3 bands “e-g”, are produced where nuclei experience some energy-loss mechanism, possibly scattering within the gas target or beam pipe. This would reduce the energy available to deposit in the ion chamber and results in the observed band. The features labelled “e” and “g” show this energy loss in combination with hits only registering on the MCP or ion chamber, the same cause as “a” and “d”. The band labelled “f” is due to leaky beam particles that have undergone some degree of energy loss.

Likewise, there are a number of features to describe on Figure 5.2. In this case, both axes depict energies as recorded by the ion chamber, so, similarly to feature “d” on Figure 5.1, feature “h” shows events that have not registered in the IC properly. The band, labelled “i”, again corresponds to those leaky beam particles that make it through the separator, and have lost some portion of their energy. Finally, the loci “j” and “k” are due to ^{21}Ne recoils and ^{17}O leaky beam particles, respectively.

5.2.1.2 γ ray Coincident Events

The greatest separation provided by DRAGON comes from the combination of the recoil mass separator and the BGO array. However, the use of the coincident γ rays introduced a further factor ψ into the adjusted yield calculation. The BGO efficiency can be as low as 40% [80]; where yield is already in the region of extremely low statistics, introducing a coincidence requirement would often leave only an upper limit being established. Furthermore the BGO efficiencies were established through GEANT simulations and will be briefly discussed in that section. This led to the “singles” events being the primary data set analysed in order to reduce the uncertainty that would be introduced through a further factor included in the adjusted yield. In some cases, however, there was no option other than to include BGO event data where separation was not clear without the identification of coincident events. In these cases, calculations and results derived using coincident data will be marked accordingly.

5.2.1.3 Separator Time-of-Flight

In addition to the local or MCP time-of-flight there is also a full separator time-of-flight recorded. This compares the time between an event detected in the BGO array and one detected by the end detectors. Two readings are taken here; firstly where the γ event acts as the “start” signal with a “stop” provided either by the MCP or IC, and secondly a “cross-over” where, similarly to the local time-of-flight, the γ event signal is delayed to

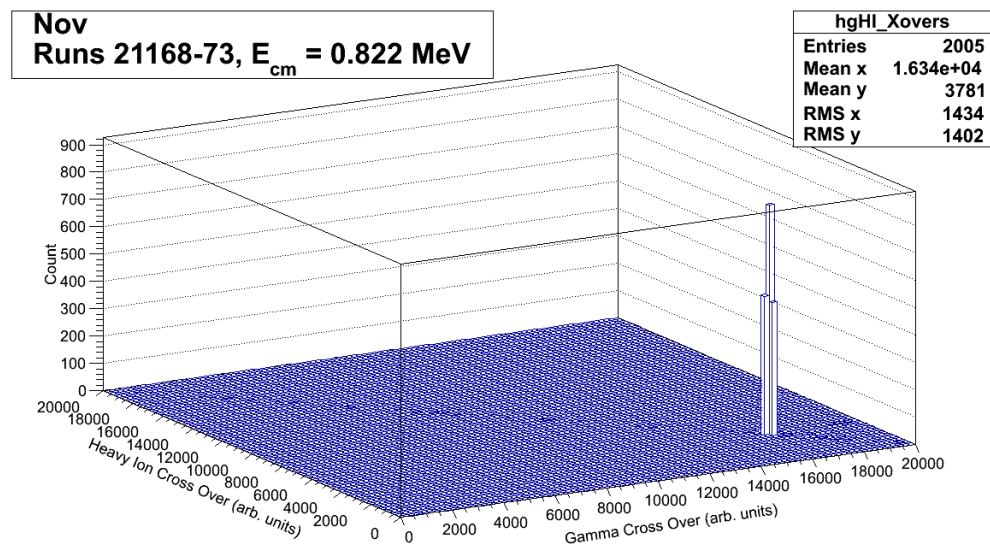


Figure 5.4: Separator Time-of-Flight for the $E_{cm} = 0.822$ MeV measurement. The Y-axis (Heavy Ion Cross Over) displays the TAC value for the BGO start signal and an IC stop. The X-axis (Gamma Cross Over) shows the TAC for an IC start signal and a delayed BGO stop. Both axes are in arbitrary units.

provide the stop with the start due to the end detector event.

Obviously this analysis technique requires the use of coincidence data and introduces our ψ factor and its associated uncertainty. Due to the necessity of coincident data, the technique was reserved for the lowest energy measurements where the previously discussed techniques were insufficient, e.g. where it had not been possible to determine a number of single recoil events. In addition some select high energy points (with their associated higher statistics) were analysed using this method for a proof of technique. In all cases the results showed that the techniques were self consistent.

One of the proof of technique examples is shown in Figure 5.4, for $E_{cm} = 0.822$ MeV, the same data set used to produce the analysis plots in Figure 5.3. The prominent ^{21}Ne recoil peak is clearly visible in the raw plot, which corresponds to the coincident locus in Figure 5.3 at ICsum ~ 800 and MCP TAC ~ 1100 . For this separator time-of-flight plot, no gating was applied; the resonance was strong enough to produce a statistically significant peak. Conversely, the same raw histogram for the Gamow window breaching $E_{cm} = 0.621$ MeV data point shows no such features. Of course, this is as one would expect when examining such a statistically poor measurement.

The technique was most useful for the lowest energies, one example of which is depicted in Figure 5.5 for $E_{cm} = 0.621$ MeV. This shows an ungated time-of-flight plot com-

pared to one where a large graphical gate had been applied around the region indicated by the MCP calibration (discussed in Section 5.2.1.4) on the ICsumMCPtof histogram. Subsequent gating around the low-channel peak on the Separator ToF plot over increasingly tighter ranges was then projected back to the standard ICsumMCPtof plot to determine the location of individual events and whether they were in fact due to recoils or leaky beam particles.

5.2.1.4 MCP calibration

The local time-of-flight (ToF) was calibrated using the known locus for the ^{17}O attenuated beam runs. A linear fit to these beam data enabled a TAC value to be determined for the tuned-for energy of the ^{21}Ne recoils. As always, the tuned energy had been automatically recorded by the rossum-heartbeat system as described in Section 4.2.6.

The calibration for the November energies can be seen in Figure 5.6 and is performed by producing a linear fit to ^{17}O data to establish the relationship between TAC and true time-of-flight, before calculating ^{21}Ne ToF via Equation 5.2 and extracting that TAC value from the previous fit. The time-of-flight is calculated according to:

$$ToF = \frac{0.59}{\sqrt{\frac{2E_{rec}}{M_{21\text{Ne}}\text{amu}}}}, \quad (5.2)$$

where the denominator describes the velocity of the recoil/beam nucleus (E_{rec} and the mass of the nucleus in terms of MeV and amu respectively) and the numerator is simply the distance between the two MCP foils (59 ± 0.5 cm).

For the case of a strong resonant energy, e.g. 0.822 MeV (run numbers 21168-73), this calibration could be confirmed, as we see the strong recoil locus occurring at the appropriate time-to-amplitude converter (TAC) value in Figure 5.3. In this case, the ^{17}O “leaky beam” locus occurring at a TAC value of ~ 2000 is the uppermost data point in Figure 5.6. Correspondingly, the time-of-flight for the ^{21}Ne recoil of 104.7 ns produces a locus at channel number 1135.

This allows a greater confidence when applying gates and graphical cuts for those energies where few recoils are expected and the tune was of a poorer quality, i.e. 0.695 & 0.621 MeV.

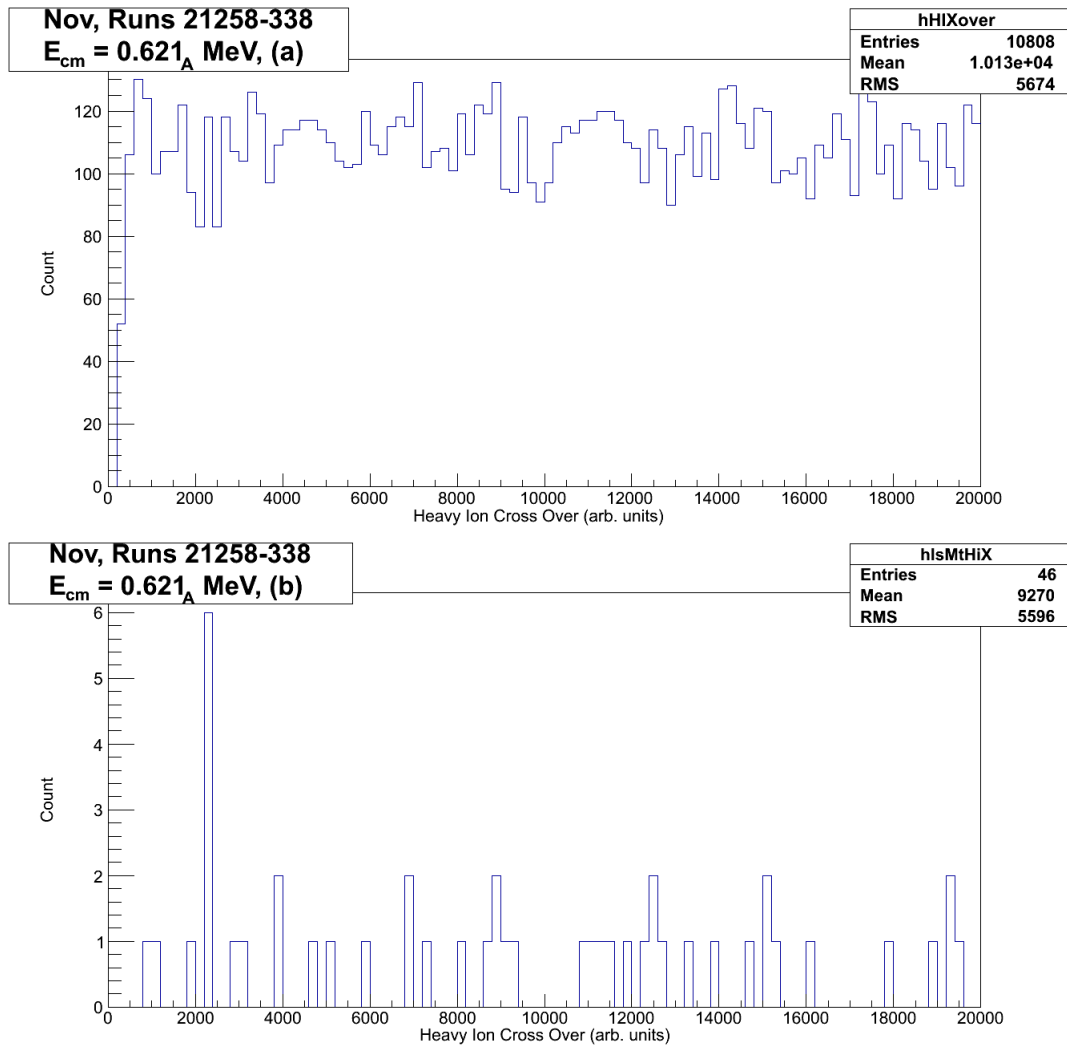


Figure 5.5: Separator ToF analysis. The raw, ungated, data is displayed in (a), whereas that remaining in plot (b) has passed a relatively broad gate on the standard ICsumMCPtof set to remove the obvious leaky beam particles. The subscript, “A”, on the centre-of-mass energy indicates that this was for the set of “tuned” $E_{cm} = 0.621$ MeV runs (see section 4.2.5).

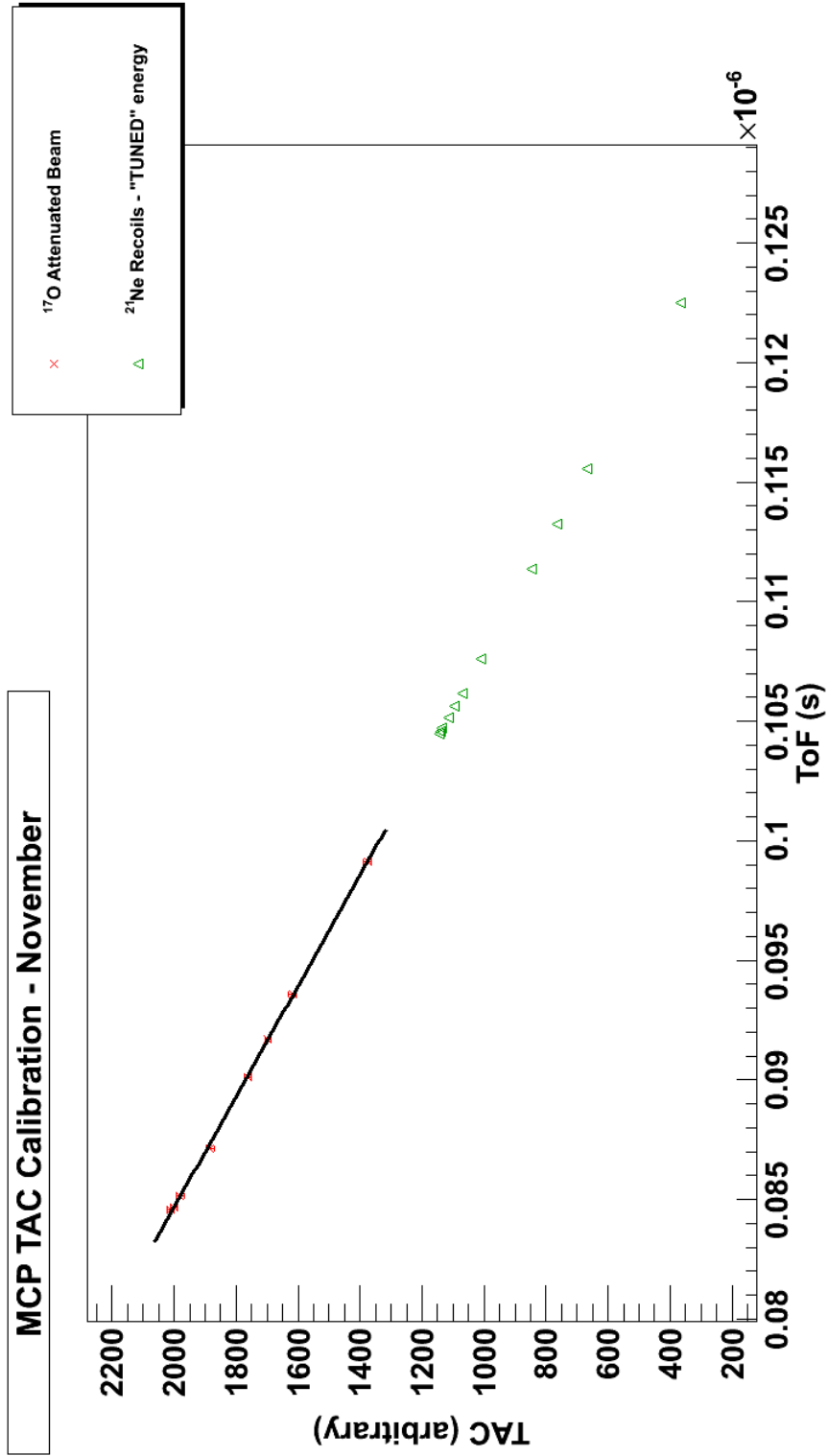


Figure 5.6: Calibration of the MCP TAC for November energies. The TAC value is measured for the ^{17}O beam particles and plotted against the corresponding time-of-flight calculated with Equation 5.2. A linear extrapolation then determines the TAC value for the time-of-flight of ^{21}Ne recoils at each energy.

5.2.2 Charge-state Fraction Measurement and Interpolation

As particles pass through a medium, there is the possibility of orbital electrons being stripped from, or captured by, the nucleus. In this case, both the ^{17}O beam and the ^{21}Ne potentially undergo stripping. The reaction can occur regardless of charge-state, however the DRAGON separator can be tuned to accept only one mass-to-charge ratio at a time. Obviously it is important to maximise the measured yield by selecting the most intense charge-state. This is true regardless of the reaction of interest, but of even more importance when performing measurements of reactions with low cross sections. In order to do this a study of charge-state distribution was carried out. As described in Section 4.2.5 a separate beam of stable ^{21}Ne was utilised for this measurement.

The beam-monitoring program, *rosum*, was used to take a series of Faraday cup readings at various energies. For the incident beam energies of 161.7, 209.64, 298.56 and 383.1 keV/u DRAGON was tuned for charge-states 3^+ to 7^+ , on the condition that DRAGON could sufficiently bend the beam. The magnets are only of a finite size, and therefore there is a limit on the magnitude of field they are capable of producing. A highly-charged nucleus will be easier to bend than one that is singly ionised, likewise an energetic beam will have a greater radius of curvature than one at a lower energy. Fitting a Gaussian to the data points at a specific energy determines the optimum charge-state to be 4^+ and thus enables the raw yield to be maximised during the experiment. Furthermore, this fit gave a measure of the width of the charge-state distribution, the importance of which shall be discussed presently. An example of this determination can be seen for the $E_{\text{beam}} = 298.56$ keV/u measurements in Figure 5.7. As highlighted in [84], only statistical uncertainties are included.

Establishing a semi-empirical formula for the distribution of charge states was the focus of [87], following on from that work a fit can be made to the data and the charge-state distribution across the full energy range of the campaign can be determined. The work in [87] established three formulae which were used in this analysis. These are given as Equations 5.3, 5.4 and 5.5 listed below.

The charge state fraction, F_q , is determined through:

$$F_q = \frac{1}{\sqrt{2\pi}d} \exp\left[-\frac{(q - \bar{q})^2}{2d^2}\right] \quad (5.3)$$

as a function of the charge state, q , the average equilibrium charge state, \bar{q} , and the distribution width, d . The latter two variables are themselves functions, with \bar{q} given by:

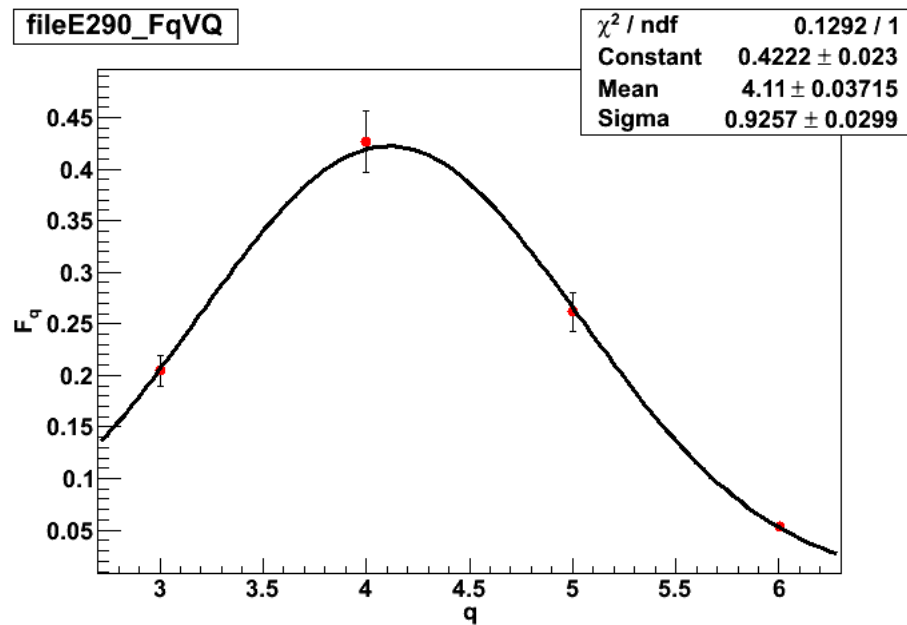


Figure 5.7: Charge state fraction as a function of charge state. For the incident energy of $E_{beam} = 298.56$ keV/u, Faraday cup measurements were taken before the gas target to provide a measurement of total beam current, before DRAGON was tuned to examine individual charge states. With DRAGON then tuned to $q = 3^+, 4^+, 5^+ \& 6^+$ a post-target measurement on FC4 provided the beam current of the individual charge state. It should be noted that the error bars represent statistical uncertainty only.

$$\bar{q} = Z_p \left[1 - \exp\left(-\frac{A}{Z_p^\gamma} \sqrt{\frac{E}{E'}} + B\right) \right] \quad (5.4)$$

where Z_p is the projectile proton number, the variable E' is equal to 0.067635 MeV/u, and the free parameters are A, B and γ , although γ is established to be 0.44515 in the case of helium gas. The expression $\frac{1}{Z_p} \sqrt{\frac{E}{E'}}$ is equivalent to the reduced velocity for a projectile of energy, E, where E also has units of MeV/u. A more thorough discussion of this forms the work of [87]. Finally, the remaining term in Equation 5.3, that of the distribution width, d, is given by:

$$d = d_1 Z_p^w, \quad (5.5)$$

with $d_1 = 0.23675$ and $w = 0.54772$, as established in [87].

To constrain the function due to the limited number of datapoints the distribution width was measured rather than left as a series of free parameters by using the width of the charge-state distribution curves as shown by the example in Figure 5.7 and listed in Table 5.1.

E_{lab} (keV/u)	Width	
161.7	0.131	0.020
209.64	0.297	0.021
298.56	0.426	0.030
383.1	0.387	0.035

Table 5.1: Measured charge state distribution widths and their associated errors. A Gaussian fit to the measured data provides the parameter d that otherwise would be determined through Equation 5.5 and a further two free-parameters.

These functions, Equations 5.3 and 5.4, were fitted to the data of the appropriate charge state, $q = 4^+$, and the charge state fraction factor of the adjusted yield, η , was then subsequently extracted from this fit. The results of the CSF analysis, the factors used in the calculation of the adjusted yield through Equation 5.1, are displayed in Figure 5.8 and as Table 5.2.

5.2.3 GEANT simulations

Transmission efficiencies through the whole separator were calculated through a series of GEANT3 simulations. Initially these simulations were run based on a series of assumptions as the required state information on the ^{21}Ne compound nucleus was not available. This assumed level scheme is shown in Figure 5.9. The use of BGO as a detector medium

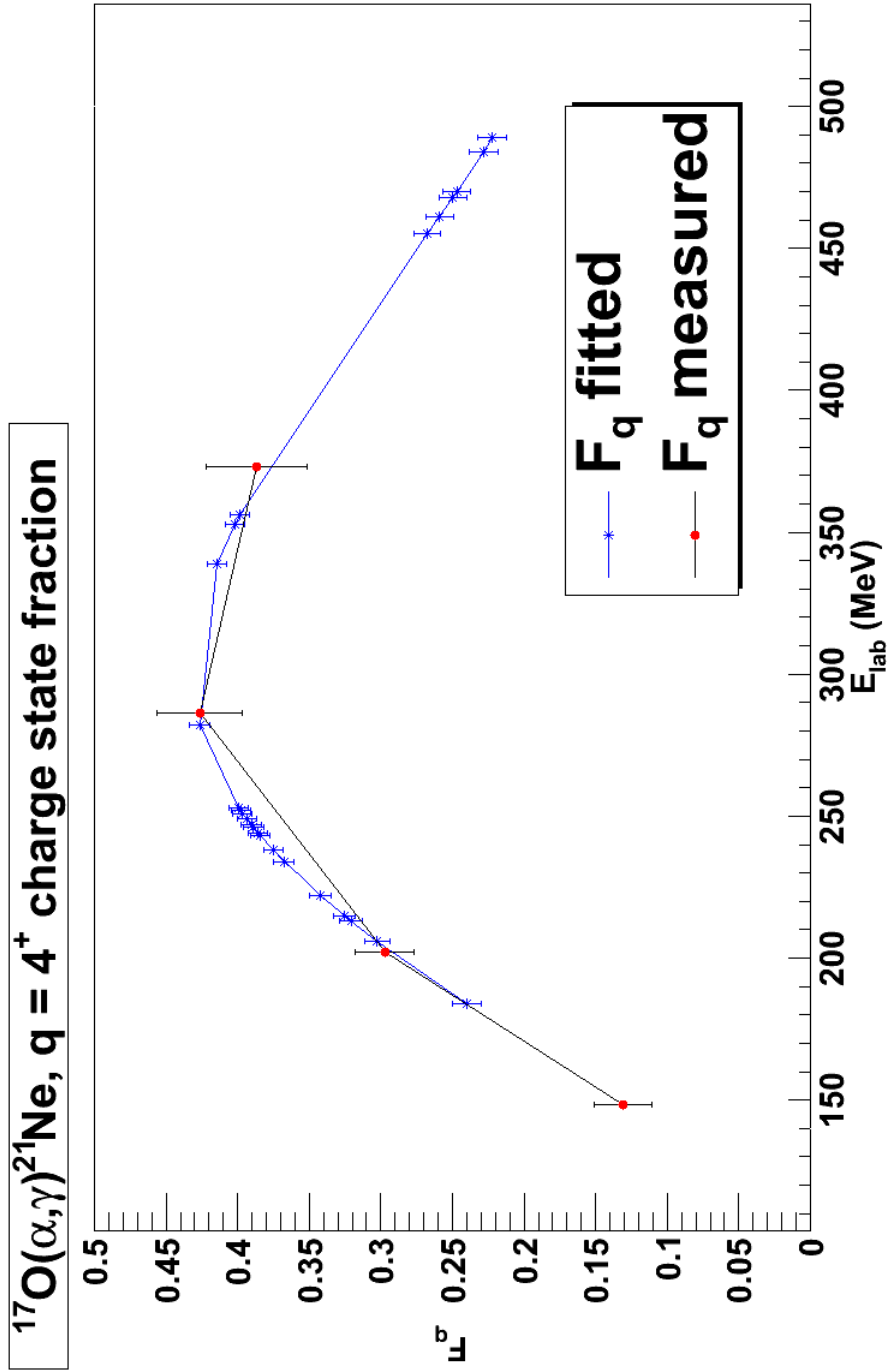


Figure 5.8: Charge state fraction as a function of lab energy. The charge state fraction can be calculated from the fit parameters for each measured energy of the experiment. Data were collected with DRAGON tuned to select ^{21}Ne recoils with a charge state of 4^+ ; the fraction of total recoils that had this charge state is displayed. The blue datapoints are the extracted F_q values, or η , whereas the red points are the measured charge state fractions that Equations 5.3, 5.4 and 5.5 were fitted to.

E_{lab} (keV/u)	E_{CoM} (MeV)	η	
184	0.621	0.240	0.010
206	0.695	0.302	0.008
215	0.709	0.325	0.008
213	0.717	0.321	0.008
222	0.748	0.342	0.008
238	0.785	0.375	0.007
234	0.787	0.368	0.007
243	0.801	0.384	0.007
246	0.811	0.389	0.007
244	0.814	0.386	0.007
247	0.818	0.390	0.007
249	0.822	0.394	0.007
249	0.823	0.394	0.007
251	0.825	0.396	0.007
252	0.829	0.398	0.007
252	0.831	0.398	0.007
253	0.836	0.399	0.007
282	0.931	0.426	0.007
339	1.116	0.414	0.007
353	1.159	0.402	0.007
356	1.17	0.399	0.007
455	1.487	0.267	0.009
461	1.509	0.259	0.009

Table 5.2: The results of the charge state fraction analysis. The fraction of recoils with a charge state of 4^+ is listed for each energy at which the experiment was performed. These are used in Equation 5.1 for the yield calculation.

results in a γ -ray energy resolution of some 10%, which, on an 8 MeV γ ray, is obviously far too great for detailed spectroscopy. Furthermore, the low number of events in the majority of measurements prevented cascade information being determined.

The simulations examined a range of angular distributions, and how the transmission through the separator would be affected by isotropic, dipole or quadrupole γ -ray distributions, as well as investigating the effect of potential resonance parameters, namely the width of any state (or states) present. A discussion of these input variables is also included in Appendix B. The intention had been to compare experimentally measured BGO spectra with those simulated for the same input parameters (beam energy, target pressure etc.) in order to determine the appropriate transmission factor to include in the calculations. However, the parallel analysis did not provide blind agreement on the assignment of transmission and so an alternative approach was deemed necessary.

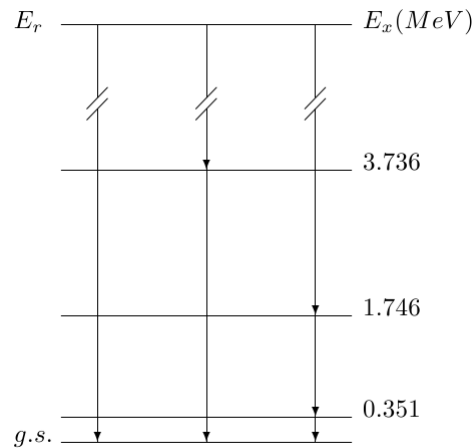


Figure 5.9: The decay scheme assumed for the initial GEANT3 simulations. Note that in all cases a 100% transition was also assumed.

The emitted γ ray from a radiative capture reaction has the potential to influence whether a nucleus enters the separator. This is especially true should a direct to ground-state transition occur, an $\sim 8\text{MeV}$ γ providing quite a “kick” to a recoil nucleus.

To investigate any possible effect this might have upon the recoil’s transmission through the gas target a decay scheme was included in the simulation. As has already been mentioned, only an estimated scheme could be included, due to the absence of significant experimental data. This “stand-in” decay scheme is included as Figure 5.9. The parallel analysis also ran some more complicated estimated decay schemes for selected energies, with additional states at $E_x \sim 6.5$ and ~ 7 MeV. However, the results were found to be very similar to those of the $E_R \rightarrow 1.746 \rightarrow 0.351 \rightarrow 0$ simulation and with the advent of additional data [93] (which will be discussed in a later section), the effort was abandoned [94].

5.2.3.1 Separator Transmissions

Two techniques were attempted to determine an appropriate separator transmission value, θ . A cartoon depicting the differences between the techniques is shown in Figure 5.10. The first, only considered the extremes of the GEANT distribution, calculating a value for Yield and σ with a θ_{Max} and θ_{Min} value. This provided a “best-case” and “worst-case” scenario, where the final value of Yield, σ etc. was calculated as the average of this spread. However, the probability of either of these cases occurring is very low. The θ_{Min} being where a direct to ground state transition occurs near the target entrance, thus significantly broadening the recoil cone due to the “kick” provided by the ~ 8 MeV γ ray. Conversely,

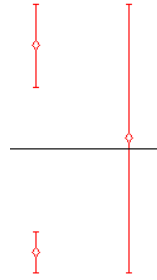


Figure 5.10: This cartoon depicts the effect of considering only the “best” and “worst” cases in terms of separator transmission. Calculations were performed for each transmission factor, providing an upper and lower value for yield/ σ /S-factor. These were then averaged to produce a result that was the mean of the limits of the two values.

the “best-case” would come towards the exit of the gas target where the lowest possible de-excitation of the recoil occurs. While this method is certain to provide a band where the true value must lie, the likelihood that the uncertainties are over estimated is high. Also, any further information that might be derived from alternate scenarios is thrown away.

The second technique considers the distribution of all possible scenarios. By considering the distribution, added weighting is given to those transmissions covered by multiple scenarios and as long as the full phase space is simulated, the mean ($\hat{\theta}$) provides a good estimator of the true value θ . Using this technique we then get the uncertainty of $\hat{\theta}$ by the standard deviation of the distribution. This distribution is depicted in Figure 5.11 showing the average transmission for the $E_{cm} = 0.829$ MeV measurement.

A later measurement was performed by a group at the University of Notre Dame [93] whereby an alternate experimental technique was used which enabled relevant state information to be determined. Further simulations were performed for the $E_{cm} \sim 0.8$ MeV peak which took into account this new cascade information. The inclusion of a full decay scheme allowed for a more accurate calculation of transmission efficiency for one state [55, 93, 95].

Furthermore, analysis of the energy “bite” of DRAGON allowed the confirmation of the location of the 8154.9 keV resonance. This enabled simulations to be performed using the latest γ -ray cascade information as well as the run-specific off-centre resonance position. These results are shown in Table 5.3 where the enhancement of the separator transmission in the November $E_{cm} \sim 0.8$ MeV scan due to resonance position can be seen.

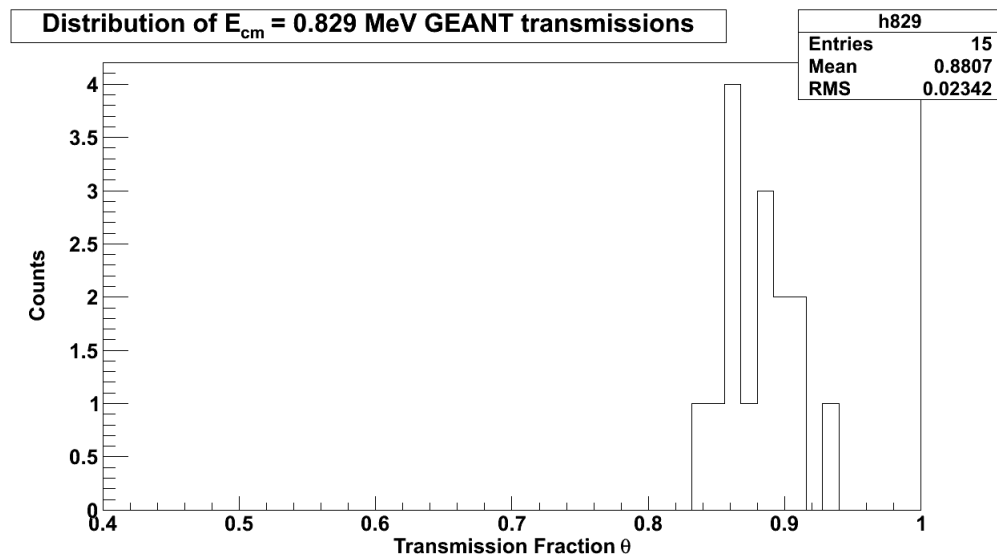


Figure 5.11: Distribution of simulated separator transmission factors for a range of resonance parameters. Separator transmission efficiencies were calculated at each energy for a range of potential γ -ray cascades and resonance widths due to a lack of experimental knowledge. Without further information it was impossible to select the true value, so rather the distribution of transmission factors was produced and the mean value used in the calculations presented in this thesis.

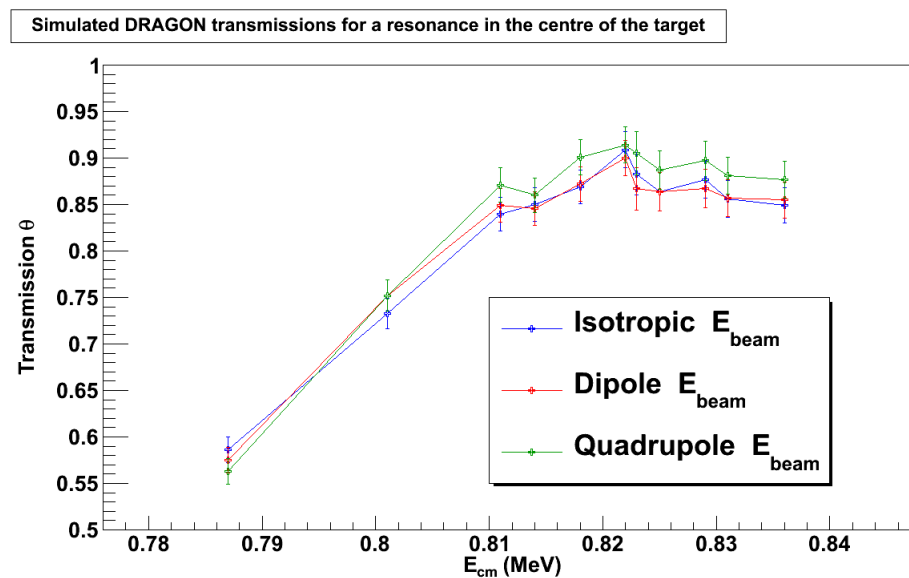


Figure 5.12: Simulated transmission efficiency as a function of resonance energy, for a centre-of-target resonant reaction. Simulations were performed for isotropic, dipolar and quadrupolar distributions to test how this parameter might effect the transmission into the separator.

E_{CoM} (MeV)	θ	$d\theta$	ψ	$d\psi$
0.621	0.34	0.10	0.76	0.02
0.695	0.41	0.10	0.72	0.02
0.709	0.46	0.14	0.71	0.02
0.717	0.44	0.12	0.72	0.02
0.748	0.49	0.15	0.77	0.02
0.785	0.49	0.11	0.74	0.02
0.787	0.61	0.12	0.59	0.04
0.801	0.74	0.10	0.58	0.04
0.811	0.83	0.06	0.59	0.03
0.814	0.81	0.08	0.59	0.02
0.818	0.85	0.05	0.58	0.03
0.822	0.88	0.02	0.59	0.03
0.823	0.87	0.02	0.58	0.02
0.825	0.87	0.02	0.58	0.02
0.829	0.88	0.02	0.59	0.01
0.831	0.87	0.02	0.59	0.01
0.836	0.86	0.02	0.58	0.03
0.931	0.67	0.13	0.76	0.02
1.116	0.73	0.07	0.73	0.02
1.159	0.75	0.06	0.73	0.02
1.17	0.77	0.06	0.75	0.02
1.487	0.87	0.04	0.75	0.02
1.509	0.88	0.04	0.75	0.02

Table 5.3: The results of GEANT simulations to determine θ , the separator transmission, and ψ , the BGO efficiency, where required, with their associated errors. These are used in Equation 5.1 for yield calculation. As described in the text, the reduced value of ψ (and $d\psi$) around the $E_{cm} \sim 0.8$ MeV peak is a result of the increased complexity (and greater accuracy) of the later GEANT simulation.

With the confirmation of the $E_{cm} \sim 800$ keV resonance to $E_r = 806$ keV, it was possible to establish separator transmissions, and BGO efficiencies with greater accuracy. Although, it should be noted that for the peak of interest at $E_r = 806$ keV, such was the intensity (possibly superceding the strength of the neutron channel) that the single event data was almost always sufficient and therefore coincident events and their additional uncertainties could be neglected. Simulations were again run for the $E_{cm} \sim 0.8$ MeV resonance. However, the resonance energy was now known and so could be explicitly stated in the GEANT input files, therefore it was no longer necessary to perform simulations varying the resonance position within the target. Hence the spread of values was reduced resulting in the lower uncertainty for those datapoints. Results for the isotropic distribution are shown in Figure 5.13 (as has been shown in Figure 5.12, the effect of angular

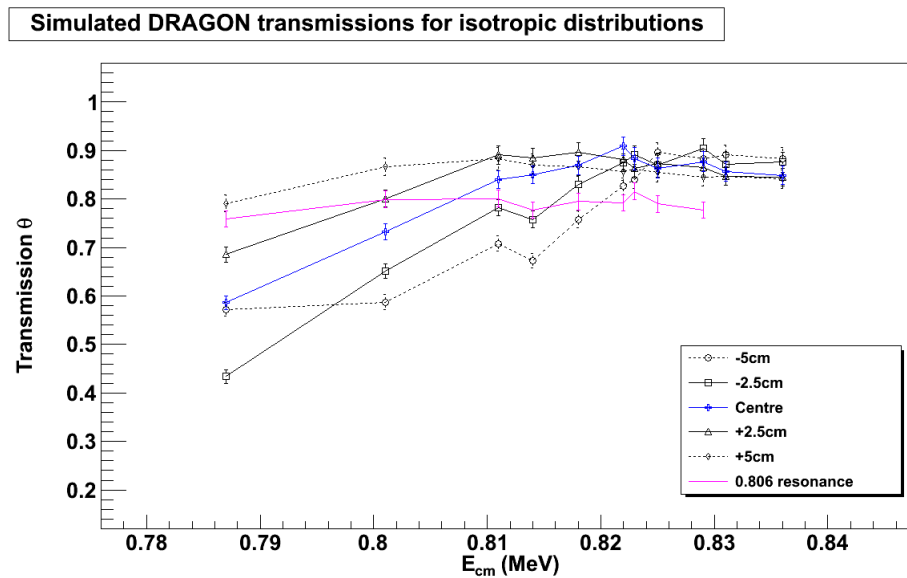


Figure 5.13: Simulated separator transmissions for isotropic distributions at the $E_{cm} \sim 0.8$ MeV peak. Simulations were performed for each incident particle energy for a resonance that would occur in the centre of the target and at ± 2.5 and 5 cm from the target centre. Once the energy of the resonance had been determined (see Section 6.3.1) further simulations were performed for the resonance occurring at its true position. These results are indicated with the magenta line.

distribution is negligible in this region).

5.2.3.2 BGO Efficiency

In the cases where coincident events were used, a factor for the efficiency of the BGO array, ψ in Equation 5.1, was necessary. These were extracted from the same simulations used to establish the transmission efficiency and subject to the same selection criteria. The individual BGO efficiency factors, ψ , for each run energy are presented in Table 5.3 alongside the corresponding transmission efficiencies, θ , and the uncertainties on each.

It is important to note that with the inclusion of additional data, the confirmation of the $E_{cm} \sim 806$ keV resonance and that described later in Section 6.6, a further set of simulations could be performed. These simulations used the full decay scheme, as described in Appendix B. The results of these more sophisticated simulations are shown in Table 5.3 as energies $0.787 < E_{cm} < 0.836$ MeV. This highlights, and explains, an important feature of Table 5.3, the lower BGO efficiencies around the $E_{cm} = 0.8$ MeV peak, which were solely the result of the increased complexity of the later GEANT3 simulation. It is also worth noting that the majority of those datapoints did not require

the use of the factor ψ in the calculation of adjusted yield since sufficient discrimination had been attained with “singles” analysis alone. However, these results are included for completeness. The relevant “singles” or “coincident” yields are listed in Appendix A in Table A.1.

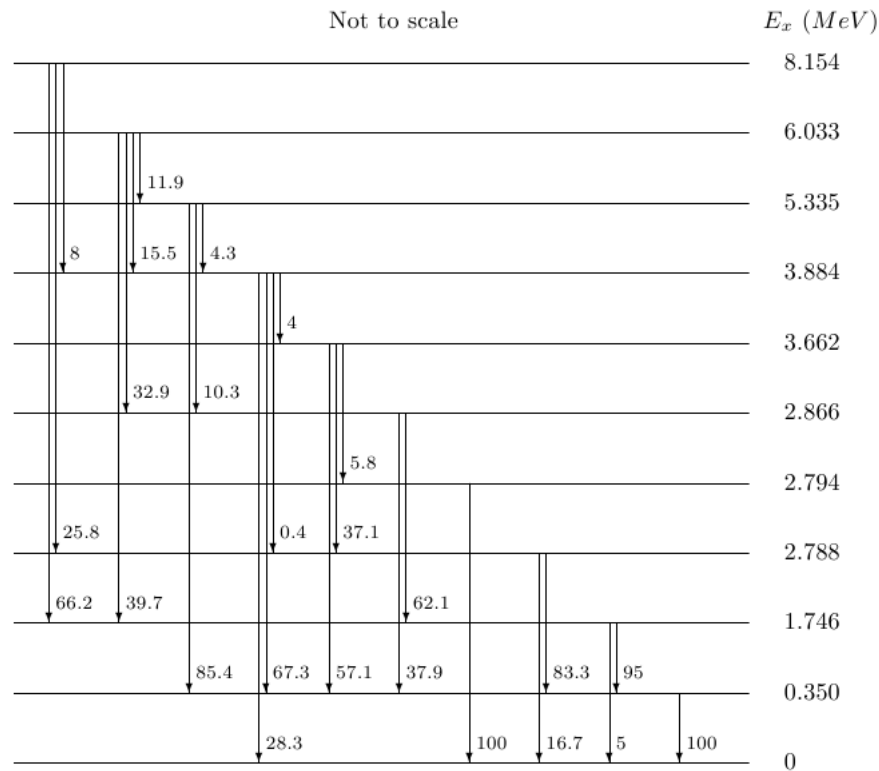


Figure 5.14: The decay scheme used for the latter GEANT3 simulations utilising the additional state data from [93]. The branching ratios (as a percentage) for each mode can be found to the right of each transition as well as in Appendix B.

With the inclusion of the more detailed level scheme depicted in Figure 5.14 the reliance on assumptions made in the scheme shown in Figure 5.9 is removed. In this case, information on branching ratios was also included (shown both in Figure 5.14 and in the input card code snippet in Appendix B), as opposed to the original simulations which assumed 100% transitions between each state listed. The simulation was only rerun for those measurements around the $E_{cm} = 806$ keV resonance.

The inclusion of many more states in the detailed level scheme requires that for the same total energy, more γ rays of lower individual energies will be emitted. The effect this has on the separator transmission has already been discussed, but the BGO efficiency will also be sensitive to the change in state information. If Figure 4.15 is revisited, it is clear that the efficiency of BGO is higher for these lower energy γ rays. However, DRAGON

utilises a hard 2 MeV CFD γ -ray threshold, a feature which is replicated in the extraction of the BGO efficiencies from the GEANT3 simulation. This threshold removes many of the low-energy γ rays from consideration (as well as any random coincidences) which has the effect of a reduced BGO efficiency around the $E_{cm} = 806$ keV peak, since, when averaged, the simple cascade schemes (as shown in Figure 5.9) have a greater proportion of “lower-energy” γ rays which still remain above threshold. It is also important to note that the majority of points around the peak had sufficient statistics that the BGO efficiency numbers were not included in the calculation of cross section due to singles data being sufficient.

5.2.4 MCP Efficiencies

The MCP efficiency factor, δ_M , in fact comprises two components. The first, the efficiency of the MCP itself, i.e. the proportion of real events detected, the second a transmission factor due to the foil having a finite stopping power itself. The efficiency of an MCP can be extremely good, with >99% not unheard of. However, incident beam energy, foil integrity and size of beam-spot can all effect the efficiency value, so these must be calculated for each experiment.

The efficiencies of the MCPs were calculated using the ICsumMCPtof plots for the various attenuated beam runs taken at several energies throughout the experiment. Three loci were established on these plots, shown in Figure 5.15, whereby the efficiency could be determined from the ratio of “good” MCP events (those where an MCP reading was recorded above background) to total events for the projection of the beam locus. The loci are labelled “B”, for good hits by beam particles, “M”, for those particles recording a hit on the MCP but with no corresponding ion chamber information, and conversely “I”, where a hit was only recorded for the ion chamber. This ratio, δ_M , is simply calculated according to:

$$\delta_M = \frac{B + M}{I + B + M} \quad (5.6)$$

with the terms B, M and I corresponding to the number of entries that pass the corresponding gates as shown on Figure 5.15. These efficiencies were then averaged across each experimental data-set which provided values of $\delta_M = 0.79 \pm 0.03$ in the May experiment, and of $\delta_M = 0.87 \pm 0.05$ for those energies measured in November.

The alternative method compared the number of peak ^{17}O beam events (those corre-

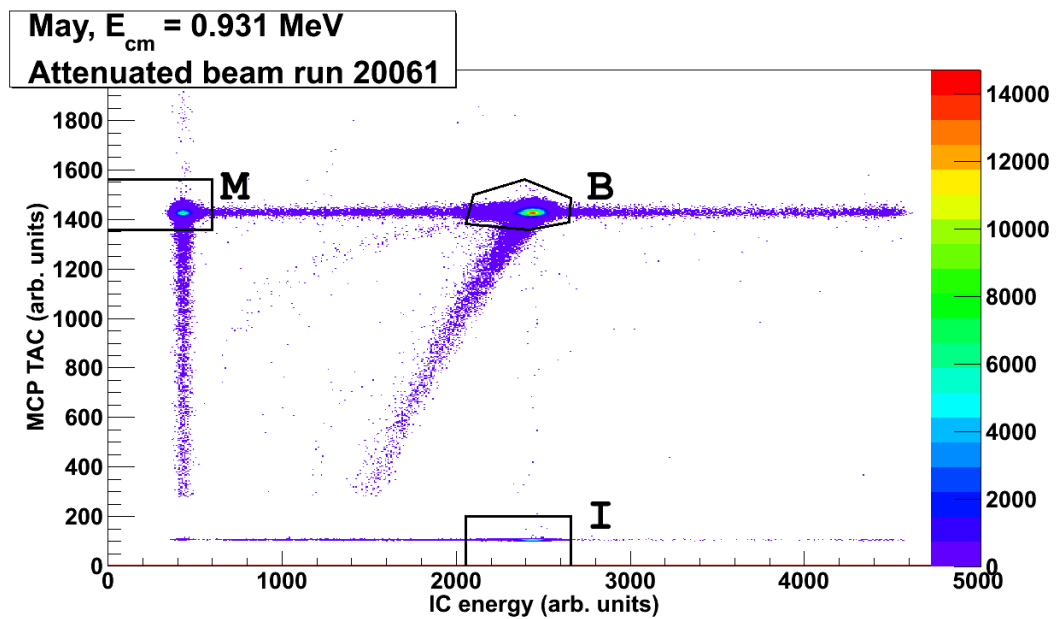


Figure 5.15: The MCP efficiency is determined from the standard ICsumMCPtof histogram of the attenuated beam. In this example the $E_{cm} = 0.931$ MeV run is shown. A cut is made on the main beam locus, “B”, then cuts are projected onto the Y- and X-axes for the same respective range as that of the beam locus for the relevant axis. “M” and “I” correspond to events recording a hit on either the MCP or ion chamber only respectively. The efficiency is calculated as the ratio of good MCP events versus total events.

sponding to cut “B” on Figure 5.15) in ICsumMCPtof and ICsumIC0 histograms. This compares ion chamber events that require the MCP to be triggered to those that have no need for MCP involvement whatsoever, the ratio of the two will therefore provide another measure of MCP efficiency. The two techniques showed comparable results with the alternate method providing $\delta_M = 0.79 \pm 0.03$ and 0.88 ± 0.03 , for the May and November experiments respectively.

The second factor of the MCP efficiency is primarily a geometric variable. As can be seen in Figure 5.16 the MCP foil is held in place by a supporting wire mesh. This nickel-plated mesh will reduce the transmission of beam and recoil particles through a geometric effect, having a substantially higher stopping power than the carbon foil. This has been the subject of a previous study [83], and the transmission given there of $76.9 \pm 0.6\%$ is used in this work.



Figure 5.16: MCP foils - On the right the foil has already been positioned and is ready to be installed in the MCP box; on the left is an untrimmed mount where the supporting mesh is clearly visible.

5.3 Total Integrated Beam

The second variable in calculation of the cross section is the number of incident ions, or total integrated beam. The beam is monitored in real time by elastic scattering of target gas nuclei as well as a precision measurement at the conclusion of each run using the Faraday cups on linear drives so that they can be positioned directly in the beamline. The relationship between the two must therefore be determined in order to establish a true measurement of the variable, I .

5.3.1 Measurement of Elastics

Realtime beam intensity monitoring was provided by detection of elastic scattering of the ^4He target nuclei. Two surface barrier detectors are located within the target box at a 30° and 57° offset from the particle beam (see Figure 4.10). Elastic scattering measurements allow for a continuous monitoring of the number of incident ions whereas the more precise method using Faraday cups of course interrupts the beam.

Integrating across the scalar data for a whole run, an example of which is shown in Figure 5.17, provides a measurement of the number of elastics. For energies which required a longer measurement duration the number of elastics in each run were summed

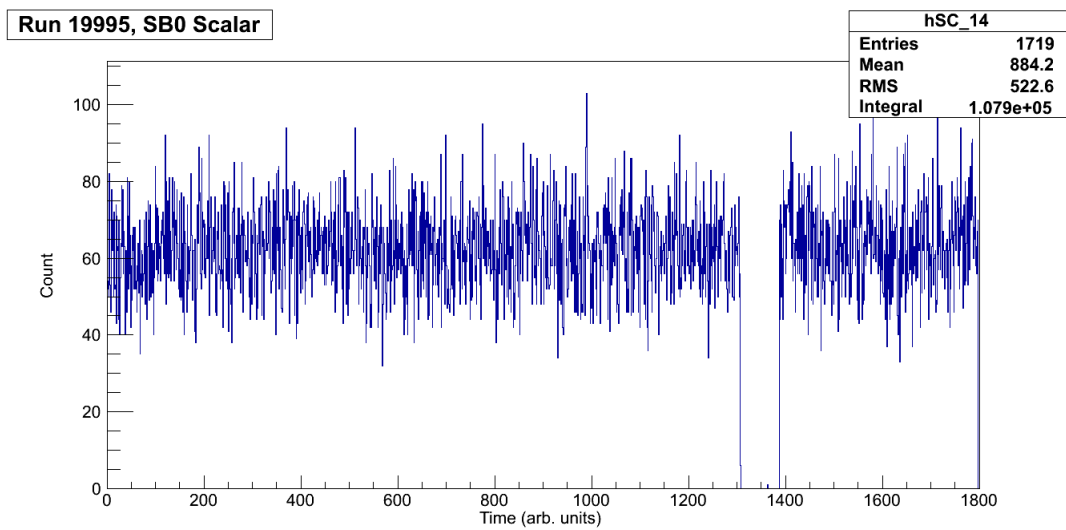


Figure 5.17: An example of elastically scattered particles detected by the SB0 scalar as a function of time, in this case, for run 19995 at $E_{beam}=492.2$ keV/u. The sudden drop at 1308 is indicative of a Faraday cup being inserted into the beamline upstream of the target for ISAC operations diagnostics.

together and that value was used in the calculation of incident beam.

5.3.2 True Beam Measurement

A precision beam measurement was made on a regular basis. At the end of each run, standard duration of 1 hour, an automated system started whereby the beam was interrupted and a series of cup readings (plus additional, relevant analysis data) was taken. The DRAGON facility contains Faraday cups at several points along its length. While readings are being taken, FC4, located immediately upstream of the target, is inserted on three separate occasions in order to obtain an average value.

The cup measurement program, *rossum*, also inserts cups to take additional readings. As well as FC4's pre-target measurements there is also a post-target cup, FC1, positioned just downstream of the target, the combination of these two is used during tuning procedures to establish the target transmission, typically $> 95\%$. A further cup allows for monitoring of the transmission into the workings of the separator proper, with FCCH positioned downstream of the first separation stage, MD1. The stability of these readings can be seen in Figure 5.18. Likewise, the current measurement during each cup's insertion and withdrawal follows a distinctive shape and must be removed from the analysis for accuracy.

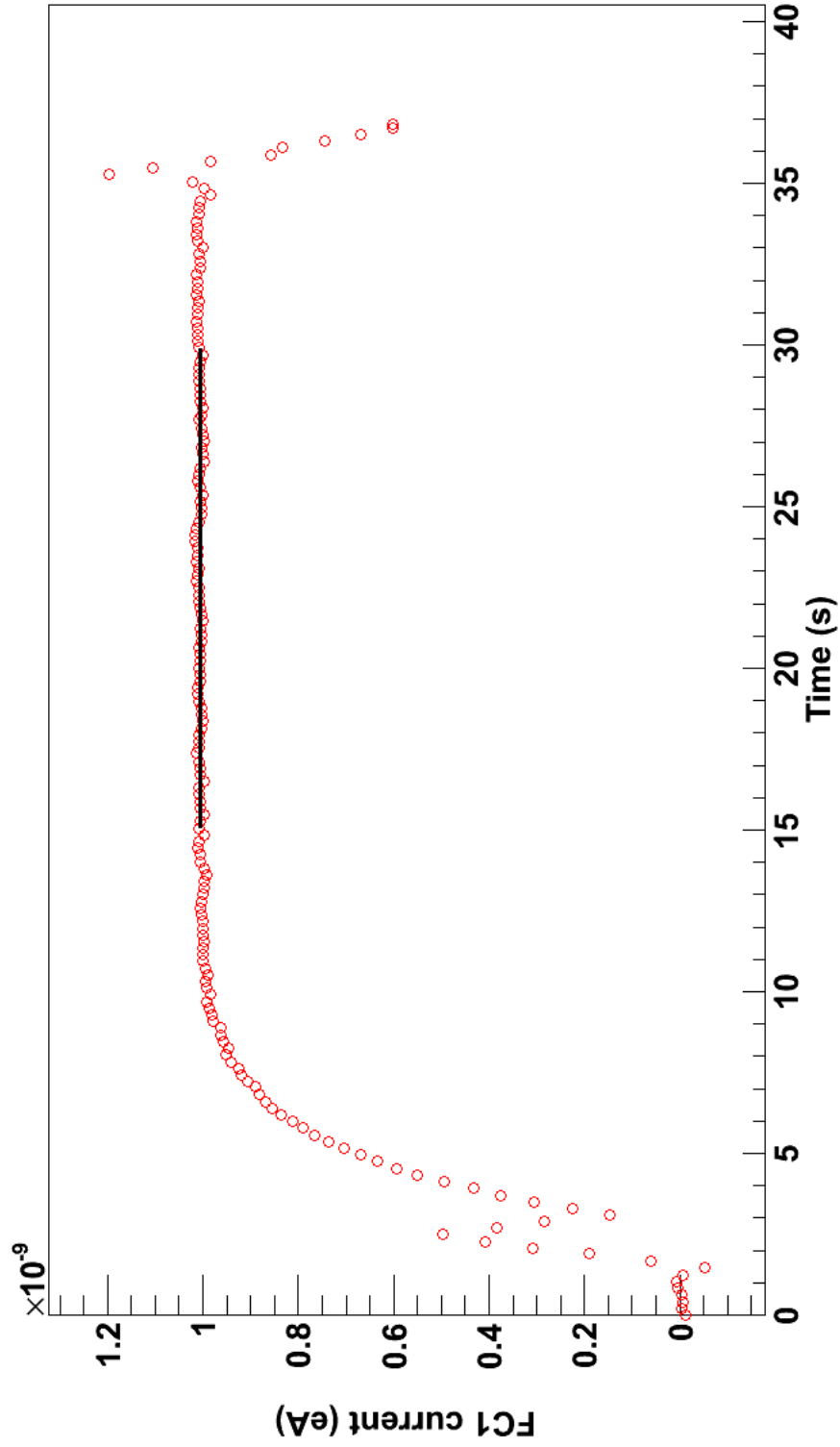


Figure 5.18: An example of beam current as a function of time, taken from the automated Faraday cup measurements. In this case FC1 during the measurement of the charge state distribution for $E_{beam} = 383.1$ keV/u, $q = 4^+$. The stability of the beam current is clear to see, with a systematic uncertainty of better than 1% [76]. The error on the current reading is taken as the width of a Gaussian fitted to the data points lying under the black line.

A 15 second section is selected (from a total of 30s cup measurement duration), with the data points fitted to a Gaussian for the centroid to be taken as the reading, and the associated error from the full-width half-maximum.

5.3.3 Beam Normalisation

The technique used for normalising the DRAGON beam has previously been discussed in [71]. This work makes use of the same method whereby the detected elastic scatters are related to a direct beam current reading.

Our normalisation factor, “R”, was calculated through:

$$R = \frac{I/q}{e} \frac{\Delta t}{N_{\alpha} E_{beam}^2 / P} \quad (5.7)$$

where in this case N_{α} is the number of elastically scattered α particles detected by the surface barrier detector during a time period Δt . For this analysis Δt was selected to be 60 seconds. The true beam measurement is “I” and its charge state on entering the target is given by “q”, which for this experiment was 3^+ . The incoming beam energy in units of (keV/u) is given as E_{beam} and the target pressure, “P”, in units of (Torr). There remains only the charge on the electron, e , which of course is 1.602×10^{-19} C.

The real-time elastic scattering was monitored by the two surface barrier detectors, which through simple kinematics recorded very different numbers due to the different locations (30° and 57°). This produces two self-consistent beam normalisation factors with which to determine the total integrated beam. These factors must then be scaled by the run-specific E_{beam}^2/P terms and the corresponding elastic scattering data for the entire duration of the run. Due to the increased number of statistics and therefore reduced uncertainty, the beam normalisation used for calculations was that of SB0 (the 30° angled surface barrier detector) although the results with SB1 were also calculated and found to be consistent.

An example of the SB0 beam normalisation factors is displayed in Figure 5.19, corresponding to those of the November experiment. The noticeable increase in beam intensity for the end of the November run is quite clear. Incidentally, this corresponded to DRAGON’s highest recorded beam intensity of $\sim 10^{12}$ pps.

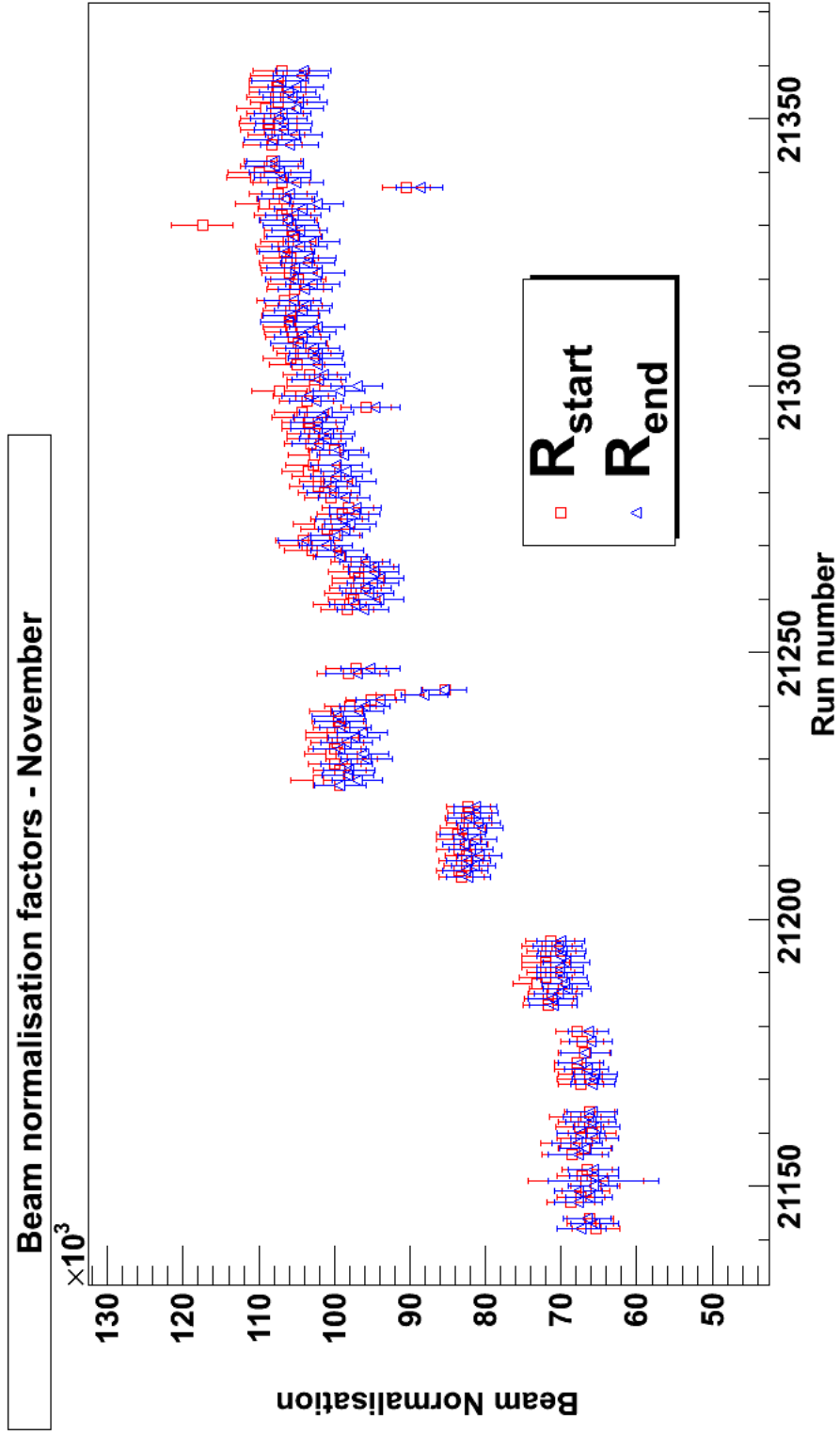


Figure 5.19: Calculated beam normalisation factors for each run for the November energies. The terms R_{start} and R_{end} correspond to calculations using cup readings at the beginning and end of the runs, respectively. Anomalous readings due to aborted measurements or unusable runs were removed prior to implementation.

5.4 Target Nuclei

The remaining cross section term is the number of target nuclei present in the reaction. This is calculated as a number density per apparent area rather than a raw number. Using the ideal gas law it is possible to calculate this value with the target pressure as the only real variable term in the equation. As can be found in any textbook, the ideal gas law is defined as:

$$PV = nRT \quad (5.8)$$

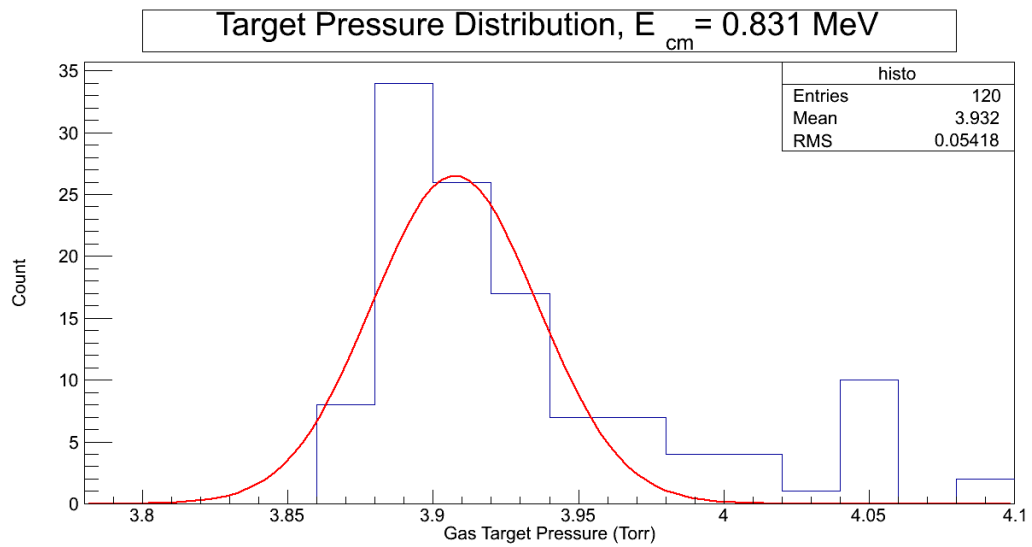
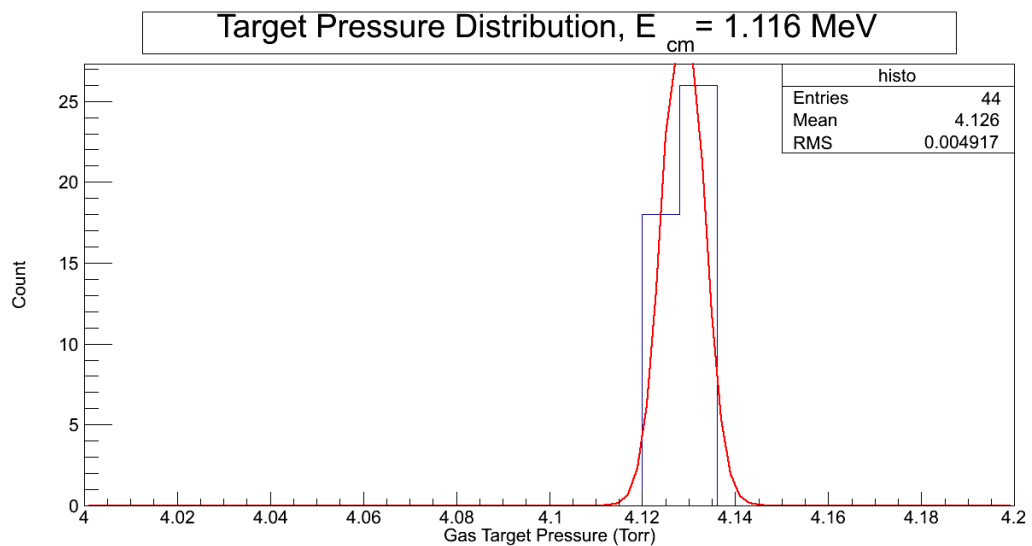
which can be rearranged to give N , the number of target nuclei per unit area:

$$N = \frac{PL}{RT} \quad (5.9)$$

where the effective length of the gas target, L , is known to be 12.3 cm [72] and the value of the universal gas constant, R , is $62.36367 \text{ l}\cdot\text{Torr}\cdot\text{K}^{-1}\cdot\text{mol}^{-1}$. The target pressure, P , was continually monitored and recorded at 5 minute intervals. For each energy, the spread of these pressure readings was looked at and found to be extremely stable, usually staying within 0.01 Torr during the course of a run (1 hour duration). Variation only occurred for those energies with longer duration (>10 hours) run times, in which case the centroid of a fitted Gaussian was taken as the value, with the uncertainty derived from the standard deviation. The excellent stability of the target is apparent in Figures 5.20 and 5.21 which have run durations of 10 hours and 3 hours 40 minutes respectively.

The temperature, T , had previously been measured with a thermocouple [76] and was monitored during this work although not recorded into the data stream. The temperature was taken as a nominal $300 \pm 5 \text{ K}$ with the combination of heating due to the pumping systems and the cooling effect of the zeolite trap found to aid stability in this aspect. This allows the calculation of the number of target nuclei per unit area which is shown in Table 5.4.

This leaves the number of target nuclei as being the most straightforward portion of the whole analysis, one real piece of information and one calculation to perform. However, as is found in [96] this is rarely the whole story, and two further pieces of the puzzle were checked before the numbers presented in Table 5.4 could be finalised.

Figure 5.20: Target Pressure Distribution for $E_{cm} = 0.831$ MeV.Figure 5.21: Target Pressure Distribution for $E_{cm} = 1.116$ MeV.

E_{CoM} (MeV)	Pressure (Torr)	atoms/unit area (cm^{-2})	error (%)
0.621	8.04	3.18e+18	3.9
0.695	8.38	3.32e+18	3.7
0.709	4.03	1.60e+18	3.7
0.717	8.12	3.22e+18	3.7
0.748	8.00	3.17e+18	3.7
0.785	3.96	1.57e+18	3.7
0.787	8.36	3.31e+18	3.7
0.801	4.04	1.60e+18	3.7
0.811	4.06	1.61e+18	3.7
0.814	6.26	2.48e+18	3.7
0.818	5.16	2.04e+18	3.7
0.822	4.13	1.63e+18	3.7
0.823	4.17	1.65e+18	3.7
0.825	3.11	1.23e+18	3.7
0.829	4.03	1.60e+18	3.7
0.831	3.91	1.55e+18	3.7
0.836	4.05	1.60e+18	3.7
0.931	3.99	1.58e+18	3.7
1.116	4.13	1.63e+18	3.7
1.159	4.10	1.62e+18	3.7
1.170	4.00	1.58e+18	3.7
1.487	4.05	1.61e+18	3.7
1.509	4.06	1.61e+18	3.7

Table 5.4: Calculated number of total target nuclei and the one variable, pressure, for each investigated centre-of-mass energy.

5.4.1 Thick Target Yield and Resonant Reactions

The above technique is perfectly valid when considering a flat cross section, one where the probability of reaction can be considered not to change across the energy “bite” of the target. However, should the target be larger than the width of the state, this is no longer strictly true.

Considering again an isolated resonance at the centre of the target, as can be seen in the cartoon in Figure 5.22, the reaction yield will come almost entirely from that portion of the target where the energy matches that of the resonance (see Figures C.1 and C.2 in Appendix C). This would result in a decrease of the number of target nuclei at the resonant energy and therefore available to the interaction. In the case of resonant reactions for a thick target, this would underestimate the calculated cross section.

Two approaches to solving this issue become clear. The first would require that detailed knowledge of the shape of the resonance be known. Knowing the width of the

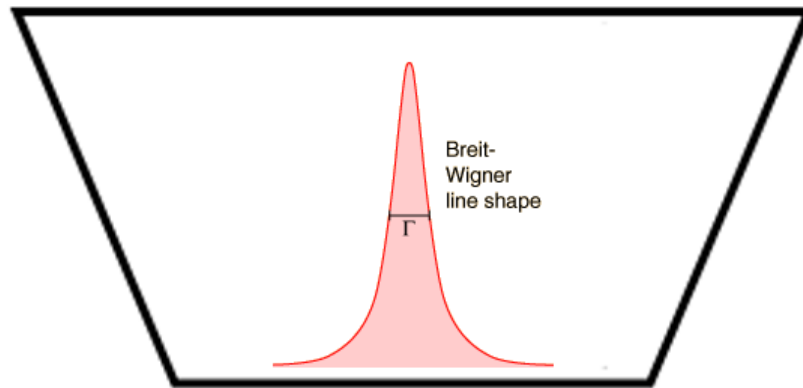


Figure 5.22: Cartoon of the gas target with a resonance positioned near the centre of the energy “bite”. For a flat, non-resonant, cross section the total volume of the trapezium is used to calculate the number of target nuclei. Conversely should a resonant state be present, only those nuclei lying under the Lorentzian distribution will contribute to the reaction.

resonance, and therefore the contributing portion of the target’s energy “bite”, one knows the ratio of nuclei within the resonance to nuclei within the target. The true number of nuclei in the reaction, N_r , is given by the geometric overlap of the resonance width, Γ_γ , and is of the form:

$$\frac{\Gamma_\gamma}{E_{bite}} = \frac{N_r}{N_t} \quad (5.10)$$

where N_t is the total number of target nuclei, and E_{bite} is given by:

$$E_{bite} = E_{in} - E_{out}. \quad (5.11)$$

This value could then be substituted into the calculation for cross section in order to accurately obtain a result.

In the case of the $E_r \sim 806$ keV resonance, as discussed previously the repeated measurements with various energy coverage allowed the definition of the width parameter,

Γ_γ . The “bites” of these measurements, which is defined as the energy lost by the particle as it travels through the target, and is described by Equation 5.11, were of the range $24.0 \leq \Delta E_{cm} \leq 51.8$ keV. For these measurements the calculated value of N_t , the total number of target nuclei would require the factor given in Table 5.5 in order to calculate resonant cross sections.

E_{cm} (keV)	$\frac{\Gamma_\gamma}{E_{bite}}$
801	0.565
811	0.565
814	0.363
818	0.439
822	0.541
823	0.509
825	0.688

Table 5.5: Calculated fraction of total number of nuclei in the gas target that contribute to resonant yield for the points surrounding $E_{cm} \sim 0.806$ MeV. Since the method described in the text is not used for the analysis, and no resonant cross section is calculated, the uncertainties are omitted from the table.

The alternate approach is one of simplicity and removes the issue completely. While it is entirely correct that in order to calculate the cross section for a resonant reaction the experimenter must know the number of target nuclei involved in the reaction, this is not the case when dealing with resonance strengths. The calculation, as given by Equation 3.24, does not include a target nuclei term. Instead it deals only with the stopping cross section, which is measured directly during the experiment by MD1 as the beam energy with and without gas in the target. The measurement “without gas” is the incident energy of the beam before any energy loss via target transmission occurs. Conversely, the measurement “with gas” gives the beam energy on its exit from the target, and from the combination of E_{in} and E_{out} the stopping cross section is established.

Due to the uncertainties surrounding the limited state information, cross sections were calculated assuming a flat, non-resonant cross section, that is to say the total number of target nuclei were included. For measurements where a resonance was suspected, either from our own measurements (as in the case of $E_{cm} \sim 0.8$ MeV), evidence that one exists in the (α, n) channel [34], or from state information [95], the $\omega\gamma$ was used to determine the resonant contribution to the reaction rate at that point. The datapoints that were taken to be resonant contributions are listed in Table 6.2 during the discussion on the resonance strength in Chapter 6.

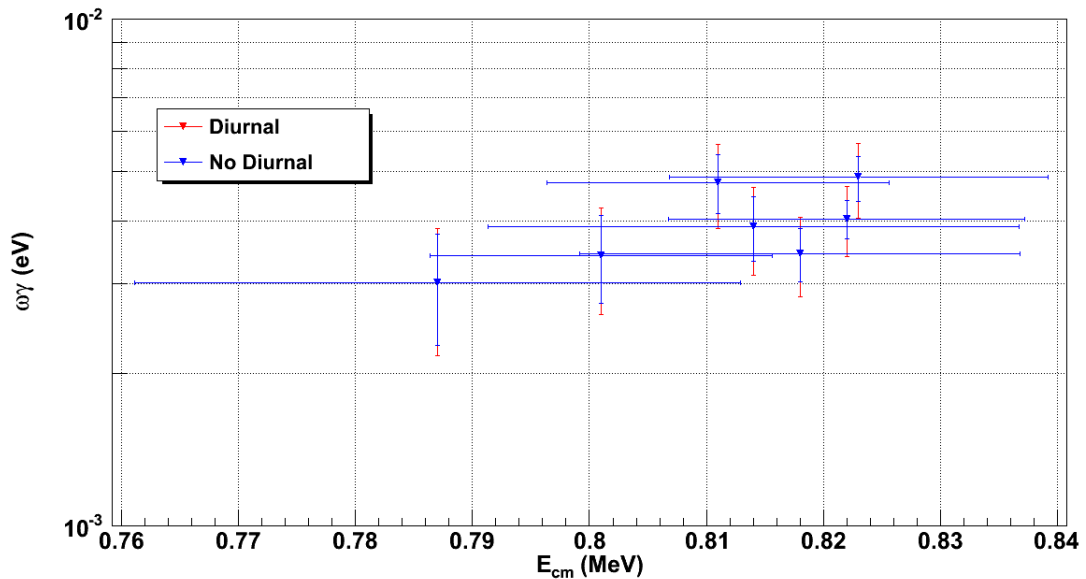


Figure 5.23: The cluster of $\omega\gamma$ measurements as a function of energy for the ~ 0.8 MeV peak with and without the possible effect of external temperature variation.

5.4.2 External Temperature Investigation

During the analysis stages, it was found that the results in the $E_{cm} \sim 0.8$ MeV peak were not behaving as expected. As these 6 on-resonance measurements were repeated readings of the same resonance, the calculated cross-sections, S-factors or $\omega\gamma$ s should all lie within error of each other. Instead, as can be seen in Figure 5.23, although they might be described as “close” (by-eye), that is not the same as being within experimental uncertainty. The presence of some further systematic effect seems plausible.

As the only variable not explicitly entered into the calculation the temperature of the target gas seemed a plausible area to be investigated. A preliminary study into the time each energy was run over presented a mild diurnal effect, whereby the measurements returning a lower result had been performed overnight. Furthermore, with the experiments performed during May/June and then November, there remained a possibility that a small but noticeable effect was caused by ambient temperature.

The results of this study are depicted in Figure 5.24 where it is clear that within the summer experiment there was an external temperature variation of ~ 8 K. Furthermore, the temperature is even lower once the November data is included, a maximum discrepancy of ~ 18 K becomes apparent. Table 5.6 reconsiders the effect of temperature upon the number of target nuclei, what could be the upper limit of a temperature induced uncertainty?

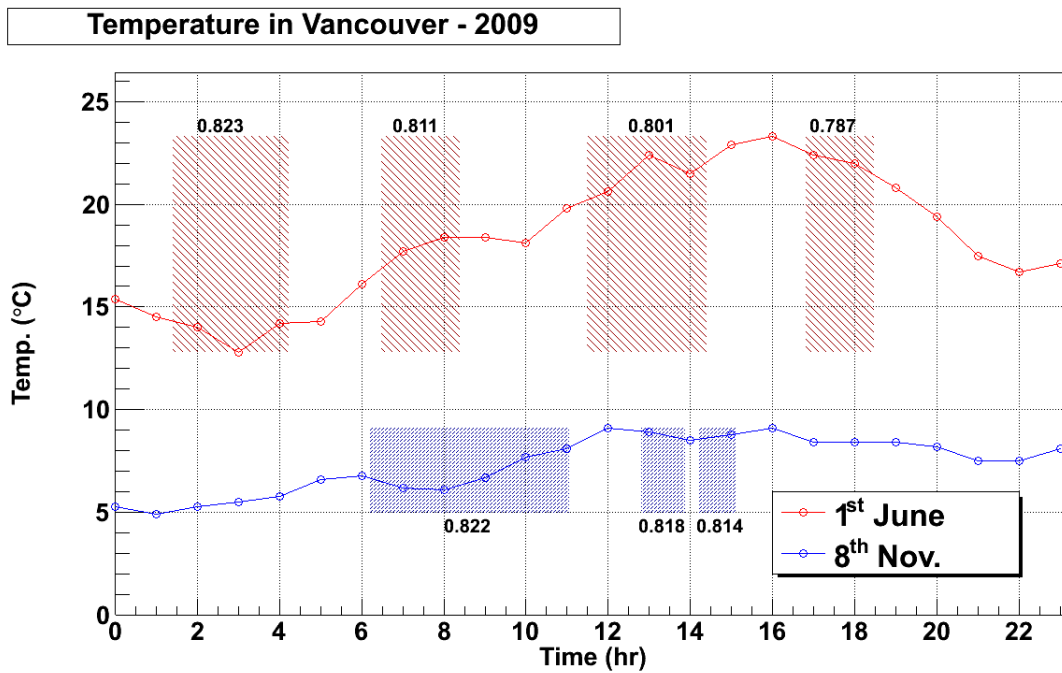


Figure 5.24: External temperature variation for the days in question when measurements were taken of the $E_r = 806$ keV peak. Hatched boxes, of the corresponding colour, show the time period for which each centre-of-mass energy was recorded. It is clear that, for example, the $E_{cm} = 801$ keV measurement was taken at a temperature several degrees above that of the $E_{cm} = 811$ keV point. Data taken from [97].

Temperature (K)	10^{18} atoms/unit area (cm^{-2})		
	4 Torr	4.5 Torr	5 Torr
280	1.697	1.909	2.121
290	1.638	1.843	2.048
300	1.584	1.782	1.980
310	1.533	1.724	1.916
320	1.485	1.670	1.856

Table 5.6: Effect of temperature variation at different pressures on the number of target nuclei. In this case the uncertainties will be the same as those presented in Table 5.4, $\sim 3.7\%$.

It is clear that the answer is “not very much”. Even accounting for the extreme worst case scenario that the effect of the Vancouver climate is to introduce a 20K variation in target temperature, this only produces an additional $\sim 7\%$ error. But this assumes that there is only one data set, where in fact we have two separate experiments. The ambient temperature variation for the two separate runs varied by no more than $\sim 8\text{K}$, which corresponds to an uncertainty $< 3\%$.

5.5 Determination of Astrophysical Reaction Properties

With the knowledge of the three terms; yield, incident nuclei and target nuclei, useful astrophysical quantities may be determined, namely the probability of that interaction, or cross section.

5.5.1 Cross Section and S-factor

The value of the cross section was determined through the application of Equation 3.5, which has been thoroughly discussed in Chapter 3. The processes required to establish the component terms: yield, target nuclei and incident ions, have been discussed within this chapter, the values of which are presented for completeness in Appendix A.

Likewise, the determination of the astrophysical S-factor simply takes one further step along the yellow brick road of calculation, and applies Equation 3.6 to those previously established cross sections. All the required data and formulae to repeat these calculations are found within this work, should one wish to do so.

5.5.2 Error Analysis

The majority of the error analysis was performed using standard Gaussian statistics common to any experimental analysis. For completeness the error propagation shall be discussed here. The uncertainty on the final result was found by combining individual errors in quadrature in the standard way through:

$$\frac{\delta f}{f} = \sqrt{\sum \left(\frac{\delta x_i}{x_i}\right)^2}, \quad (5.12)$$

in which a function, f , with error δf , describes a series of independent variables, x_i , with their own independent errors, δx_i [98, 99]. These are also explicitly stated within Appendix A.

The exception to this came where statistics were insufficient and so a low-statistic method was required instead. Following the Feldman & Cousins techniques established in [100] those energies with the lowest yields ($E_{cm} = 0.621 - 0.717$) were calculated with a 1σ confidence interval.

According to the central limit theorem the distribution of random variable becomes Gaussian as $N \rightarrow \infty$, for which all the standard error techniques apply. However, for a much smaller value of N this is not the case. In fact, it can be shown that once N reaches ~ 20 , the distribution becomes anti-symmetric, and thus the previously described treatment is no longer appropriate. Instead, the practice is to make use of confidence intervals which take account of this small-number discrepancy, and the condition that any number must be non-negative. As already mentioned, this work uses the Feldman & Cousins [100] technique, as opposed to more traditional methods of former confidence belts.

The benefit of the Feldman & Cousins technique over the alternative Neyman confidence intervals [101] is that the previously unrecognised problem of “empty intervals”, where the interval contains no physically allowed values is accounted for. It should be noted that for expected mean values of $\mu > 1.65$ the two techniques converge, a full and detailed description can be found in [102].

In a few cases where repeated measurements of the same resonance had been recorded, a weighted mean was taken in order to further constrain the uncertainty. The weighted mean, \bar{x} , and its variance, $V(\bar{x})$, are given by:

$$\bar{x} = \frac{\sum x_i/\sigma_i^2}{\sum 1/\sigma_i^2} \quad (5.13)$$

and

$$V(\bar{x}) = \frac{1}{\sum \frac{1}{\sigma_i^2}}. \quad (5.14)$$

5.5.2.1 The Absent Recoils

Not all energies measured during the course of the experiment had ^{21}Ne recoils observed. This then raises the question of how a yield of zero events can be processed through the appropriate formulae? Naïvely, one might simply use a value of 1 recoil for the raw yield, however, this entirely misses the point of the Poisson nature of counting statistics.

Instead, as with the other low-stat measurements (zero being the lowest of all counting measurements) the Feldman & Cousins technique was implemented. The same confidence intervals used previously are taken down to a lower limit of $n = 0$ and $b = 0$ (where n is the number of events and b the number of background events). The raw yields used in the calculation of cross sections etc. for runs where no recoils were observed were taken from the relevant tables presented in [100]. Obviously the rest of the analysis: target, beam etc. proceeded as with other runs.

Chapter 6

Results and Interpretation

“No dragon can resist the fascination of riddling talk and of wasting time trying to understand it.”

- J.R.R. Tolkien

6.1 The $^{17}\text{O}(\alpha,\gamma)^{21}\text{Ne}$ Cross Section

The analysis can be said to have been concluded with the determination of the cross section of the reaction, the probability of interaction between the two nuclei. Using the techniques discussed in the preceding chapter, the cross section at each energy has been determined and is presented here in Table 6.1 and as Figure 6.1. Also included in the appendix are the data used to obtain these cross sections.

Due to the large coverage afforded by the DRAGON energy “bite”, and the desire to perform a sufficient scan across important energy regions, several measurements at different centre of mass energies are in fact measuring the same resonance (or region). This is most obvious when examining the cluster of data points at $E_{cm} \sim 0.8$ MeV. This cluster, corresponding to the series of measurements of the 8.154 MeV state in ^{21}Ne , can be seen in the close-up image inset into Figure 6.1. Clearly visible are the overlapping regions which can be used to resolve the position and width of the resonance. Also, for the second experimental run performed in November 2009, certain energy regions were repeated to provide a self-consistency check, namely $E_{cm} \sim 1.16, 0.8$ and 0.71 MeV. As a result, the 0.8 MeV cluster can be combined into a weighted average to provide a single value for the resonance having been measured multiple times. For the lowest repeated point, only an upper limit can be established due to no ^{21}Ne recoils being detected. In this case it is not appropriate to calculate a weighted average. Certainly in the case of the two

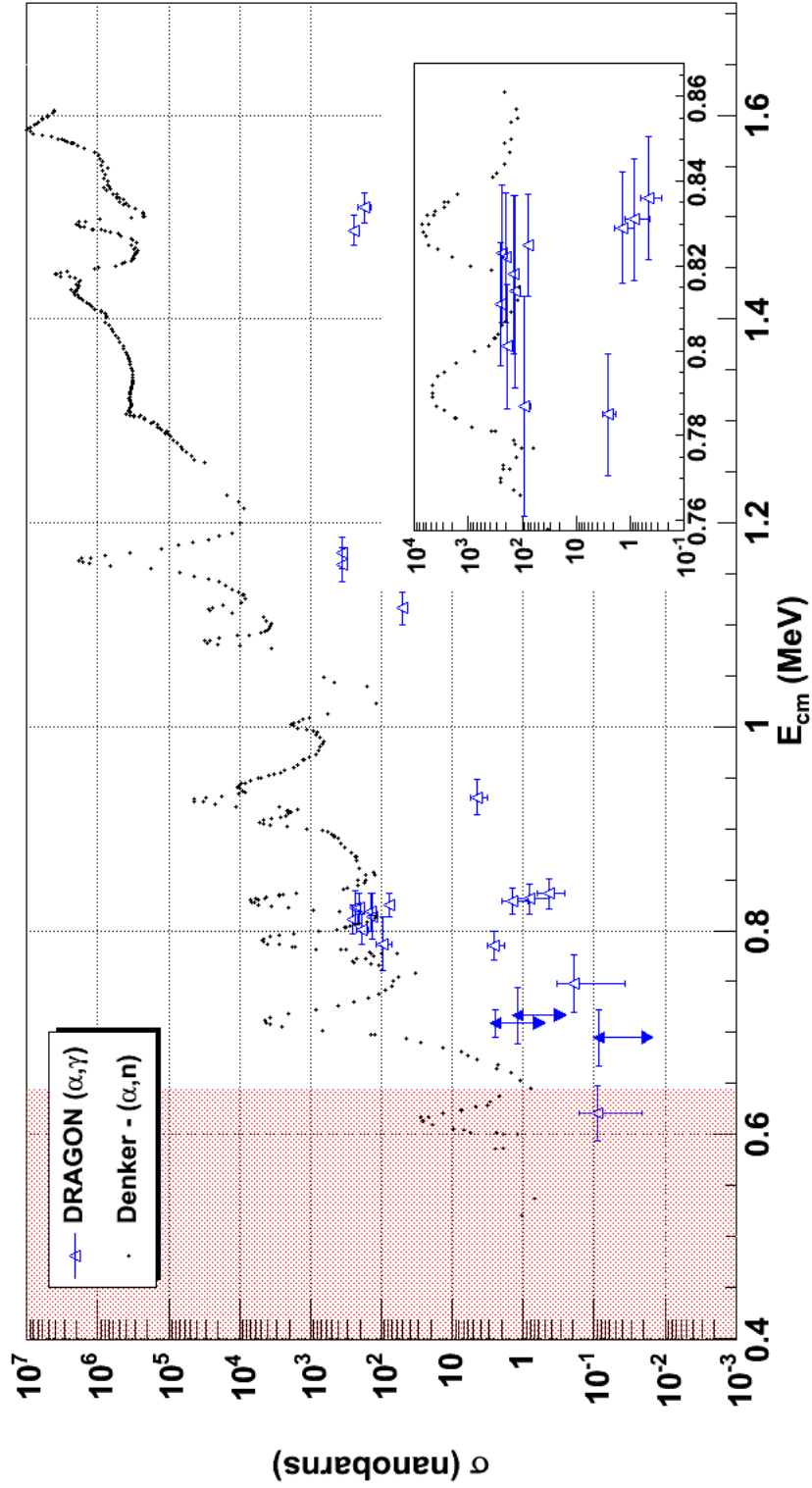


Figure 6.1: The $^{17}\text{O}(\alpha, \gamma)^{21}\text{Ne}$ cross section. The plot depicts the results of the experiment in blue: open triangles represent datapoints with recorded ^{21}Ne recoils and solid triangles and solid triangles where only an upper limit could be assigned. The data is also plotted with the $^{17}\text{O}(\alpha, n)^{20}\text{Ne}$ measurement by Denker [35], black points, for comparison, and overlaid with the Gamow window in red. The inset highlights the data taken at the region of unexpectedly high-yield around $E_{cm} \sim 0.8$ MeV.

E_{CoM} (MeV)	σ (nb)	$d\sigma$ (nb)	error (%)
0.621	0.0905*	0.0690	76.5
0.695	0.0691†	0.0193	27.1
0.709	1.90†	0.61	31.8
0.717	0.986†	0.276	28.0
0.748	0.190*	0.153	80.5
0.785	2.54	0.71	28.1
0.787	94.2	23.2	24.6
0.801	186	36	19.4
0.811	256	34	13.1
0.814	134	19	14.3
0.818	143	17	11.7
0.822	205	17	8.2
0.823	233	23	9.9
0.825	78.7	10.4	13.3
0.829	1.42*	0.57	40.6
0.831	0.827	0.402	47.9
0.836	0.442*	0.181	41.2
0.931	4.40	1.16	26.4
1.116	50.4	7.8	15.4
1.159	351	43	12.3
1.17	351	45	12.8
1.487	246	32	12.9
1.509	177	39	22.3

Table 6.1: Table of $^{17}\text{O}(\alpha,\gamma)^{21}\text{Ne}$ cross sections. *measurements requiring additional separator time-of-flight analysis; †null-event points, only an upper limit could be determined.

~ 0.7 MeV points where the bite of the higher 0.717 MeV point wholly encapsulates the coverage of the 0.709 MeV measurement, this provides no new information. The 0.717 MeV measurement, with ~ 4 times the run duration, shows a significantly lower limit than the 0.709 MeV measurement. Therefore the 0.717 MeV is taken as the more precise measurement of the 8.062 MeV resonance.

6.2 Extrapolating the Astrophysical S-factor

The cross section is not always the most straightforward term with which to interpret results. This is particularly true in the field of nuclear astrophysics where we are concerned with the reaction mechanism at the extremely low energies at which stellar burning occurs. The region of the Gamow window is shown in the cross section plot, Figure 6.1, and can clearly be seen to extend far below the region covered experimentally. The cross

section tails off strongly with decreasing energy making accurate, statistically significant, measurements difficult to obtain. Furthermore, in the absence of data taken in the energy region of interest, one is required to make an extrapolation down towards the Gamow window. The strong energy variation reduces the reliability of this extrapolation and the situation becomes more problematic by introducing greater uncertainties. Something the experimental campaign was proposed to reduce.

The standard practice, therefore, is to make use of the astrophysical S-factor which has already been discussed in Chapter 3. The flattening of the excitation function makes it far more stable with varying energy. For a non-resonant, or flat, excitation function the smoothly varying function of beam energy becomes a useful tool in the extrapolation.

This result can be seen in both the example functions taken from [14] in Figure 3.1 and by comparing the work of this thesis in Figures 6.1 and 6.2. The “flattening” of the function in the S-factor plot is quite apparent, and the benefit it accords to lower-energy extrapolation should be clear. The S-factor calculated by the Descouvemont model is also included. The DRAGON measurements result in a far stronger (α,γ) channel than predicted by the GCM calculations. This is most noticeable when comparing the off-resonance points around $E_{cm} \sim 0.8$ MeV where the GCM underpredicts by a factor of ~ 100 to the experimental data.

6.3 The Strength of the Resonance

Through calculating the resonance strength, $\omega\gamma$, it is possible to compare contributions to the reaction rate from different portions of the excitation function. It also removes the issue discussed earlier of the over-estimation of target nuclei (and therefore underestimation of σ) as Equation 3.24 makes use of the “stopping cross section”, ϵ , and the target number density (in units of atoms per cubic centimeter) rather than the total number of interacting nuclei as one might otherwise expect.

Values for the $\omega\gamma$ were calculated for each data point; however, a resonance strength is not always the best, or most appropriate parameter to determine. Obviously for off-resonance regions where σ varies smoothly with respect to energy, it makes no sense to talk about a resonance strength. During the experimental campaign, the energies measured were selected based on known state information of ^{21}Ne and resonances observed in the (α,n) channel [35]. This was in part to ensure the validity of the $\omega\gamma$ technique, but more importantly to maximise any potential yield at the lowest energy regions. However, the presence of a resonance in the (α,n) channel is no guarantee that a similar resonance will be present in the corresponding (α,γ) channel.

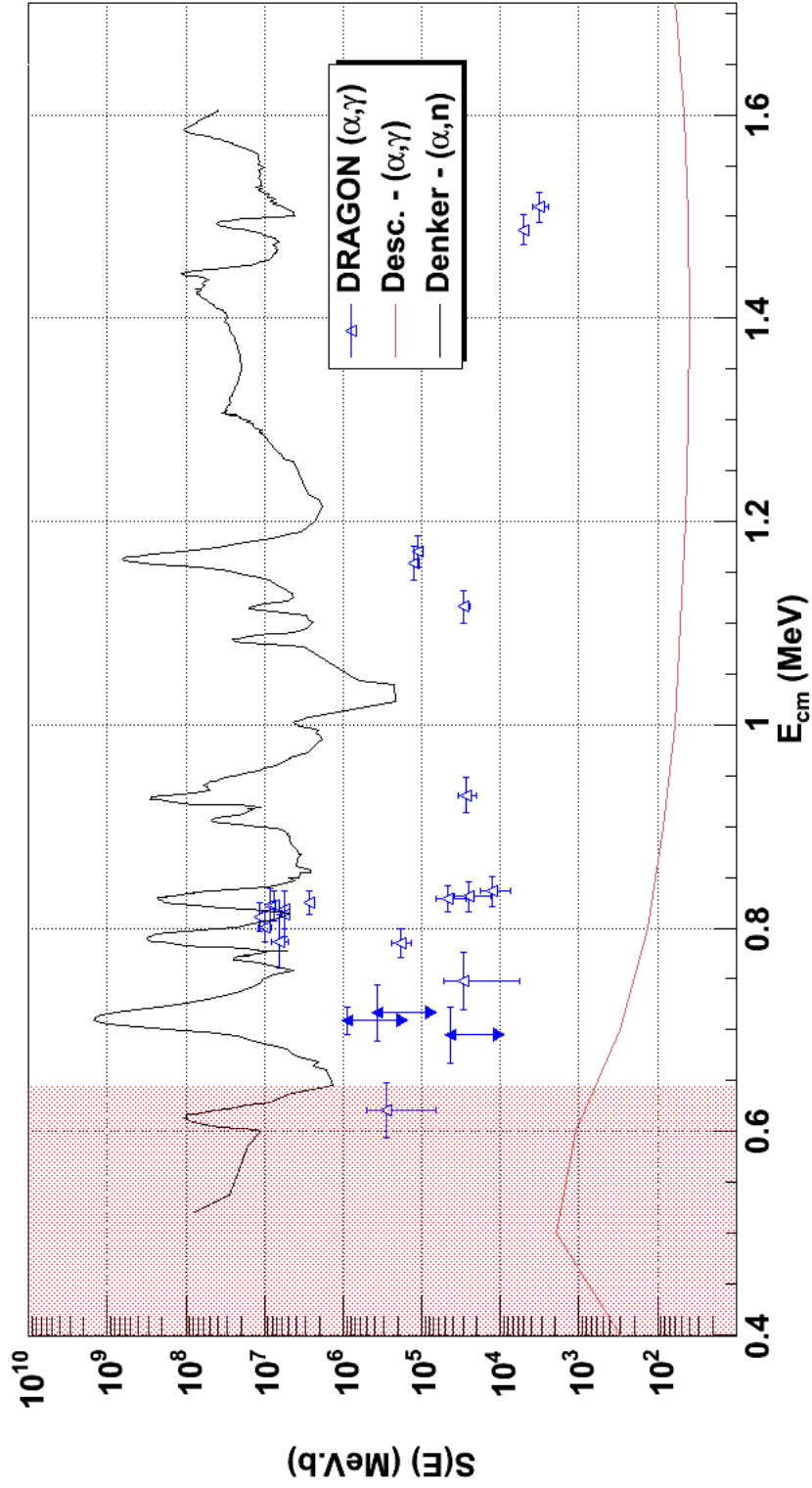


Figure 6.2: The experimental results converted into astrophysical S-factor. Shown are the $^{17}\text{O}(\alpha, \gamma)^{21}\text{Ne}$ DRAGON measurements (blue triangles, solid points indicating upper limits), the Descouvement GCM (α, γ) calculation (red line) for the ground state [43], and the Denker (α, n) data as the black line [35]. The data are overlaid with the Gamow window as the shaded red region.

In order to confirm the existence of a resonance, a full scan of the excitation function around the resonance energy, E_r , is necessary. This was performed for the region around the 8.154 MeV state, corresponding to the $E_{cm} \sim 0.8$ MeV cluster, but other data points, e.g. $E_{cm} \sim 0.621, 0.71, 1.16$ & 1.59 MeV, can be labelled no more than “likely candidates” without further information.

Nevertheless, the results of the resonance strength calculations are shown in Figure 6.3. However, whereas the calculations and results for each measurement of the cross section and S-factor were displayed previously, it seems more appropriate to speak only of resonances and so the weighted averages are taken and displayed instead.

6.3.1 $E_{cm}^r = 806$ keV

Due to the full coverage of the energy region around the $E_{cm} \sim 0.8$ MeV resonance it was possible to assign a more constrained value to the resonance energy, as opposed to the usual energy bite of DRAGON of $24.0 < \Delta E_{cm} < 56.1$ keV (for a target pressure of 3 Torr and 8 Torr respectively). The scan of this peak covered an energy region starting at $E_{cm} = 851$ keV (the upper boundary of the 836 keV data point) and pushed down with continuous coverage to $E_{cm} = 668$ keV (the lowest energy in the 695 keV bite), which can be seen on Figure 3.6 as the energy “bite”. This provided several off-resonance measurements from which we could deduce the energy.

Using the off-resonance energies at $E_{cm} = 0.785, 0.787, 0.825, 0.829, 0.831$ and 0.836 MeV, specifically their respective “bites” coupled with information from the BGO spectra in Figure 6.4 it was possible to determine that a resonance was located between $0.799 < E_{cm} < 0.816$ MeV. The z-distribution of γ -ray events in the BGO array is shown in Figure 6.4 where the movement of the resonance position within the target is apparent. Both spectra display a measurement of the $E_{cm} \sim 0.8$ MeV resonance made during the November pressure variation scan. In this case, the pressure was varied to observe the effect of different energy bites for the same incident beam energy. It is clear that the $E_{cm} = 0.814$ MeV measurement contains the resonance at near-centre within the target, compared to the $E_{cm} = 0.825$ MeV run with the resonance position weighted heavily downstream. This would have the effect of increasing the separator transmission due to the reactions occurring toward the target exit, which was discussed in Section 5.2.3.1.

By examining Figure 6.5 the portions of the excitation function that were scanned by different measurements can be compared. This is most easily explained by looking at the pressure variation points, i.e. those with the same incident beam energy but with different energy bites ($E_{cm} = 0.814, 0.818, 0.822$ & 0.825 MeV). In this example the

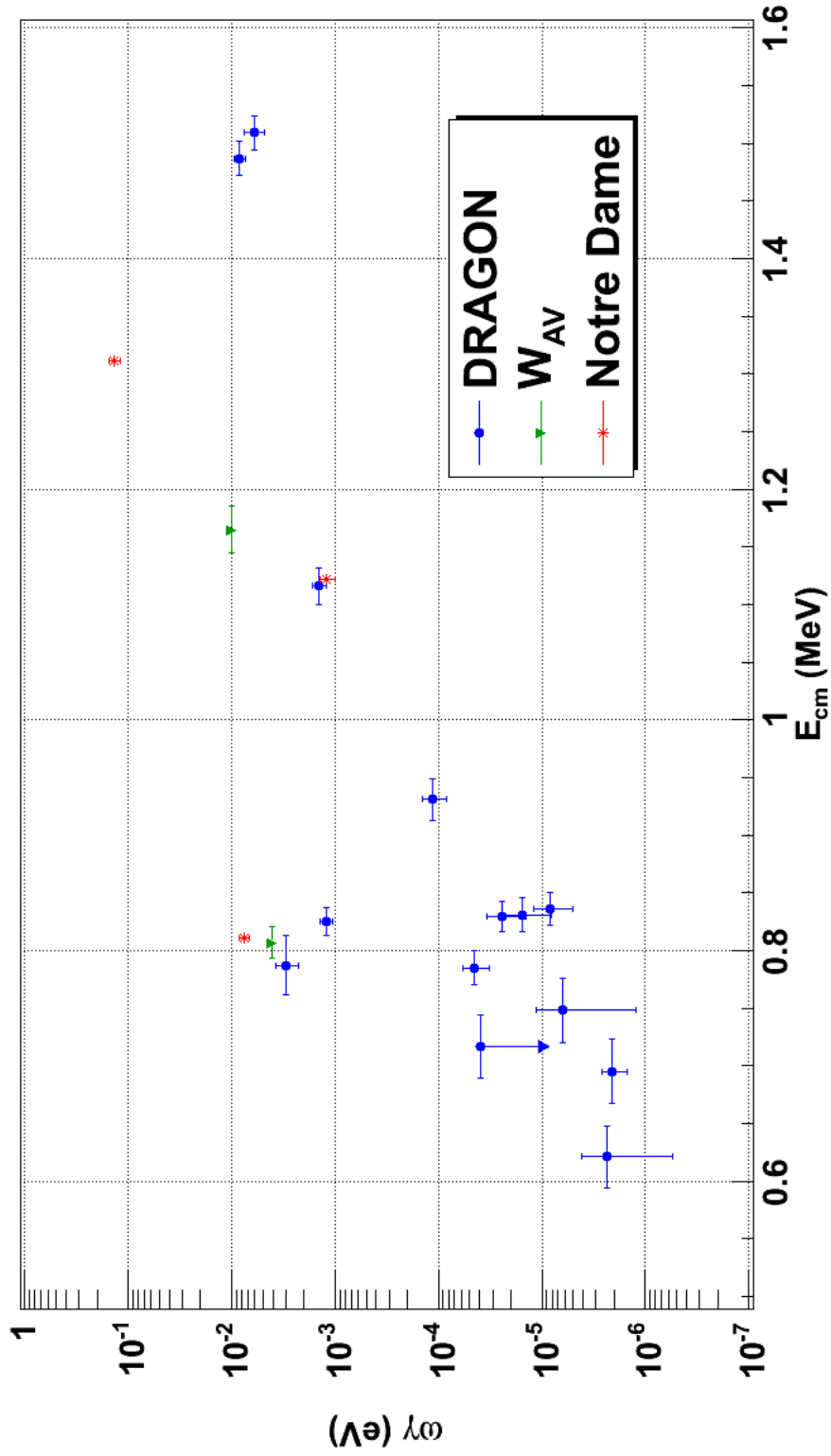


Figure 6.3: The resonance strengths for the $^{17}\text{O}(\alpha, \gamma)^{21}\text{Ne}$ reaction. Blue datapoints are the individual DRAGON measurements, with the published Notre Dame [93] values depicted in red. For those energies where repeated measurements were taken, a weighted average, W_{AV} , as described in Section 5.5.2, has been used in place of the DRAGON datapoints and is depicted in green.

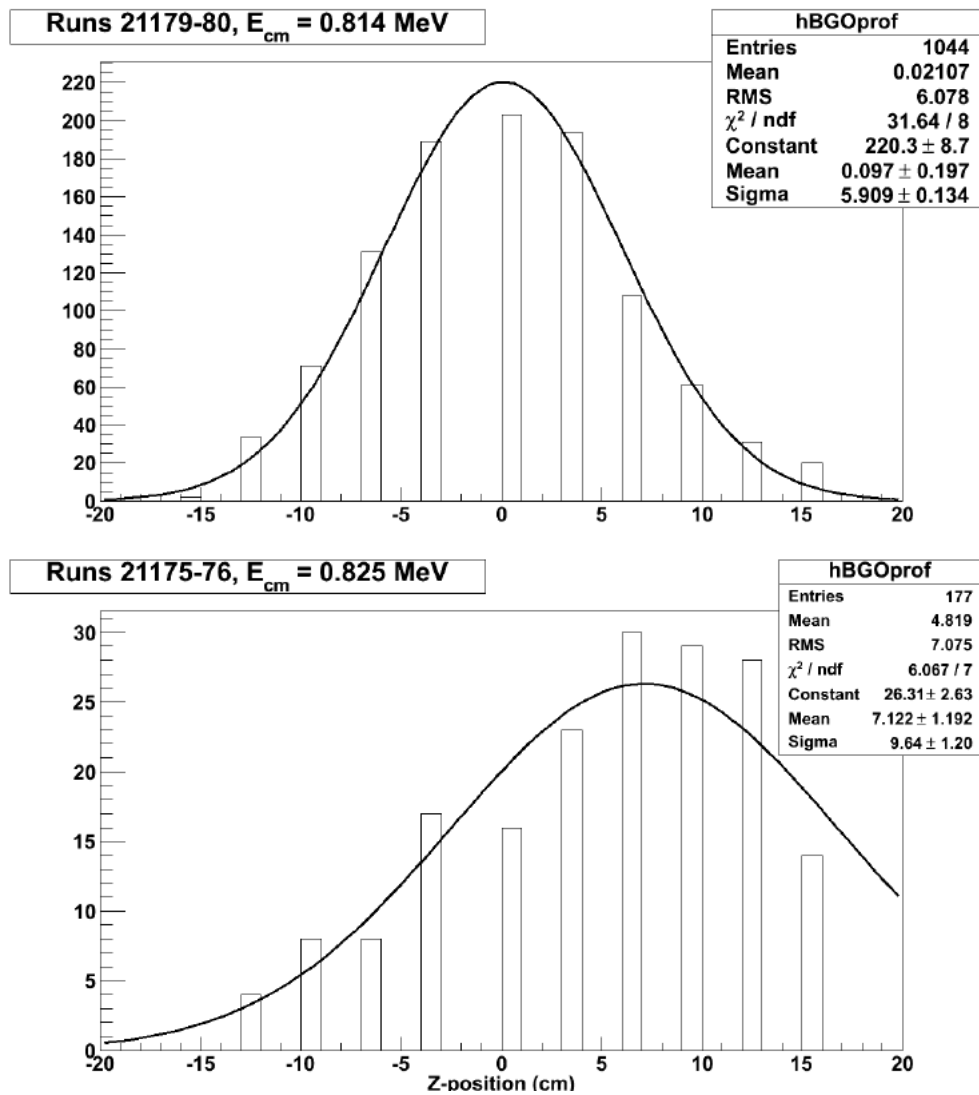


Figure 6.4: BGO z -distributions for $E_{cm} = 0.814$ & 0.825 MeV. Both measurements are of the same resonance, but the BGO γ hit pattern can be used to show where the resonance is located within the gas target. By also knowing the entrance and exit energies, as well as the target energy loss, the energy of the resonance can be determined.

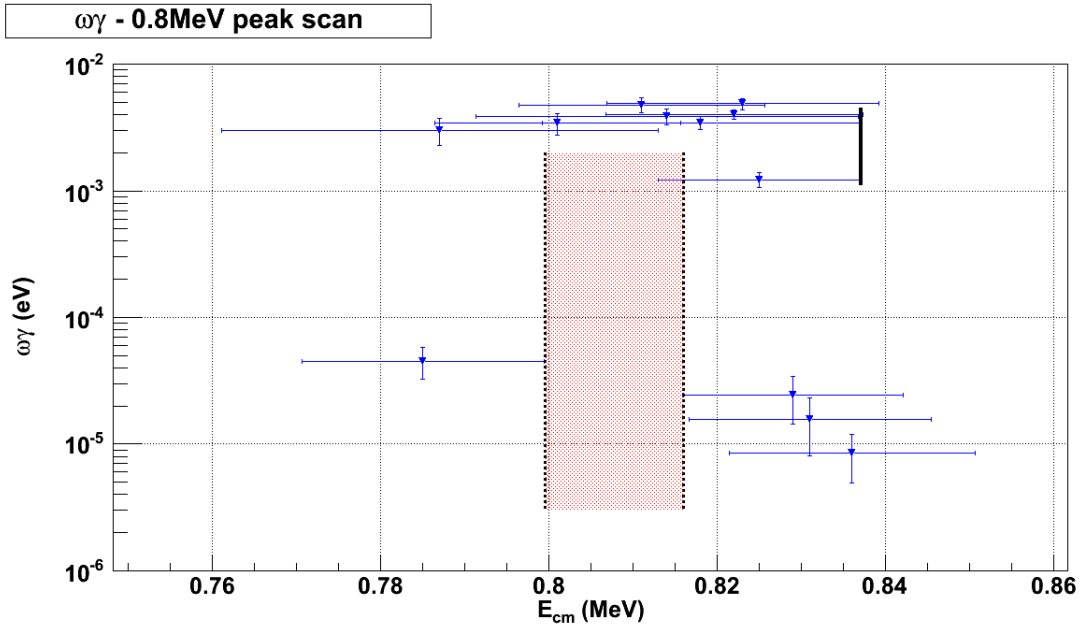


Figure 6.5: Assignment of the ~ 0.8 MeV resonance via energy bite variation. The red area is the energy region where the resonance has been determined to lie. The black line marks the energy at the entrance to the gas target for the four pressure variation runs, $E_{cm} = 0.814, 0.818, 0.822$ & 0.825 MeV.

lowest resonance strength was measured at the $E_{cm} = 0.825$ MeV point with the other readings ~ 3 times greater. This would be indicative of a resonance occurring below the lowest point of the 0.825 energy bite with possibly some of the tail encroaching on the energy sampled by the DRAGON target. Furthermore, there are the solid non-resonance points at $E_{cm} = 0.785$ & 0.829 MeV which can be used to impose a boundary on where the resonance must lie. This value corresponds well with the known state at $E_{res} = 8.154$ MeV and is in good agreement with references [55, 93].

The BGO array’s modular structure allows for some position information to be determined. By examining the hit pattern in the full γ -ray array it is possible to locate the resonance within the gas target energy “bite” to within a resolution of a few centimetres, the size of the BGO prism. This is only applicable for coincident measurements of high statistics, firstly to account for the BGO efficiency, and secondly to allow faint structure to be observed. This is apparent in Figure 6.4 where the resonance can be seen to be downstream of the target centre. This would correspond to a value of $E_{res} \sim 8.154$ MeV.

6.3.2 Selection of Likely Resonances

Without a sufficiently detailed level scheme or data covering the full excitation function it becomes difficult to assign the status of “resonance” to an energy. In this data the exception remains the $E_{cm} \sim 0.8$ MeV region for which a more idealised scan was performed, and thus, as was described in the previous section, it can be declared, with no small amount of confidence, that there exists a resonance in the $^{17}\text{O}(\alpha,\gamma)^{21}\text{Ne}$ channel at $E_{cm} = 0.806$ MeV.

However, as has already been covered earlier in this thesis, there is a significant amount of data that suggests other resonances are present within the studied energy range. Namely, these would be the $^{17}\text{O}(\alpha,n)$ measurements described in Chapter 2, the work of [35–37]. Although these data are describing the competing reaction channel to that which is of interest in this thesis, in the absence of other $^{17}\text{O}(\alpha,\gamma)$ data this assumption must suffice. Further measurements allowing a confirmation of these assumptions were performed by another group, and are described in detail towards the end of this chapter, in Section 6.6.

For the purposes of the final analysis, it was necessary to make decisions on which datapoints would be processed as resonant contributions, and which would comprise the non-resonant dataset. The decision on whether a datapoint was labelled as a resonance was based on the previously mentioned evidence, using known resonances in the competing $^{17}\text{O}(\alpha,n)$ channel. Those measurements meeting the requirements are listed in Table 6.2 along with their calculated resonance strengths and the associated uncertainty.

E_{CoM} (MeV)	run numbers	$\omega\gamma$ (meV)	error (%)
0.621	21258-338	0.714	28.1
0.717	20159-68	23.16	24.6
0.806	20146-53, 21168-80	3	19.4
1.116	20052-56	33.56	13.1

Table 6.2: The resonances selected for the purposes of calculating the reaction rate according to Equation 3.26.

6.4 Thermonuclear Reaction Rates

The development of nucleosynthesis theory is heavily dependent upon continued improvement in the empirical measurements of stellar reaction rates [103]. This work will

attempt to make its own contribution to these compilations. Comparisons to the previous values, those of CF88 and Descouvemont [39, 43], are necessary and so those are included in all figures. Since the CF88 numbers are presented directly as reaction rates it was a trivial matter to include them. The Descouvemont GCM results required a minor calculation in order to convert the presented S-factor into a reaction rate. The Descouvemont S-factors were processed through the same reaction rate code used to calculate the DRAGON results.

6.4.1 Resonant Contribution

In Chapter 3 it was discussed that it is possible to calculate the individual contribution to the reaction rate from a narrow, isolated resonance. Using Equation 3.26 these calculations were performed for each assumed resonance, those listed in Table 6.2. How a state contributes to the reaction rate in the Gamow window will depend on many factors, including spin and parity, width of the channel and resonance energy.

The results of these reaction rate calculations are displayed in Figure 6.6 and the relative contributions can be compared to those of CF88 and Descouvemont. It is clearly shown that the Gamow window for $^{17}\text{O}(\alpha,\gamma)$ in massive stars occurs at $\Delta E_G \sim 200 - 300 T_6$ [28]. At this temperature region most of the resonances measured by DRAGON will have a negligible effect upon the total reaction rate. This highlights the deficiency in the $\omega\gamma$ technique. By following the guidelines in [14, 46], as described previously, the assumption is made that the only contribution to the reaction rate comes from the isolated, narrow resonances for which an $\omega\gamma$ is calculated. This may be a valid argument, after all, considering Figure 6.3, the highest strength at an energy approaching the Gamow window occurs at $\omega\gamma_{8154} = 4 \pm 0.2$ meV, compared to its direct off-resonance points at $E_{cm} = 0.829 - 0.836$ MeV where the effective resonance strength is some 2 orders of magnitude lower.

However, “2 orders of magnitude lower” is quite different from zero, which is what the sum of $\omega\gamma$ s implies. The technique described by Equation 3.26 makes the assumption that the cross section is zero for all off-resonance regions, which has already been shown to be inaccurate in Figure 6.3. However, in the absence of more data, the approximation that the reaction rate comes solely from the cross section for these discrete resonances and is zero for all other energies is fair but possibly naïve. Certainly the resonance contribution to the reaction rate will be more significant than its adjacent off-resonance component, but this should be accounted for.

Naturally, it is not appropriate for the repeated measurements to be included in this summation. The 0.8 MeV cluster, the low energy (~ 0.7 MeV) limits and the ~ 1.17 MeV

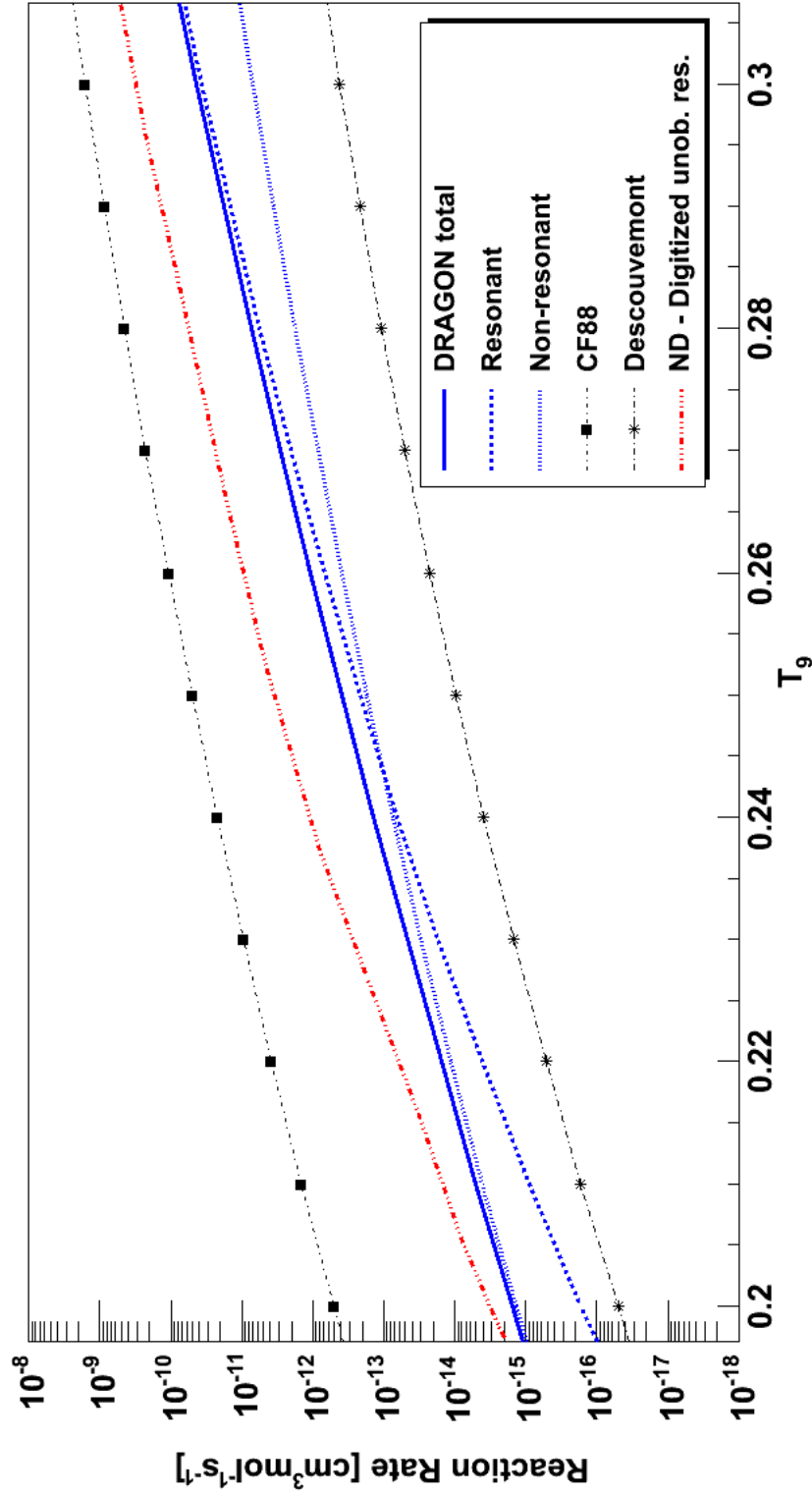


Figure 6.6: The $^{17}\text{O}(\alpha, \gamma)^{21}\text{Ne}$ reaction rates. The “corridor of uncertainty”, the CF88 and Descouvement predictions [39, 43], are shown in black. Within the range of these predictions are the DRAGON data in blue, and the measurement by Notre Dame [93] in red. The DRAGON data comprises three separate reaction rates: the resonant contribution described in Section 6.4.2. Finally, the third blue line (solid) is the sum of the resonant and non-resonant contributions.

normalisation between the May and November experiments are all measurements of the same resonances, obviously these can only contribute once regardless of the number of measurements performed. In these cases, it was the average for the resonance that was used to determine the contribution to the reaction rate.

6.4.2 Numerical Integration of the S-factor Excitation Function

Ideally, a full scan of the entire excitation function down to the lowest edge of the Gamow window would have been performed, and then the reaction rate could be determined directly by a full numerical integration as described by Equation 3.15. Obviously this was not possible due to those reasons already discussed throughout this work. Alternatively, one can effectively fill in the intervening space via fitting a first-order polynomial to the existing data then extracting the S-factor at these points.

This technique would produce a relatively flat cross section across the function with few features of note. Certainly, this does not appear wholly appropriate since it is clear that there is an extremely prominent feature at $E_{cm} = 806$ keV, one which possibly supercedes the otherwise dominant (α, n) channel. Instead, a combination method seemed the most promising. Fitting to known off-resonance data while still considering the contribution of $\omega\gamma$ s separately allows for the calculation of the non-resonant contribution to the reaction rate.

In the same way that individual contributions of isolated resonances can simply be summed together [14], as per Equation 3.26, one can apply the same treatment to the non-resonant reaction rate too. Since the resonances have S-factors many orders of magnitude greater than even the most optimistic fit, any induced error from a double count over the resonance widths is negligible. Taking the solid example of the ~ 0.8 MeV resonance, the peak at 7.12×10^6 MeV.b is ~ 500 times greater than the S-factor at $E_{cm} = 0.836$ MeV. The off-resonant contribution equates to less than the uncertainty on the weighted average of the peak.

In this instance the counter argument to that used when considering the $\omega\gamma$ contribution to the reaction rate must be applied, that only non-resonant data points should be taken into account. Obviously, including the measurements of the ~ 0.806 MeV peak, and other likely resonances, could significantly offset a fit to the DRAGON data. The effect would be to artificially increase the calculated reaction rate, as well as introducing a double counting uncertainty that has already been discounted due to the relative strength of respective contributions.

A range of fitting parameters were tested, as well as the effect of including those

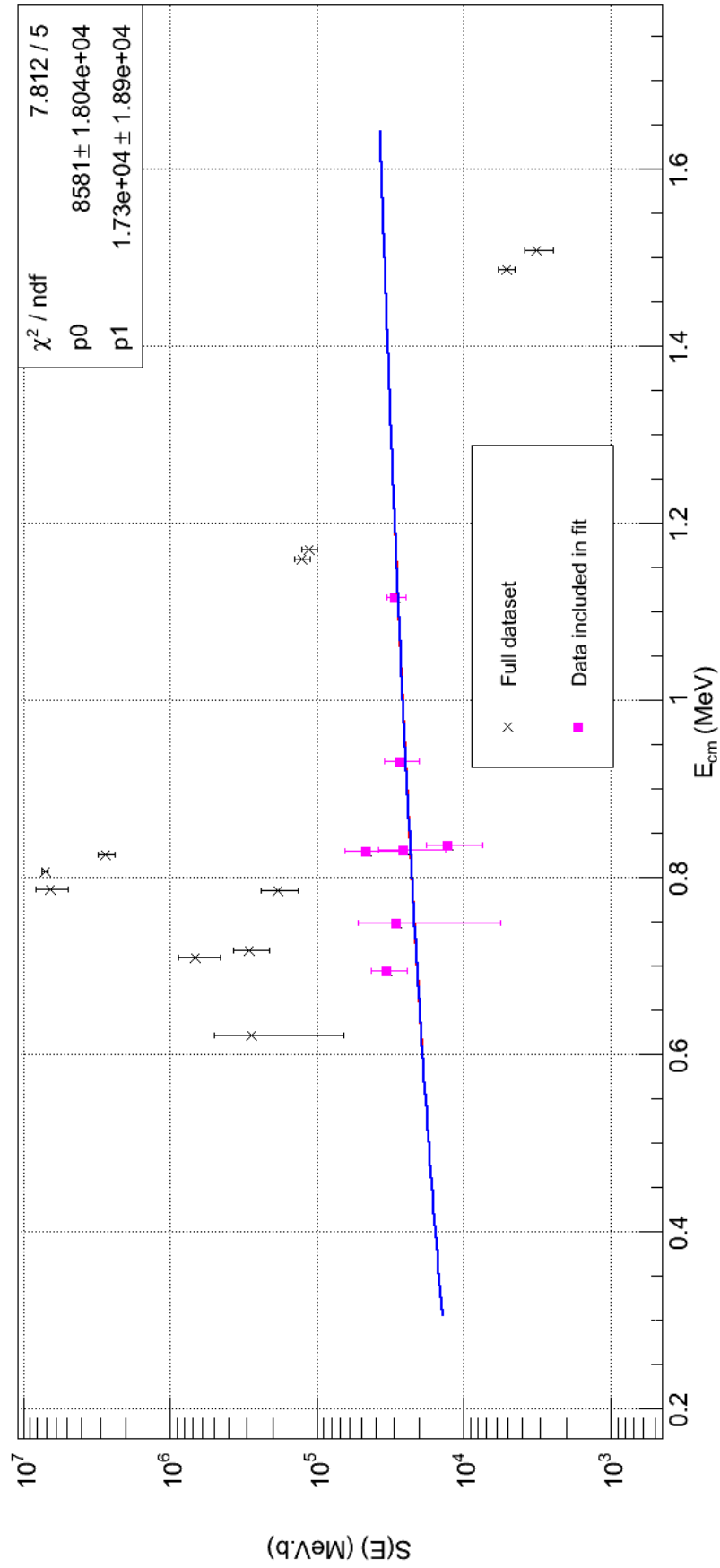


Figure 6.7: The fit to the non-resonant S-factors is displayed as the blue line. The fit (a simple first-order polynomial) was applied only to those datapoints thought unlikely to be due to resonances, the justification being the opposite of that described in Section 6.3.2. The datapoints included in the fit are highlighted in magenta. The remaining points (in black) are displayed for clarity, but have no influence upon the fitting process.

likely, but not certain, resonances described in Table 6.2. Figure 6.7 shows the DRAGON S-factor data with the best fit overlaid. The function (a simple first-order polynomial) is fitted to the cluster of off-resonance data at $E_{cm} \sim 0.8$ MeV, those that are certain to be non-resonant points, as well as the data gathered at 0.695, 0.748 and 0.931 MeV. This was then extrapolated to fill the full excitation function before being processed through a FORTRAN reaction rate code [104]. The results of these reaction rate calculations can be seen in Figure 6.9 as well as in Appendix A where two additional “pseudo-fits” providing a band of upper and lower limits are also shown.

6.4.3 Parameterisation of the Reaction Rate

Once the thermonuclear reaction rate has been determined, standard practice is to find an analytical approximation, a function that can later be used to reproduce the rate for astrophysical model calculations. This was performed by taking the final result of Figure 6.6, the total DRAGON reaction rate produced by summing the resonant and non-resonant contributions, and then fitting some function to the data.

In performing the parameterisation, it was found that the ROOT fitting algorithm could not sufficiently deal with the magnitudes required, with reaction rates lower than 1×10^{-16} for $T_9 < 0.2$, so an alternative was sought. This issue was overcome by plotting the logarithm of both the reaction rate and temperature, as given by:

$$\log(N_A \langle \sigma v \rangle) = r, \quad (6.1)$$

and fitting to that. The best fitting function, the one that most closely matched the data, whilst showing limited deviation at the extremes, was found to be a 6th-order polynomial.

Parameter	Value	
χ^2	11.343	
NDF	1251	
p0	-1.94	0.008
p1	10.15	0.02
p2	-9.86	0.04
p3	2.14	0.06
p4	2.64	0.05
p5	0.48	0.03
p6	-1.67	0.02

Table 6.3: Analytical approximation for the DRAGON reaction rate.

The parameters, and function, are presented here as:

$$r = \sum_{i=0}^6 p_i (\log T_9)^i \quad (6.2)$$

and Table 6.3. In fitting with the standard format of the NACRE collaboration [34], the reaction rate for specific temperatures has been extracted and are given in Appendix A.

The covariance and correlation matrices of the parameterisation are presented in Tables 6.4 and 6.5 respectively. However, here it is necessary to give some discussion to what is truly represented by the parameterisation. It is not a fit in the most accurate sense of the term, the function applied to the data is really only ever likely to be a best guess. However, this approximation does allow for a reasonable reproduction of the data for the purposes of interpolating the values required by astrophysical codes.

	p0	p1	p2	p3	p4	p5	p6
p0	6.6e-05	-8.14e-05	-0.00024	0.00023	0.00023	-0.00012	-7.6e-05
p1	-8.1e-05	0.00055	8.9e-05	-0.0011	-0.00021	0.00055	0.00020
p2	-0.00024	8.88e-05	0.0020	-0.0013	-0.0021	0.00083	0.00067
p3	0.00023	-0.0011	-0.0013	0.0034	0.0016	-0.0019	-0.00089
p4	0.00023	-0.00021	-0.0021	0.0016	0.0025	-0.0011	-0.00087
p5	-0.00012	0.00055	0.00083	-0.0019	-0.0011	0.0011	0.00058
p6	-7.6e-05	0.00020	0.00067	-0.00089	-0.00087	0.00058	0.00037

Table 6.4: The covariance matrix for the parameterisation of the reaction rate.

	p0	p1	p2	p3	p4	p5	p6
p0	1	-0.43	-0.67	0.48	0.56	-0.43	-0.49
p1	-0.43	1	0.085	-0.82	-0.18	0.70	0.44
p2	-0.67	0.085	1	-0.49	-0.94	0.55	0.78
p3	0.48	-0.82	-0.49	1	0.57	-0.97	-0.80
p4	0.56	-0.18	-0.94	0.57	1	-0.67	-0.91
p5	-0.43	0.70	0.55	-0.97	-0.67	1	0.90
p6	-0.49	0.44	0.78	-0.80	-0.91	0.90	1

Table 6.5: The correlation matrix for the parameterisation of the reaction rate.

6.4.4 Summary of Reaction Rate Calculation

For further clarity, the analysis and calculation of the final reaction rate numbers are summarised here. For every measured energy, that is to say, each datapoint, a value for

both the resonance strength, and the cross section was calculated. For those clear resonances, those listed in Table 6.2, their contribution to the total reaction rate was determined through use of Equation 3.26 as detailed in Section 6.4.1. These datapoints were not used in the determination of the non-resonant contribution.

The non-resonant contribution was determined through an integration across the S-factor excitation function. The key point in this case is that the non-resonant, or “flat”, cross section was used. Where numbers for the cross section or S-factor have been presented, they are non-resonant. Where a resonant contribution is necessary, the resonance strength technique was utilised. This has previously been stated in Section 5.4.1.

6.5 Uncertainty of Results

The actual error calculations have already been discussed, earlier in Section 5.5.2 and more explicitly in Appendix A, however, some comment on their final value is necessary. It should be clear that the resonant contributions are more reliable than the non-resonant, simply due to the source of uncertainty. The extrapolation required to calculate the non-resonant contribution significantly increases the error on that value, whereas the resonant contributions are limited only by the uncertainty on the measurement.

However, the uncertainty on those measurements should also be discussed, specifically the relative contributions of each factor to the final error value and whether any one contribution dominates. The error budget for the experimental data is shown in Figure 6.8. It is quite clear that the most significant contribution (with the exception of the low-statistic or Feldman-Cousins derived [100] raw yield uncertainties) is that of the simulated separator transmission from Geant3. The raw yield uncertainties supercede the magnitude of those of the separator transmission for the datapoints with the lowest statistics, and were discussed thoroughly in Sections 5.5.2 and 5.5.2.1.

While the uncertainties on each value, be they cross section, S-factor, resonance strength or reaction rate, are large in some cases, it is important to consider what the question that was posed in the first place. The two competing models, CF88 [39] and the GCM [43], predict grossly different abundances so being able to introduce a further constraint is itself a useful outcome. Although the errors on the extrapolated cross section are large, the results obtained in this thesis are sufficient to provide a valuable constraint on this critical astrophysical reaction. A further off-resonance measurement at higher energies would help reduce the error in the extrapolation.

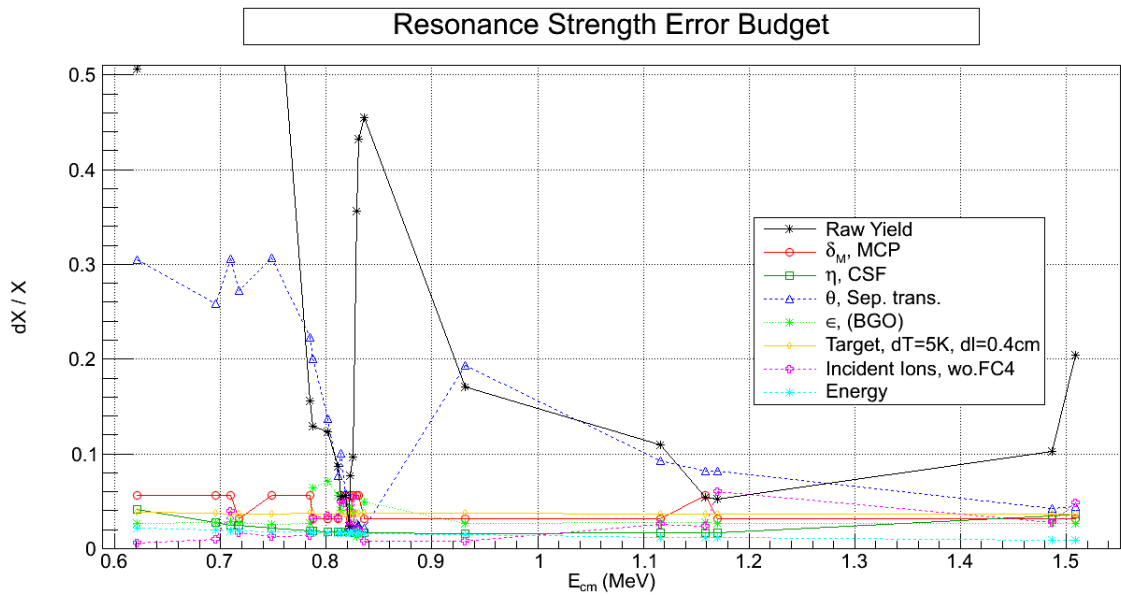


Figure 6.8: Fractional errors for the factors used to determine the resonance strength. Uncertainties on the MCP efficiencies, charge state fraction, separator transmission and BGO detector efficiencies are displayed for the factors of the adjusted yield, as well as those for the numbers of target nuclei and incident beam particles, and the error in the measured energy.

6.6 “Other” Data

After the DRAGON measurements had taken place a further experiment was performed by a group from the University of Notre Dame. Using a very different technique of a helium beam directed onto a tantalum-backed target implanted with enriched ^{17}O they covered a similar energy range although their results were limited to only the strongest resonances.

E_α (keV)	E_{cm} (MeV)	$\omega\gamma$ (meV)
1002(2)	0.811	7.6(9)
1386(2)	1.122	1.2(2)
1619(2)	1.311	136(17)

Table 6.6: The resonance strengths published by the Notre Dame group. The α -particle energies presented have been converted into the centre-of-mass for ease of comparison to those of the DRAGON collaboration [93].

The University of Notre Dame (ND) data was published in reference [93], listing comparable $\omega\gamma$ values to those measured by DRAGON for the $E_{cm} = 0.806$ MeV resonance. In order to acquire values for the ND results, two techniques were applied. The first simply extracted the data from the image presented in the above paper using a freely available piece of software, the Engauge Digitizer [105]. The alternate technique was to process the ND $\omega\gamma$ numbers through the same code used for the DRAGON data. The result showed consistency between these two extraction techniques, whereby the DRAGON code reproduced the ND reaction rates from their presented resonance strengths. Those calculated ND reaction rates are presented in Figures 6.6 and 6.9 to compare to the DRAGON results. Again, repeating the DRAGON technique, the same method of calculating a total reaction rate for a series of isolated narrow resonances was applied. Thus individual contributions from the resonance strength at $E_\alpha = 1002$, 1386 and 1619 keV, as well as a contribution from so-called “unobserved resonances” are calculated for the ND data before being summed to provide a total ND reaction rate.

The ND assignment of “unobserved resonances” introduces a deficiency in their data set, whereby they are confined to allocating only an upper limit. The DRAGON data significantly lowers this somewhat arbitrary limit and enables a more appropriate, and indeed accurate, value for the reaction rate to be determined at the energies of actual importance.

If Figure 6.9 is now closely examined, it is clear that for the region of astrophysical importance the Notre Dame reaction is dominated by the contribution from their “unobserved resonances”. At the upper boundary of the Gamow window the unobserved

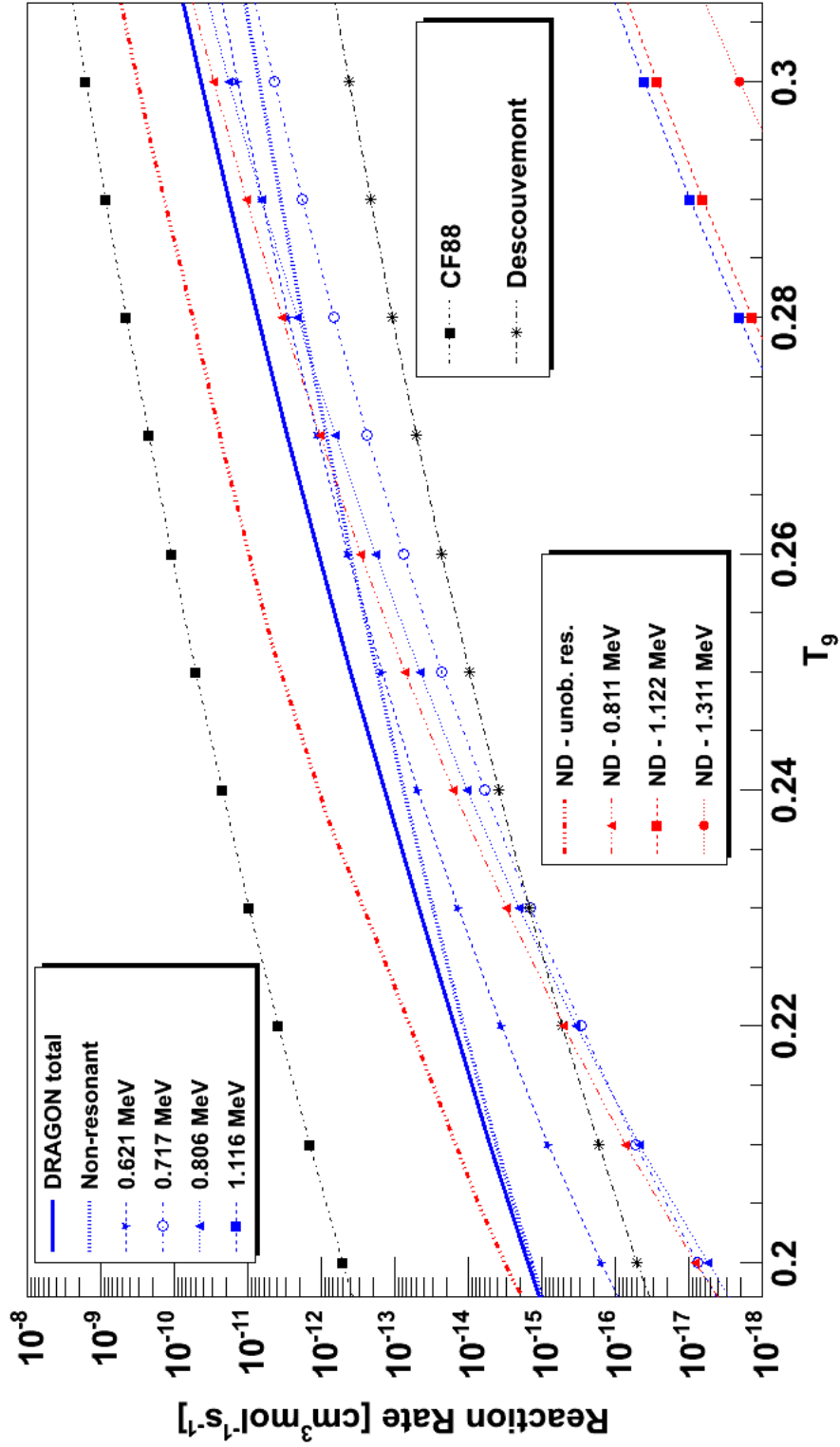


Figure 6.9: Comparison of the DRAGON and Notre Dame $^{17}\text{O}(\alpha,\gamma)^{21}\text{Ne}$ reaction rate contributions. The DRAGON results are displayed in blue, and the Notre Dame reaction rates are in red. For comparison, results of the two theoretical models are included as usual.

resonance contribution is an order of magnitude greater than their measurement of the $E_r = 8.154$ MeV resonance; this situation becomes even worse at the lower, $T_9 = 0.2$ boundary, where the contribution from the strong 8.154 MeV resonance drops significantly to less 1%. In this instance the upper resonances measured by the Notre Dame group can be ignored as irrelevant.

Chapter 7

Conclusions and Further Work

“I had nothing to offer anybody except my own confusion.”

- Sal, On the Road

To conclude this thesis, it is necessary to reconsider the original problem, whether the GCM or CF88 reaction rates more accurately describe those occurring in nature, and how these might affect the nucleosynthesis of heavy elements via the weak s-process. Direct measurements of the $^{17}\text{O}(\alpha,\gamma)^{21}\text{Ne}$ reaction were carried out in June and November 2009 with the DRAGON recoil separator at the ISAC-I facility, TRIUMF in Vancouver, Canada. Measurements were made across a range of energies, from $E_{cm} = 1.597$ MeV pushing down into the Gamow window itself with a measurement at $E_{cm} = 0.621$ MeV. Both resonant and non-resonant contributions to the reaction rate were calculated and have been presented within this thesis. In analysing the measurements performed by the DRAGON collaboration, it is clear that neither theoretical model can accurately reproduce the cross sections established by the data. The DRAGON reaction rate sits squarely in the ambiguous middle-ground.

The (α,γ) channel is significantly underestimated by the GCM model which could suggest that the channel may in fact be sufficient that ^{16}O can be labelled as a neutron poison. However, the CF88 rate also significantly overestimates the reaction rate which would be indicative of the opposite interpretation. Detailed stellar model calculations have indicated that the weak s-process is not sensitive to the absorption of free neutrons via the $^{17}\text{O}(\alpha,\gamma)^{21}\text{Ne}$ reaction below a factor of two orders of magnitude less than the (α,n) channel [25]. Therefore it is possible to conclude that the rate, as measured by the DRAGON collaboration, does not reach the level required to inhibit the s-process efficiency in massive, rotating stars at low metallicity. However, as only the upper portion of the Gamow window has been probed, and there are potentially 3 further contribut-

ing states within the window, this measurement should only be considered a lower limit. Without further spectroscopic information on these states in ^{21}Ne , particularly with regards to potential low angular momentum transfers, it is not possible to determine their possible contribution, significant or otherwise.

When discussing the potential for further work, it is always tempting to somewhat childishly say “more beam time”. While it is true that an increase in beam time would indeed allow the uncertainty to be further reduced, and a full scan to be measured, it is of more use to talk of specific astrophysical requirements. The request was made for *knowledge of the reaction rate across the full width of the Gamow window* [106]. The resonant reaction rate contributions displayed in Figure 6.9 clearly show that the contribution below the upper region of the Gamow window is negligible even for the strong 806 keV resonance so continued resources should not be wasted above this point.

What may be extremely helpful would be to further constrain the non-resonant contribution by increasing the range of fitted data points. The fit in this work being performed across a relatively narrow energy range. Should a further experimental campaign be permitted, the author would suggest initially focussing on performing a scan of the region $550 < E_{cm} < 750$ keV. Of course, with some 80 hours taken to record 5 events at $E_{cm} = 0.621$ MeV using DRAGON, alternative facilities are most likely required due to the prohibitive beam requirements of ever-decreasing cross-section measurements. This can be put into some context with a few final estimates. For $E_{cm} = 0.621$ MeV DRAGON measured $\sigma_{(\alpha,\gamma)} = 0.091$ nb compared to the Denker $\sigma_{(\alpha,n)} = 13.3$ nb, if the same ratio is assumed for $E_{cm} = 0.521$ MeV (the lowest energy measured by Denker) then $\sigma_{(\alpha,\gamma)} = 7.4$ pb. To record 1000 ^{21}Ne recoils at $E_{cm} = 0.521$ MeV, with the same beam intensity of 10^{12} pps as recorded in this thesis, DRAGON would require an astonishing 1.6×10^6 hours of beam time! It would seem necessary, therefore, to utilise alternative, complimentary measurements instead of the presented direct technique.

Appendix A

Data

The results in various forms are found within the main body of the thesis. Here, the data tables are presented for any future parties who may seek to reproduce figures of their own.

Also presented are the three weighted averages calculated for those energies regions covered by multiple measurements. Most reliable is that of the unexpectedly strong ~ 0.8 MeV resonance due to the number of repetitions involved. The two other regions, ~ 0.7 and 1.17 MeV only had two measurements each, and in one case only an upper limit can be assigned.

The error analysis was described analytically in Section 5.5.2 but here the relevant calculations are explicitly stated as Equations A.1, A.2 and A.3. The fractional error on the adjusted yield, Y , is given by:

$$\left(\frac{\delta Y}{Y}\right)^2 = \left(\frac{\delta R_Y}{R_Y}\right)^2 \times \left(\frac{\delta \delta_M}{\delta_M}\right)^2 \times \left(\frac{\delta \eta}{\eta}\right)^2 \times \left(\frac{\delta \theta}{\theta}\right)^2 \times \left(\frac{\delta \psi}{\psi}\right)^2, \quad (\text{A.1})$$

with the raw yield, R_Y ; the MCP efficiency, δ_M ; the charge state fraction, η ; the separator transmission, θ ; and the BGO efficiency, ψ , all contributing to the final value. Similarly for the fractional error on the number of incident ions, I , the same sum in quadrature:

$$\left(\frac{\delta I}{I}\right)^2 = \left(\frac{\delta R}{R}\right)^2 \times \left(\frac{\delta TrgtTrans}{TrgtTrans}\right)^2 \times \left(\frac{\delta \tau}{\tau}\right)^2 \times \left(\frac{\delta N_\alpha}{N_\alpha}\right)^2 \times \left(\frac{\delta P}{P}\right)^2 \times \left(\frac{\delta E_{beam}}{E_{beam}}\right)^2 \quad (\text{A.2})$$

is a function of the beam normalisation factor, R ; the target transmission, $TrgtTrans$;

E_{CoM} (MeV)	Adj. Yield (recoils)	$\delta A.Y(\%)$	Target Nuclei 10^{18} atoms/unit area	$\delta N(\%)$ (cm^{-2})	Incident Beam (particles)	$\delta I(\%)$
0.621*	103.1	8.0	3.184	3.9	4.247e+17	0.6
0.695†	21.8	7.5	3.316	3.7	9.533e+16	1.0
0.709† ^a	18.3	7.2	1.596	3.7	6.024e+15	4.0
0.717† ^a	20.7	5.6	3.216	3.7	6.526e+15	1.6
0.748	37.3	7.1	3.165	3.7	7.500e+16	1.2
0.785	335.8	17.0	1.569	3.7	8.431e+16	1.3
0.787 ^b	435.0	13.6	3.308	3.7	1.396e+15	3.2
0.801 ^b	381.1	13.0	1.601	3.7	1.279e+15	3.4
0.811 ^b	672.6	9.6	1.607	3.7	1.635e+15	3.2
0.814 ^b	1566.5	8.4	2.477	3.7	4.713e+15	4.9
0.818 ^b	1442.3	8.4	2.044	3.7	4.946e+15	4.8
0.822 ^b	7319.0	6.7	1.6350	3.7	2.182e+16	2.3
0.823 ^b	799.8	8.8	1.650	3.7	2.083e+15	2.6
0.825 ^b	457.4	11.6	1.233	3.7	4.715e+15	5.3
0.829	68.6	6.4	1.597	3.7	3.113e+16	2.0
0.831	53.3	6.5	1.548	3.7	4.298e+16	1.9
0.836	28.5	41.0	1.602	3.7	4.022e+16	0.8
0.931	195.8	17.7	1.578	3.7	2.817e+16	0.8
1.116	456.7	11.7	1.635	3.7	5.547e+15	2.5
1.159 ^c	1710.5	8.2	1.622	3.7	3.001e+15	2.3
1.17 ^c	2651.1	7.2	1.584	3.7	4.773e+15	6.0
1.487	668.4	11.5	1.606	3.7	1.693e+15	2.8
1.509	171.7	21.0	1.606	3.7	6.040e+14	4.8

Table A.1: Final data necessary for the calculation of the $^{17}\text{O}(\alpha,\gamma)^{21}\text{Ne}$ cross section as described by Equation 3.5. * signifies coincident yield, † indicates those energies where only an upper limit could be ascertained, and ^{a,b,c} show those energy bites covering the same resonance and from which weighted averages were taken.

E_{cm} (MeV)	σ (nb)	$\delta\sigma$	S(E) MeV.b	$\delta S(E)$	$\omega\gamma$ (meV)	$\delta\omega\gamma$
0.717	0.99	0.28	2.92e+5	8.18e+4	0.031	0.0086
0.806	180.173	8.65	7.12e+6	3.47e+5	4.03	0.195
1.165	351.07	31.05	1.20e+5	1.07e+4	10.1	0.9

Table A.2: Results for the weighted averages of the multiply measured resonances.

the DAQ livetime, τ ; the number of elastics, N_α ; the beam energy, E_{beam} ; and the target pressure, P . For the final component of Equation 3.5, the number of target nuclei, N , the uncertainty is calculated as:

$$\left(\frac{\delta N}{N}\right)^2 = \left(\frac{\delta P}{P}\right)^2 \times \left(\frac{\delta T}{T}\right)^2 \times \left(\frac{\delta l}{l}\right)^2, \quad (\text{A.3})$$

due to the target pressure, P ; the target temperature, T ; and the effective length, l .

The final table presents the results of the parameterised reaction rate. These were produced as per the discussion in Section 6.4.3 and according to Equation 6.2. Following the fit as previously described, the function was used to determine reaction rates at the same temperatures as those used by the NACRE collaboration [34].

T_9	Reaction Rate ($\text{cm}^3\text{mol}^{-1}\text{s}^{-1}$)	T_9	Reaction Rate ($\text{cm}^3\text{mol}^{-1}\text{s}^{-1}$)
0.07	4.19e-31	0.7	0.000175
0.08	2.38e-28	0.8	0.000957
0.09	3.77e-26	0.9	0.00374
0.1	2.46e-24	1	0.0114
0.11	8.33e-23	1.25	0.0894
0.12	1.73e-21	1.5	0.358
0.13	2.44e-20	1.75	0.959
0.14	2.54e-19	2	1.99
0.15	2.06e-18	2.5	5.41
0.16	1.36e-17	3	10.4
0.18	3.65e-16	3.5	16.4
0.2	5.88e-15	4	23.1
0.25	1.37e-12	5	37.9
0.3	7.84e-11	6	53.0
0.35	1.85e-09	7	67.0
0.4	2.39e-08	8	78.0
0.45	1.98e-07	9	84.5
0.5	1.18e-06	10	85.5
0.6	2.02e-05		

Table A.3: Parameterisation of the $^{17}\text{O}(\alpha,\gamma)^{21}\text{Ne}$ reaction rate.

The remaining plots to include are those looking at the range of possible reaction rates for the non-resonant contributions. A variety of fits were performed, with different assumptions made regarding which data might be the result of resonant contributions. The best fit, based on the stability of the function, was presented in the main body of the thesis in Section 6.4. In that section it was also stated how a maximum and minimum S-factor was tested to look at the range of potential non-resonant contributions. Those “fits”, both simple zeroeth-order polynomials to catch the upper and lower limits of the non-resonant

S-factors are shown here in Figure A.1.

Finally, the reaction rates from these limits are displayed in Figure A.2 alongside the previous “best fit” and the theoretical reaction rates. It can be seen that, for the region of interest, the fitted rate lies firmly between the extreme limits, although this is to be expected. What is more relevant is the contribution from the resonances included in the total DRAGON reaction rate. At the highest energies of the Gamow window, the region measured by DRAGON, the addition of the $\omega\gamma$ contributions increases the total rate by almost an order of magnitude compared to that due to the fitted non-resonant reaction rate alone, and is double the value of the upper boundary. This highlights the effect of the $E_{cm} = 0.621$ MeV resonance, and the limited information that one can gather from extrapolated results.

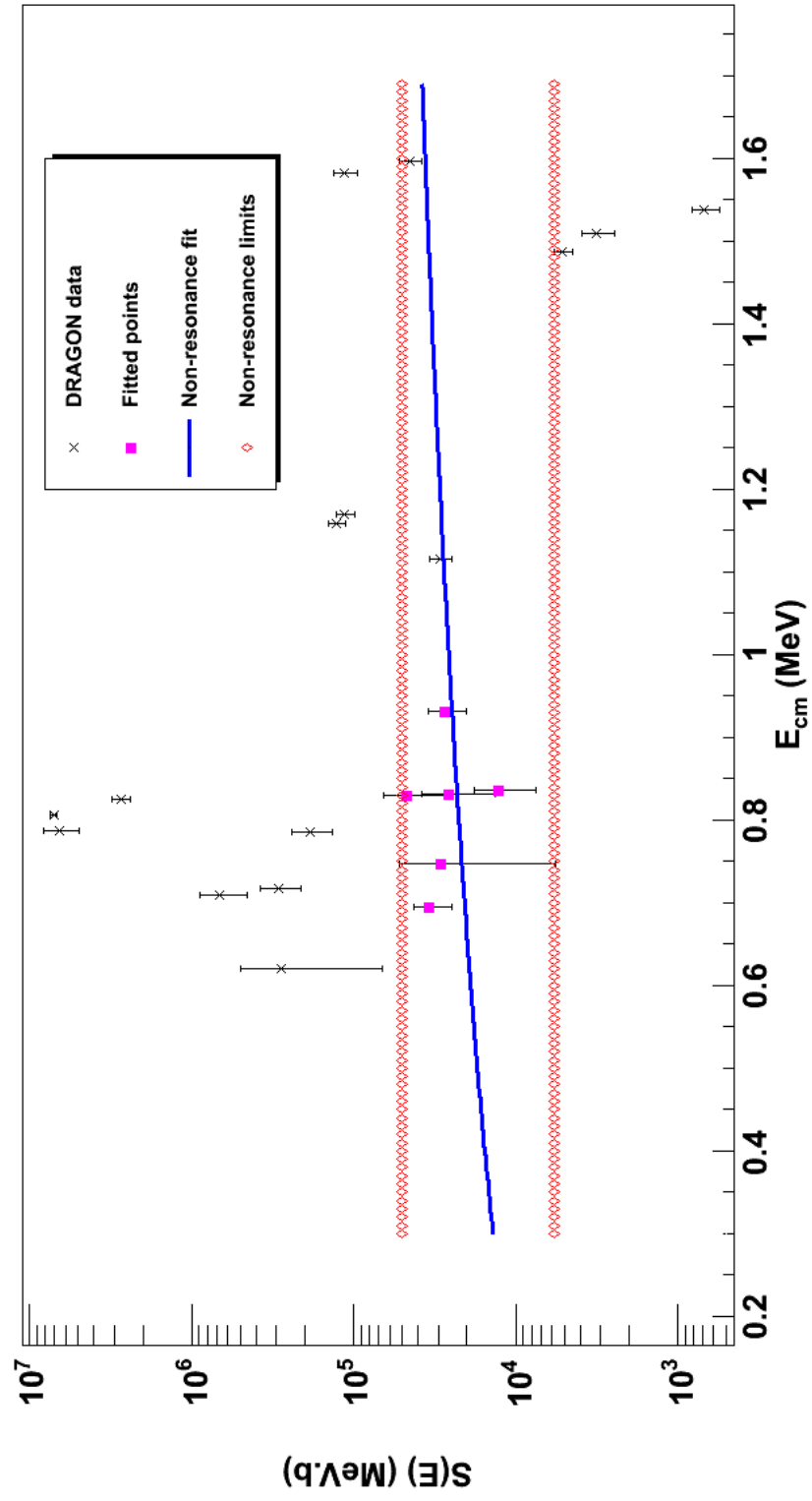


Figure A.1: Upper and lower boundaries to the non-resonant contribution.

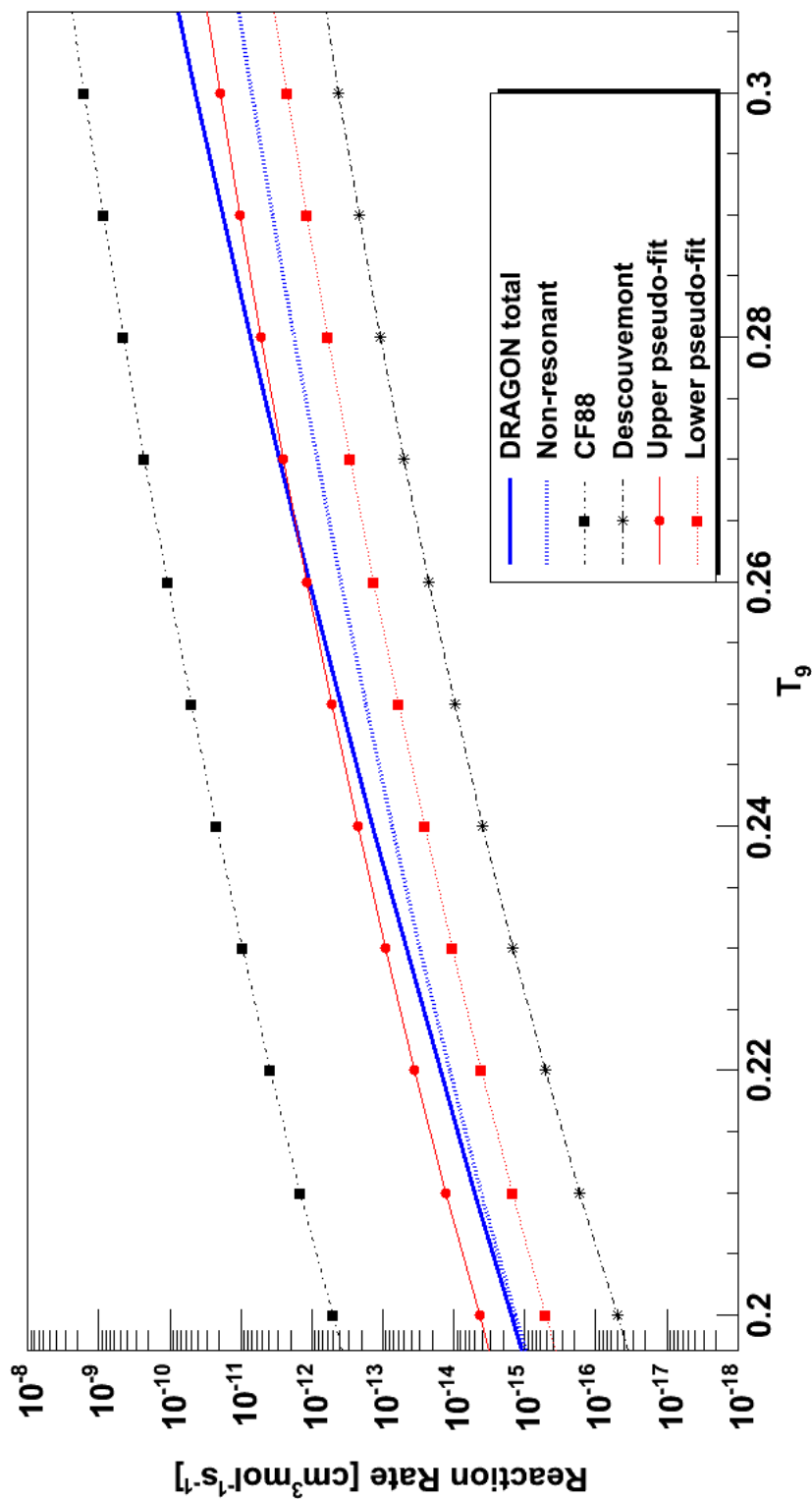


Figure A.2: Comparison of fitted reaction rates. The reaction rates of the upper and lower boundaries to the non-resonant contribution are displayed in red, along with the final DRAGON total reaction rate and the best-fit non-resonant contribution for comparison. The theoretical reaction rates are included as standard.

Appendix B

GEANT Input Parameters

The GEANT3 simulation code used by DRAGON allows for a variety of input parameters to be varied depending on requirement. The most frequently changed during the simulations required for this thesis was the gas pressure of the target cell, which GEANT used to calculate relevant stopping powers. Also simulated was the effect of different resonance widths and the distribution of the resultant γ -ray emission. Each parameter required an alteration to the GEANT source code, meaning scripting was limited to loops across energy alone.

The angular distribution of the reaction's γ -ray emission was discussed in Chapter 3 and the implementation of the code is given here. In this case the source code would be compiled to simulate reactions with a quadrupole distribution of γ rays, the change to either other distribution would simply be made by commenting out the current distribution line, and uncommenting that for the new desired distribution, before recompiling the source code.

```
C----67---- gamma angular distribution
      REAL FUNCTION angdist(X)
      REAL pi
      parameter (pi = 3.1415926)

C      A uniform angular distribution for gammas
C      angdist = 1.0
C      A quad. angular distribution for gammas
C      angdist = (15./(8.* pi))*(1.-X**2)*X**2
C      A dipole angular distribution for gammas
```

```
C      angdist = (3./(8.* pi))*(1.-X**2)
```

Chapter 5 discussed the potential importance of the effect of the de-excitation of the recoil nucleus, and also presented the level schemes used in the simulation. Initially a simple scheme (shown earlier as Figure 5.9) was used but the advent of the measurements performed by the Notre Dame group [93] allowed for a more detailed scheme to be included without relying on estimation. Specifically, information on branching ratios was also included, whereas the initial simulations assumed 100% transition between each state. Only the measurements around the $E_x = 8.154$ MeV resonance were rerun. The more complicated level scheme has been shown previously as Figure 5.14. A sample of the code used for the implementation of the full decay scheme utilised by the DRAGON Geant3 simulation is detailed below, including all the relevant information regarding modes of transition and branching ratios.

```
# Branching ratios:
# br(x,z), sets branching ratio of level(x) decay mode z
# md(x,z) = y, sets decay mode z, for level(x), to level(y)
# example
# br(2,1) = 100
# md(2,1) = 0
# sets branching ratio from level(2) to level index 1 to 100%
# sets level index 1, for level(2), to level(0)
# or, sets branching ratio from level(2) to level(0) to 100%

$params                                ztarg = 2.
life = 1E-15                            zprod = 10.
level = 15*0.                            beamlifetime = 10000.
beamtyp = '170'                          beam_mass_excess = -808.81E-6
rectyp = '21Ne'                          recoil_mass_excess = -5731.78E-6
zbeam = 8.                               resenerg = 0.806
abeam = 17.                              part_width = 0.0007
atarg = 4.                               gam_width = 0.000007
```

```
spin_stat_fac = 1.          br(2,1) = 5.
ell = 1.                   md(2,1) = 0
rstate = 10                br(2,2) = 95.
level( 0) = 0              md(2,2) = 1
level(1) = 0.350          br(3,1) = 16.7
level(2) = 1.746          md(3,1) = 0
level(3) = 2.788          br(3,2) = 83.3
level(4) = 2.794          md(3,2) = 1
level(5) = 2.866          br(4,1) = 100.
level(6) = 3.662          md(4,1) = 0
level(7) = 3.884          br(5,1) = 37.9
level(8) = 5.335          md(5,1) = 1
level(9) = 6.033          br(5,2) = 62.1
level(10) = 8.154         md(5,2) = 2
life( 0) = 1000.          br(6,1) = 57.1
life( 1) = 7.13E-12       md(6,1) = 1
life( 2) = 52.E-15        br(6,2) = 37.1
life( 3) = 81.E-12        md(6,2) = 3
life( 4) = 5.5E-15        br(6,3) = 5.8
life( 5) = 40.E-15        md(6,3) = 4
life( 6) = 65.E-15        br(7,1) = 28.3
life( 7) = 27.E-15        md(7,1) = 0
life( 8) = 7.E-15         br(7,2) = 67.3
life( 9) = 19.E-15        md(7,2) = 1
life(10) = 21.E-15        br(7,3) = 0.4
br(1,1) = 100.           md(7,3) = 3
md(1,1) = 0              br(7,4) = 4.
```

B. GEANT Input Parameters

$$\text{md}(7,4) = 6$$

$$\text{br}(8,1) = 85.4$$

$$\text{md}(8,1) = 1$$

$$\text{br}(8,2) = 10.3$$

$$\text{md}(8,2) = 5$$

$$\text{br}(8,3) = 4.3$$

$$\text{md}(8,3) = 7$$

$$\text{br}(9,1) = 39.7$$

$$\text{md}(9,1) = 2$$

$$\text{br}(9,2) = 32.9$$

$$\text{md}(9,2) = 5$$

$$\text{br}(9,3) = 15.5$$

$$\text{md}(9,3) = 7$$

$$\text{br}(9,4) = 11.9$$

$$\text{md}(9,4) = 8$$

$$\text{br}(10,1) = 66.2$$

$$\text{md}(10,1) = 2$$

$$\text{br}(10,2) = 25.8$$

$$\text{md}(10,2) = 3$$

$$\text{br}(10,3) = 8.$$

$$\text{md}(10,3) = 7$$

Appendix C

Thick Target Yield

This thesis has established, and made frequent use of, the calculation of cross section; it was presented in Chapter 3 as Equation 3.5. Reference has also been made as to the significance of beam current, and how the production of ever more intense beams can directly lead to the measurement of ever weaker reactions. The cross section is an immovable object, but the beam is a property that the experimental physicist (or rather the ever-reliable beam production physicist) has more control over. An increase in beam leads to a direct increase in yield. But the yield is a product of cross section, beam intensity and target nuclei, if the cross section is constant (for a specific energy), the beam has already been increased to its technologically limited maximum, then surely the same logic can be applied to the target? No. Not always.

A bigger target does not result in a greater yield, and for a rather simple reason. In the case of resonant reactions with a thick target, where thickness is defined relative to the width of the resonance being measured, nuclei will only react over a specific energy range, the resonance width. The yield due to the resonance being very much greater than that due to off-resonance reactions. This is depicted in Figure C.1 for a simulated narrow resonance. It can be seen how the yield, shown in the lower plot, increases as a greater portion of the resonance is integrated over, before plateauing once the entire resonance is within the target.

However, should there be a double resonance, then an increase in target thickness, to the extent that both resonances were within the energy coverage of the target then this would indeed result in a further increase in yield. This situation is shown in Figure C.2 where a the yield curve of a double peak exhibits two plateau sections where each resonance becomes wholly covered by the target region.

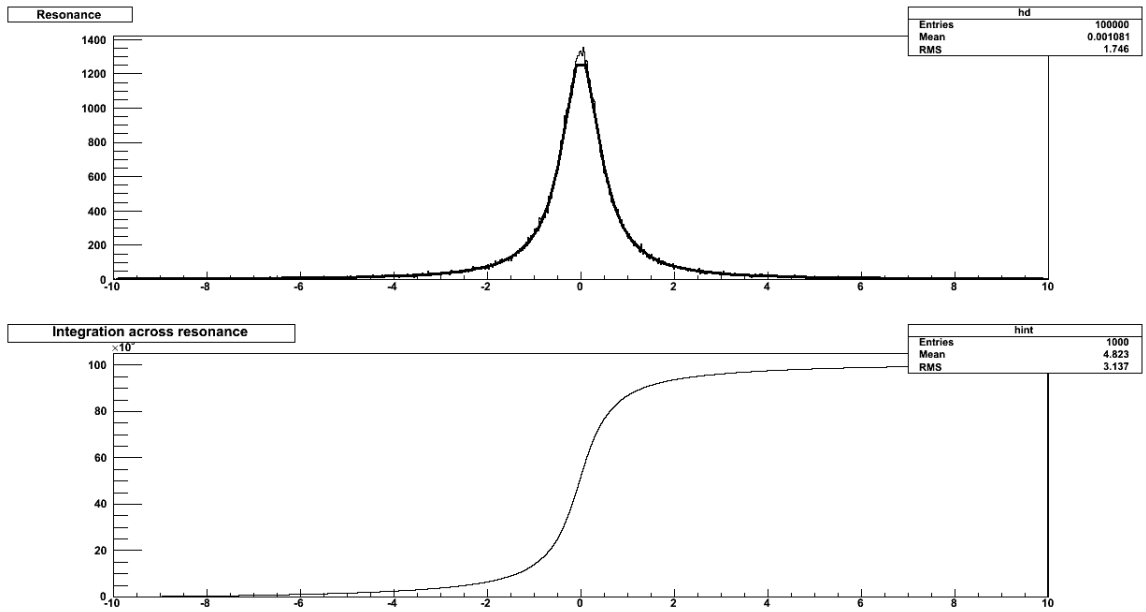


Figure C.1: Thick target yield for a single resonance.

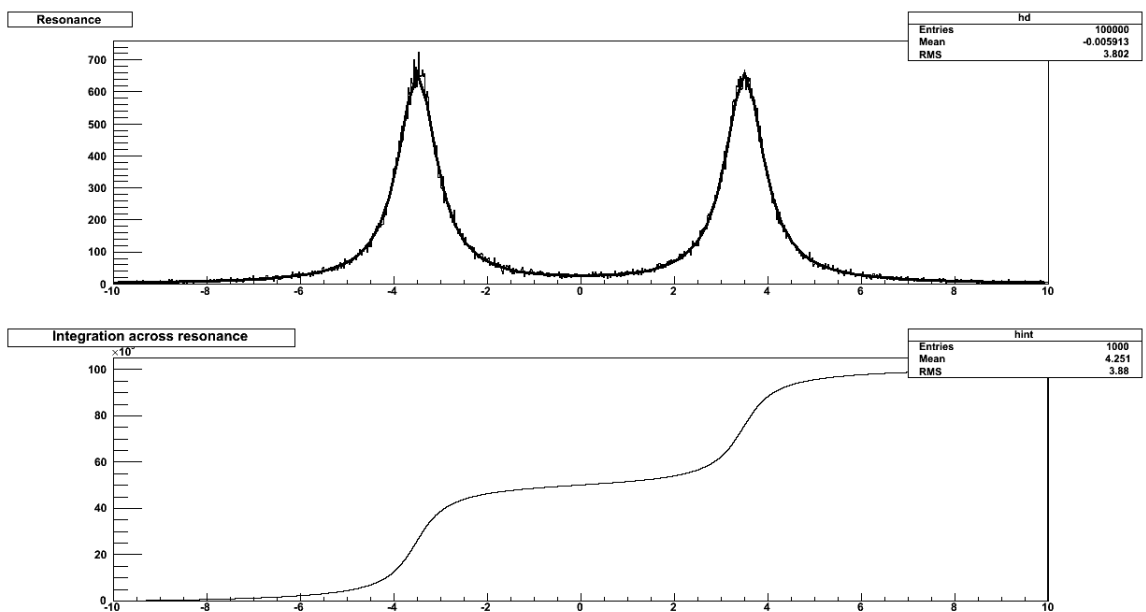


Figure C.2: Thick target yield for a double resonance.

Appendix D

The S1216 Beamlog

As was discussed in Section 4.2.6, DRAGON, through the use of the Rossum support software, maintains its own record of the various settings for each experimental run. The Rossum heartbeat maintains a log of settings such as gas pressures (Target and Ion Chamber), magnetic and electric dipole field strengths, and mass, charge and energy of the desired species. Since Rossum records these various run data at 5 minute intervals inclusion of the entire runlog would add ~40 additional pages to this work, without contributing significantly to the understanding of the reader, so only a snapshot has been included here as Table D.1.

In addition to printing only one entry per energy, several fields have been removed for the sake of brevity. In all cases of data acquisition the experiment was performed with DRAGON tuned to accept a charge state of 4^+ and a recoil mass of 21, thus it seemed unnecessary to include these here. Two energies are included in Table D.1, the first is simply the centre of mass energy, and is included for reference with the rest of the thesis, the second is the energy of the recoil entering DRAGON. Also, it should be noted that in the case of $E_{cm} = 1.17$ MeV Rossum was unavailable, data was still acquired but the NMR and ED settings were lost. Finally, the uncertainties on the recorded values of the magnetic and electric fields have been shown to be better than 1% [72].

MIDAS runs	E_{cm} (MeV)	E_{Tuned}	Target (Torr)	IC	NMR1 (Gauss)	NMR2	ED1	ED2
20028-41	1.537	6.467	4.06	7.81	4195.45	5161.29	82.41	65.47
20042	1.509	6.347	4.06	7.81	4155.84	5111.8	99.84	79.25
20043-45	1.487	6.256	4.05	7.81	4125.78	5073.23	79.72	63.21
21132-35	1.17	-	4.00	8.3		Rossum failure		

D. The S1216 Beamlog

20047-50	1.159	4.859	4.10	7.81	3636.76	4467.29	61.53	49.01
20052-56	1.116	4.67	4.13	7.81	3564.79	4378.61	59.08	47.08
20062-98	0.931	3.886	3.99	6.59	3252.18	3998.84	48.99	39.28
20104-44	0.836	3.487	4.05	7.81	3080.91	3782.84	44.09	35.12
21140-54	0.831	3.471	3.91	8.3	3073.39	3778.41	43.97	35
21157-64	0.829	3.464	4.03	8.3	3070.38	3773.93	43.89	34.85
21175-76	0.825	3.455	3.11	8.06	3065.56	3766.26	43.76	34.77
20146-48	0.823	3.433	4.17	7.81	3056.88	3754.78	43.42	34.56
21169-73	0.822	3.425	4.13	8.3	3053.19	3750.77	43.38	34.47
21177-78	0.818	3.393	5.16	8.3	3039.33	3733.54	42.97	34.14
21179	0.814	3.359	6.26	8.3	3024.44	3715.15	42.54	33.8
20149-50	0.811	3.381	4.06	7.81	3033.2	3727.72	42.64	34.01
20152-53	0.801	3.338	4.04	7.81	3013.64	3705.47	42.24	33.6
20156-57	0.787	3.221	8.36	7.81	2960.59	3633.91	50.06	39.95
21184-99	0.785	3.271	3.96	8.3	2983.7	3665.15	41.43	32.9
21206-22	0.748	3.053	8.0	8.3	2884.78	3541.72	38.57	30.67
20159-68	0.717	2.925	8.12	7.81	2821.73	3468.99	36.85	29.55
21247-48	0.709	2.953	4.03	8.3	2834.64	3487.45	37.39	29.63
21224-43	0.695	2.836	8.38	8.3	2778.03	3407.77	35.68	28.37
21258-360	0.621	2.524	8.04	6.35	2620.72	3222.45	31.88	25.32

Table D.1: A snapshot of the Rossum heartbeat runlog. MIDAS gives the unique identifier for each “run” (usually renewed each hour unless stopped early by the DRAGON operator), the energies are the centre of mass energy of the reaction and the tuned DRAGON energy, Target and IC are the pressures of the gas target and ion chamber, NMR1 & 2 are the field strengths recorded on MD1 & 2 respectively, likewise with ED1 & 2.

Appendix E

Logic Symbols

In tribute to the (far more impressive) texts that have preceded this work a collection of common electronics logic box symbols are included here. Primarily these are included as an aid to the diagram of the data acquisition electronics in Section 4.19. The symbols themselves are listed as Figure E.1.

In addition to the symbols key itself the respective truth tables are also included as Table E.1. Furthermore, the mathematical operator for each logic gate are also displayed for completeness.

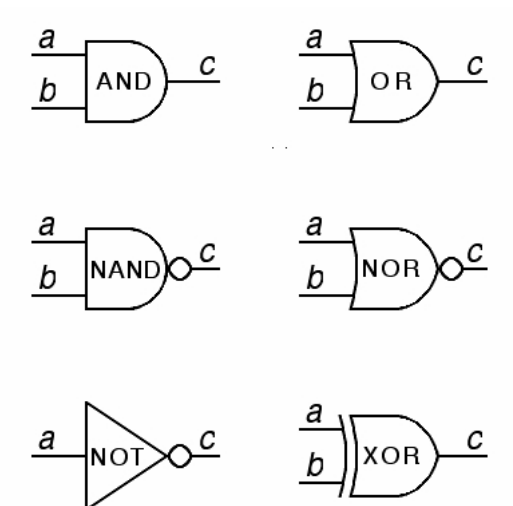


Figure E.1: Some common electronics logic symbols [79].

input		output c					
a	b	AND ab	OR $a + b$	NAND \overline{ab}	NOR $\overline{a + b}$	NOT \bar{a}	XOR $a \oplus b$
0	0	0	0	1	1	1	0
0	1	0	1	1	0	1	1
1	0	0	1	1	0	0	1
1	1	1	1	0	0	0	0

Table E.1: Boolean logic truth tables.

Nomenclature

Throughout the thesis many acronyms and abbreviations are used, in the first instance they will be defined, but for ease of reference a selection of terminology is listed here.

General Abbreviations

- AGB – Asymptotic Giant Branch
- BBN – Big Bang Nucleosynthesis
- BGO – Bismuth Germanate
- DSSSD – Double-Sided Silicon Strip Detector
- DTL – Drift-Tube Linac
- ECR – Electron Cyclotron Resonance
- FC – Faraday Cup
- HEBT – High Energy Beam Transport
- HPGe – Hyper-Pure Germanium
- ISAC – Isotope Separation and Acceleration
- ISM – Interstellar Medium
- ISOL – Isotope Separation On-line
- MEBT – Medium Energy Beam Transport
- NMR – Nuclear Magnetic Resonance
- RFQ – Radio-Frequency Quadrupole

-
- SEMF – Semi-Empirical Mass Formula
 - TACTIC – TRIUMF Annular Chamber for Tracking and Identification of Charged-particles
 - TUDA – TRIUMF-UK Detector Array
 - TRIUMF – TRI-University Meson Facility

Equipment

- DRAGON – Detector of Recoils and Gammas of Nuclear reactions
- ED – Electric Dipole
- EMS – ElectroMagnetic Separator
- FC4 – Faraday Cup upstream of gas target
- FC1 – Faraday Cup downstream of gas target
- FCCH – Faraday Cup downstream of MD1
- IC – Ion Chamber
- MD – Magnetic Dipole
- MCP – Micro Channel Plates

Analysis and Electronics

- ADC – Analog-to-Digital Converter
- AMP – Amplifier
- CFD – Constant Fraction Discriminator
- DAQ – Data Acquisition
- DISC – Discriminator
- LED – Leading Edge Discriminator
- HI – Heavy Ion
- ICsumMCPtof – Histogram of IC energy versus MCP time-of-flight

-
- ICsumICX – Histogram of IC total energy versus individual anode
 - MEM – Memory
 - PMT – Photo Multiplier Tube
 - SCA – Single Channel Analyser
 - TAC – Time-to-Amplitude Converter
 - ToF – Time-of-Flight

Astrophysics Terminology

- E_G – Gamow Energy
- ΔE_G – Gamow Window
- T_6 – Stellar Temperature in MK
- T_9 – Stellar Temperature in GK
- M_\odot – Mass of the Sun

Key Parameters

- $M_{^{17}O}$ – 16.999131u
- $M_{^4He}$ – 4.002603u

References

- [1] E. Margaret Burbidge, G. R. Burbidge, William A. Fowler, and F. Hoyle. Synthesis of the elements in stars. *Reviews of Modern Physics*, 29:547–650. [1](#)
- [2] Bernard E.J. Pagel. *Nucleosynthesis and Chemical Evolution of Galaxies*. Cambridge University Press, 2nd edition, 2009. Pages 1, 8-9, 50, 98, 221. [2](#), [3](#), [4](#), [8](#), [10](#), [15](#)
- [3] A.G.W. Cameron. *Essays in Nuclear Astrophysics*. Cambridge University Press, 1982. Page 23. [2](#)
- [4] Ian J. Thompson and Filomena M. Nunes. *Nuclear Reactions for Astrophysics: Principles, Calculation and Applications of Low-Energy Reactions*. Cambridge University Press, 2009. Page 8. [3](#)
- [5] Lawrence Kawano. Primordial nucleosynthesis the computer way. Technical report, Fermi National Accelerator Laboratory, 1992. FERMILAB-Pub-92/04-A. [3](#)
- [6] A.C. Phillips. *The Physics of Stars*. Wiley, 2nd edition, 2008. Pages 5, 26. [4](#), [40](#)
- [7] Carl Sagan. *Cosmos*. Random House, 2002. Page 168. [4](#)
- [8] P.D. Serpico, S. Esposito, F. Iocco, G. Mangano, G. Miele, and O. Pisanti. Nuclear reaction network for primordial nucleosynthesis: a detailed analysis of rates, uncertainties and light nuclei yields. *Journal of Cosmology and Astroparticle Physics*, 12:010, 2004. [4](#)
- [9] F. Hoyle. On nuclear reactions occurring in very hot stars. I. the synthesis of elements from carbon to nickel. *Astrophysical Journal Supplement*, 1:121–146, 1954. [4](#)
- [10] R. Bass. *Nuclear Reactions with Heavy Ions*. Springer-Verlag, 1980. Pages 1-9. [6](#)

- [11] Richard N. Boyd. *An Introduction to Nuclear Astrophysics*. The University of Chicago Press, 2008. Pages 224-238. 7
- [12] K. Heyde. *Basic Ideas and Concepts in Nuclear Physics: An Introductory Approach*. Institute of Physics Publishing, 3rd edition, 2004. Page 9. 7
- [13] Richard Shurtleff and Edward Derringham. The most tightly bound nucleus. *American Journal of Physics*, 57(6):552, 1989. 7
- [14] Claus E. Rolfs and William S. Rodney. *Cauldrons in the Cosmos*. The University of Chicago Press, 1988. Pages 135, 156-7, 169-178, 414. 8, 40, 121, 128, 130
- [15] Donald D. Clayton. *Principles of Stellar Evolution and Nucleosynthesis*. The University of Chicago Press, 1983. Pages 557, 577-579. 8, 11, 15
- [16] F. Käppeler. Reaction cross sections for the s, r, and p process. *Progress in Particle and Nuclear Physics*, 66:390–9, 2011. 12
- [17] Bradley S. Meyer. The r-, s- and p-processes in nucleosynthesis. *Annual Review of Astronomy and Astrophysics*, 32:153–90, 1994. 12, 13, 17
- [18] D.D. Clayton, W.A. Fowler, T.E. Hull, and B.A. Zimmerman. Neutron capture chains in heavy element synthesis. *Annals of Physics*, 12:331–408, 1961. 12
- [19] P.A. Seeger, W.A. Fowler, and D.D. Clayton. Nucleosynthesis of heavy elements by neutron capture. *The Astrophysical Journal Supplement*, 11:121–166, 1965. 12, 13
- [20] D.D. Clayton and M.E. Rassbach. Termination of the s-process. *The Astrophysical Journal*, 148:69–85, 1967. 14
- [21] D.D. Clayton and R.A. Ward. S-process studies - exact evaluation of an exponential distribution of exposures. *The Astrophysical Journal*, 193, 1974. 12
- [22] R. Hirschi *et al.* Nugrid: s-process in massive stars. In *Proceedings of The 10th Symposium on Nuclei in the Cosmos*. 13, 16, 22, 24, 40
- [23] Joachim Görres. Experiments in nuclear astrophysics I. WE-Heraeus Summer School on Nuclear Astrophysics in the Cosmos, July 2010. http://exp-astro.physik.uni-frankfurt.de/meetings/nic-school-2010/lectures/goerres_GSI_Summer_School.pdf. 13

- [24] M. Wiescher, J. Görres, E. Uberseder, G. Imbriani, and M. Pignatari. The cold and hot CNO cycles. *Annual Review of Nuclear and Particle Science*, 60:381–404, 2010. 17
- [25] U. Frischknecht, R. Hirschi, and F.-K. Thielemann. Non-standard s-process in low metallicity massive stars. *Astronomy & Astrophysics*, 538, 2012. 17, 139
- [26] Reactor concepts manual: Pressurized water reactor (PWR) systems, August 2009. U.S. Nuclear Regulatory Commission. 17
- [27] Raymond L. Murray. *Nuclear Energy: An Introduction to the Concepts, Systems, and Applications of Nuclear Process*. Butterworth-Heinemann, 5th edition, 2000. Pages 140-141, 269. 17
- [28] M. Rayet and M. Hashimoto. The s-process efficiency in massive stars. *Astronomy & Astrophysics*, 354:740, 2000. 17, 128
- [29] Knolls Atomic Power Laboratory. Nuclides and isotopes: Chart of the nuclides 17th edition. <http://www.nuclidechart.com/>, 2010. 17
- [30] <http://www.nndc.bnl.gov/nudat2/>, July 2012. 18, 41
- [31] T. Belgya, E. Uberseder, D. Petrich, and F. Käppeler. Thermal neutron capture cross section of ^{22}Ne . In *Proceedings of The 13th International Symposium on Capture Gamma-Ray Spectroscopy and Related Topics*, volume 1090, pages 367–371, 2008. 17
- [32] Robert Eisberg and Robert Resnick. *Quantum Physics of Atoms, Molecules, Solids, Nuclei and Particles*. Wiley, 2nd edition, 1985. Page 618. 19
- [33] Kenneth S. Krane. *Modern Physics*. Wiley, 2nd edition, 1996. Pages 448-9. 19
- [34] NACRE collaboration. Nacre - european compilation of reactions rates for astrophysics. <http://pntpm3.ulb.ac.be/Nacre/nacre.htm>, October 2008. 19, 20, 112, 133, 143
- [35] A. Denker. *Drei Neutronenerzeugungsreaktion in Sternen*. PhD thesis, Universität Stuttgart, 1994. 19, 77, 78, 119, 121, 122, 127
- [36] J.K. Bair and F.X. Haas. Total Neutron Yield from the Reactions $^{13}\text{C}(\alpha,n)^{16}\text{O}$ and $^{17,18}\text{O}(\alpha,n)^{20,21}\text{Ne}$. *Physical Review C*, 7(4):1356–1364, 1973. 19, 20, 77

- [37] L.F. Hansen, J.D. Anderson, J.W. Mclure, B.A. Pohl, M.L. Stelts, J.J. Wesolowski, and C. Wong. The (α, n) cross sections on ^{17}O and ^{18}O between 5 and 12.5 MeV. *Nuclear Physics A*, 98:25–32, 1967. [19](#), [20](#), [77](#), [127](#)
- [38] William A. Fowler, Georgeanne R. Caughlan, and Barbara A. Zimmerman. Thermonuclear reaction rates. *Annual Review of Astronomy and Astrophysics*, 5:525–570, 1967. [21](#)
- [39] William A. Fowler, Georgeanne R. Caughlan, and Barbara A. Zimmerman. Thermonuclear reaction rates, II. *Annual Review of Astronomy and Astrophysics*, 13:69–112, 1975. [21](#), [128](#), [129](#), [134](#)
- [40] Michael J. Harris, William A. Fowler, Georgeanne R. Caughlan, and Barbara A. Zimmerman. Thermonuclear reaction rates, III. *Annual Review of Astronomy and Astrophysics*, 21:165–176, 1983.
- [41] William A. Fowler, Michael J. Harris Georgeanne R. Caughlan, and Barbara A. Zimmerman. Tables of thermonuclear reaction rates for low-mass nuclei ($1 \leq z \leq 14$). *Atomic Data and Nuclear Data Tables*, 32:197–233, 1985.
- [42] Georgeanne R. Caughlan and William A. Fowler. Thermonuclear reaction rates V. *Atomic Data and Nuclear Data Tables*, 40:283–334, 1988. [21](#)
- [43] P. Descouvemont. Microscopic three-cluster study of 21-nucleon systems. *Physical Review C*, 48(6):2746–2752, 1993. [21](#), [22](#), [122](#), [128](#), [129](#), [134](#)
- [44] P. Descouvemont. Microscopic models for nuclear reaction rates. *Journal of Physics G*, 19:S141–S152, 1993. [21](#)
- [45] C. Angulo *et al.* A compilation of charged-particle induced thermonuclear reaction rates. *Nuclear Physics A*, 656:3–183, 1999. [28](#)
- [46] C. Iliadis. *Nuclear Physics of Stars*. Wiley, 2007. Pages 171-201, 438. [28](#), [31](#), [32](#), [33](#), [34](#), [40](#), [128](#)
- [47] R.A. Wolf. Rates of nuclear reactions in solid-like stars. *Physical Review*, 137:B1634–B1643, 1965. [29](#)
- [48] D. Hutcheon. Analysis of DRAGON data. private communication, 2009. [34](#)

- [49] C.E. Svensson *et al.* TIGRESS: TRIUMF-ISAC gamma-ray escape-suppressed spectrometer. *Journal of Physics G: Nuclear and Particle Physics*, 31:S1663, 2005. [37](#)
- [50] I-Yang Lee. The GAMMASPHERE. *Nuclear Physics A*, 520:641–655, 1990.
- [51] C.Aa. Diget, S.P. Fox, A. Smith, S. Williams, M. Porter-Peden, L. Achouri, P. Ad-sley, H. Al-Falou, R.A.E Austin, G.C. Ball, J.C. Blackmon, S. Brown, W.N. Catford, A.A. Chen, J. Chen, R.M. Churchman, J. Dech, D. DiValenti, M. Djongolov, B.R. Fulton, A. Garnsworthy, G. Hackman, U. Hager, R. Ksherti, L. Kurchaninow, A.M. Laird, J.-P. Martin, M. Matos, J.N. Orce, N.A. Orr, C.J. Pearson, C. Ruiz, F. Sarazin, S. Sjue, D. Smalley, C.E. Svensson, M. Taggart, E. Tardiff, and G.L. Wilson. SHARC: Silicon highly-segmented array for reactions and coulex used in conjunction with the tigris γ -ray spectrometer. *Journal of Instrumentation*, 6:P02005. [37](#)
- [52] Sabine Engel. *Awakening of the DRAGON: Commissioning of the DRAGON Recoil Separator Experiment & First Studies on the $^{21}\text{Na}(p,\gamma)^{22}\text{Mg}$ Reaction*. PhD thesis, Ruhr-Universität Bochum, 2003. [37](#), [62](#), [72](#)
- [53] S. Engel, D. Hutcheon, and S. Bishop *et al.* Commissioning the DRAGON facility at ISAC. *Nuclear Instruments and Methods in Physics Research A*, 553:491, 2005. [37](#), [55](#), [58](#)
- [54] Urs Frischknecht. private communication, 2011. [40](#)
- [55] <http://www.nndc.bnl.gov/ensdf/>, October 2011. [40](#), [96](#), [126](#)
- [56] E.C. Simpson. private communication, 2012. [40](#)
- [57] M. Marchetto *et al.* Radioactive ion beam post-acceleration at ISAC. *European Physical Journal Special Topics*, 150:241–242, 2007. [43](#)
- [58] M. Marchetto, J. Berring, and R.E. Laxdal. Upgrade of the ISAC DTL tuning procedure at TRIUMF. In *Proceedings of The 11th European Particle Accelerator Conference*, 2008. [43](#)
- [59] Pierre Bricault, Friedhelm Ames, Tobias Achtzehn, Marik Dombisky, and Francis Labrecque *et al.* An overview on TRIUMF’s developments on ion source for radioactive beams (invited). *Review of Scientific Instruments*, 79, 2008. [43](#), [45](#)

- [60] W. Gelletly. Science with radioactive beams: The alchemist's dream. *Contemporary Physics*, 42:285–314, 2001. 45
- [61] A. Shotter. Radioactive beams. *Nuclear Physics A*, 752:532–539, 2005. 45
- [62] K. Jayamana *et al.* Off-line ion source terminal for ISAC at TRIUMF. *Review of Scientific Instruments*, 79:02C711, 2008. 45
- [63] Luke Erikson. *Experimental Developments for the Study of Explosive Nucleosynthesis in Stars*. PhD thesis, Colorado School of Mines, 2006. 46, 71
- [64] Ian G. Brown. *The Physics and Technology of Ion Sources*. Wiley, 2nd edition, 2004. Pages 177-212. 45, 47
- [65] H. Postma. Multiply charged heavy ions produced by energetic plasmas. *Physics Letters A*, 31:196–197, 1970. 47
- [66] K. Jayamana *et al.* A multicharge ion source (supernanogan) for the OLIS facility at ISAC/TRIUMF. *Review of Scientific Instruments*, 81:023304, 2010. 48
- [67] A. Sawchenko. private communication, 2009. 48
- [68] Robert E. Laxdal *et al.* RNB post-accelerator for ISAC at TRIUMF - present and future. *Nuclear Physics A*, 701:647–650, 2002. 49
- [69] M. Weiss. Radio frequency quadrupole. Technical report, CAS Aarhus, 1986. CERN-PS 87-51. 48
- [70] <http://www.aps.anl.gov/epics/index.php>, December 2011. 53
- [71] J. D'Auria *et al.* Astrophysics with a DRAGON at ISAC. *Nuclear Physics A*, 701:625–631, 2003. 53, 71, 77, 106
- [72] D. Hutcheon *et al.* The DRAGON facility for nuclear astrophysics at TRIUMF-ISAC: design, construction and operation. *Nuclear Instruments and Methods in Physics Research A*, 498:190–210, 2003. 53, 57, 58, 63, 64, 72, 74, 75, 77, 108, 153
- [73] J.B.A. England. *Techniques in Nuclear Structure Physics*, volume 1. Macmillan, 1974. Page 144. 58
- [74] K.L. Brown and G.W. Tautfest. Faraday-cup monitors for high-energy electron beams. *Review of Scientific Instruments*, 27:696, 1956. 58

- [75] <http://princetonscientific.com/pdf/beam/09--.pdf>, January 2011. 59
- [76] Shawn Bishop. *Direct Measurement of the $^{21}\text{Na}(p,\gamma)^{22}\text{Mg}$ Resonant Reaction Rate in Nova Nucleosynthesis*. PhD thesis, Simon Fraser University, 2003. 61, 105, 108
- [77] L. Buchman *et al.* Nuclear astrophysics at TRIUMF. *Nuclear Physics A*, 805:462c–469c, 2008. 62
- [78] RUVAC: Roots vacuum pumps, single-stage. http://www.idealvac.com/files/brochures/Oerlikon_Leybold_Roots_Blower_Vacuum_Pump_Catalog.pdf, 2006. Excerpt from the Leybold Vacuum Full Line Catalog. 62
- [79] W.R. Leo. *Techniques for Nuclear and Particle Physics Experiments: A How-to Approach*. Springer-Verlag, 2nd edition, 1994. Pages 21-22, 241, 318, 326-327. 64, 65, 74, 155
- [80] Dario G. Gigliotti. Efficiency calibration measurement and GEANT simulation of the DRAGON BGO gamma ray array at TRIUMF. Master's thesis, The University of Northern British Columbia, 2004. 66, 68, 85
- [81] Glenn F. Knoll. *Radiation Detection and Measurement*. Wiley, 2000. Pages 152, 239, 276, 451, 659-660. 65, 67, 69, 70, 72, 74
- [82] R.D. Evans. *The Atomic Nucleus*. McGraw-Hill, 1955. Page 712. 67
- [83] C. Vockenhuber *et al.* A transmission time-of-flight system for particle identification at a recoil mass separator at low energies. *Nuclear Instruments and Methods in Physics Research A*, 603:372–378, 2009. 69, 102
- [84] C. Vockenhuber *et al.* The $^{40}\text{Ca}(\alpha,\gamma)^{44}\text{Ti}$ reaction at DRAGON. *Nuclear Instruments and Methods in Physics Research B*, 259:688–693, 2007. 71, 90
- [85] S. Engel *et al.* Development of detection systems for low-energy heavy ions at DRAGON. *Nuclear Physics A*, 701:228–230, 2002. 71
- [86] J. Ziegler. SRIM-2003. *Nuclear Instruments and Methods in Physics Research B*, 219:1027–1036, 2004. <http://www.srim.org>. 71
- [87] Wenjie Liu. Charge state studies of heavy ions passing through gas. Master's thesis, Simon Fraser University, 2001. 73, 90, 92

- [88] Christian Ouellet. The $^{40}\text{Ca}(\alpha,\gamma)^{44}\text{Ti}$ nuclear reaction using DRAGON. Master's thesis, McMaster University, 2007. 74, 76
- [89] C. Ruiz. private communication, 2008. 74, 77
- [90] <http://subatomic.mines.edu/mantle/?CMSPAGE=Research/nuclear/mantle/>, 2008. Colorado School of Mines Software Guide. 76
- [91] A.M. Laird, C. Ruiz, and M.P. Taggart. A direct measurement of the $^{17}\text{O}(\alpha,\gamma)^{21}\text{Ne}$ reaction. Submitted to the TRIUMF EEC, October 2008. 77
- [92] TRIUMF EEC panel. Report of the subatomic physics experiments evaluation committee. Technical report, TRIUMF, December 2008. http://www.triumf.ca/sites/default/files/200812_sap_report.pdf. 77
- [93] A. Best *et al.* First direct measurement of resonance strengths in $^{17}\text{O}(\alpha,\gamma)^{21}\text{Ne}$. *Physical Review C*, 83, 2011. 95, 96, 100, 124, 126, 129, 136, 148
- [94] U. Hager. private communication, 2010. 95
- [95] P. Endt. Strengths of gamma-ray transitions in $A = 5-44$ nuclei, IV. *Atomic Data and Nuclear Data Tables*, 55:171–197, 1993. 96, 112
- [96] A. Bloch. *Murphy's Law*. Perigee Trade, 26th edition, 2003. Page 1. 108
- [97] National Climate Data and Information Archive. http://climate.weatheroffice.gc.ca/climateData/canada_e.html, May 2012. 114
- [98] G.L. Squires. *Practical Physics*. Cambridge University Press, 3rd edition, 1985. Pages 37-38. 116
- [99] R.J. Barlow. *Statistics: A Guide to the Use of Statistical Methods in the Physical Sciences*. Wiley, 1999. Pages 55-61. 116
- [100] G.J. Feldman and R.D. Cousins. Unified approach to the classical statistical analysis of small signals. *Physical Review D*, 57:3873–3889, 1998. 116, 117, 134
- [101] J. Neyman. Outline of a theory of statistical estimation based on the classical theory of probability. *Philosophical Transactions of The Royal Society*, A236:250–289, 1937. 116
- [102] Frederick James. *Statistical Methods in Experimental Physics*. World Scientific, 2006. Pages 225-231. 116

- [103] David Arnett. *Supernovae and Nucleosynthesis: An Investigation of the History of Matter, From the Big Bang to the Present*. Princeton University Press, 1996. Pages 90-91. [127](#)
- [104] Th. Rauscher. private communication, 2010. [132](#)
- [105] <http://digitizer.sourceforge.net/>, June 2012. [136](#)
- [106] M. Pignatari. private communication, 2011. [140](#)